Quasi–one-dimensional superfluidity

Pierre-François Duc

Department of Physics
McGill University
Montréal, Québec, Canada
December 2018

A thesis submitted to McGill University in partial fulfillment of the requirements of the degree of Doctor of Philosophy

“*Ce n’est qu’en essayant continuellement qu’on finit par réussir & donc plus ça rate plus on a de chances que ça marche!*”

Les Fondements de la pensée Shadock

ABSTRACT

The breakdown of the celebrated Fermi liquid theory in 1D motivated Tomonaga and Luttinger to propose new models to describe many-body physics in 1D. To experimentally test the predictions of Tomonaga–Luttinger physics, experiments have been performed over the last twenty years or so in electronic systems and low-density cold atoms gases. However, as of today and seventy years after Tomonaga and Luttinger seminal works, a one-dimensional high-density strongly correlated bosonic experimental system is still lacking. In this thesis, we provide the first experimental realization of a quasi–one-dimensional flow with superfluid helium–4. Measurements of ^{4}He flow through a *single* nanopore of $\sim$3 nm radius were performed as a function of temperature above and below the superfluid transition temperature T_λ. The observed pressure dependence of the flow is found to be much weaker than in larger pores, and from previous studies. The critical velocities of the superfluid inside the pore are extracted from the measurements by combining a short-pipe hydrodynamic model developed by Langhaar, and the two-fluid model of Tisza and Landau. The temperature dependence of the critical velocities below the transition temperature is found to be well-modeled by a power law with non-universal exponent, in contrast to the known behavior of the bulk ^{4}He superfluid exhibinting critical exponents belonging to the three-dimensional O(2) universality class. Furthermore, the critical velocities associated with each of the nanopores studied are found decrease with the nanopore radius. This is also in stark contrast with the behavior predicted by the Feynman critical velocity model observed in larger pores. Recent theoretical advances regarding superfluid dissipation predict a similar trend that is observed in our work, and suggest that our smallest pore is neighboring a regime where enhanced dissipations inside the pore will further suppress the critical velocity. Our findings are an important advance towards the realization of a Tomonaga–Luttinger liquid in a dense bosonic system.

ABRÉGÉ

L'échec de la théorie du liquide de Fermi en 1D a motivé Tomonaga et Luttinger à développer un nouveau modèle pour décrire la physique corpusculaire en 1D. Afin de vérifier expérimentalement les prédictions de Tomonaga–Luttinger, des expériences ont été effectuées avec des systèmes électroniques et des gaz d'atomes froids à faibles densités. Pourtant aujourd'hui, 70 années après les travaux précurseurs de Tomonaga et Luttinger, aucun système expérimental de bosons à haute densité et fortement corrélés n'a encore été réalisé. Dans cette thèse, nous réalisons expérimentalement pour la première fois écoulement quasi–uni-dimensionel avec de l'Hélium–4 superfluide. Des mesures du débit massique d'^{4}He à travers un *unique* nanopore de $\sim$3 nm de rayon on été effectuées en fonction de la température en dessus et en dessous de la température de transition superfluide T_λ. La dépendance en pression du débit massique observée est bien plus faible que dans le cas de nanopores plus larges, ainsi que rapporté précedemment dans la littérature. Les vitesses critiques du superfluide dans le nanopore sont extraites des mesures en combinant un modèle d'écoulement hydrodynamique classique pour canal court développé par Langhaar avec le modèle des "deux-fluides" de Tisza et Landau. La dépendance en température des vitesses critiques en dessous de la température de transition est bien décrite par une loi de puissance avec des exposants non-universels, contrastant avec le comportement connu de l'^{4}He superfluide proche de la transition qui est décrit par des loi de puissance avec des exposants critiques appartenant à la classe d'universalité tri-dimensionelle O(2). De plus, nous avons établi que la vitesse critique diminue lorsque le rayon du nanopore diminue en comparant les vitesses critiques de trois nanopores. Cela est en opposition forte à la tendance prédite par le modèle de vitesse critique de Feynman, qui avait été observée pour des pores de plus grands rayons précedemment. Des avancées théoriques récentes concernant les dissipations dans la phase superfluide prédisent une dépendance de la vitesse critique par rapport à la taille du nanopore qui est en accord avec celle que nous avons observée. Par ailleurs elles suggèrent que notre plus petit nanopore est à la frontière d'un régime où il est prédit que les dissipations sont créées à plus haute fréquence et contribuent à réduire fortement la vitesse critique. Nos résultats constituent une avancée importante vers la réalisation d'un liquide de Tomonaga–Luttinger dans un sytème de bosons denses.

ACKNOWLEDGEMENTS

This thesis, although it bears my name, would not have been conceivable without the great help and support I received from many during these years. First, I would like to thank my supervisor, Guillaume Gervais, for his incredible amount of energy and setting ambitious scientific goals. He always pushed me to go beyond my limits while letting me explore freely. He nevertheless was always present when his help was needed. I am grateful for his trust and unfailing support. Amongst my other colleagues in the laboratory, my gratitude goes first to Michel Savard who patiently taught me everything he knew about the nanopores and how to run the helium–3 fridge, before handing me the relay on a race towards one-dimensional confinement of helium. I thank Benjamin Schmidt for sharing his immense knowledge of measurements at low temperatures and for the stimulating pythonic instrument control and data analysis discussions. I take the opportunity to acknowledge the Python Software foundation and the python community. All the data acquisition and visualization in this thesis were performed using their opensource libraries. I am grateful to Keyan Bennaceur for his tips regarding sample preparation and for always lending me an attentive ear. I thank Matei Petrescu, in particular for his assistance on the nanopore's fabrication, and the continuous operation of the fridge during superfluid measurements. Although the laboratory was in a basement, all its members were as many windows on the outside world and I would also like to thank them for making the lab such a pleasant environment. Special thanks to Samuel Gaucher, Simon Bilodeau, Eli Gerber, Camille Bowness and Oulin Yu. I will cherish those memories, thank you for being a part of it.

I would like to thank both Adrian Del Maestro and Bernd Rosenow for the collaboration and for hosting me in their respective universities. It was of great help to me to discuss this fascinating topic together. A special thank to Adrian Del Maestro for answering so clearly and patiently my numerous questions about Luttinger liquids and dissipation in superfluid over the years.

The fabrication of the nanopores would not have been possible without the TEM skills of Jean-Philippe Massé at the Center for Material Microscopy of Polytechnique Montréal. I am also grateful to David Liu who was always available to subsequently image the pores with McGill TEMs. Many thanks as well to Vincent Tabard-Cossa for sharing his knowledge and tips about alternatives to TEM for nanopore fabrication.

A great thank to Richard Talbot, John Smeros and Robert Gagnon for their technical expertise and dedication to help students in a myriad of ways, ranging from CAD design to sample preparation and cleaning procedure, electrical connections, pump maintenance and construction work. I owe you most of my technical knowledge and you enabled me to take initiatives in domains I had initially no clues about. This will serve me for the rest of my life. I am indebted to Pascal Boursequin and Jean-Phillipe Guay for introducing me to precision metal machining. Their training and guidance unraveled a world of opportunities I was unaware of.

I would like to thank Kenneth Ragan for trusting and supporting me on my tutorials experimentations. These accumulated experiences will surely benefit my potential future students! Thanks as well to Juan Gallego for his fast replies and high competence in the IT domain, to Eddie Del Campo for his coffee machine jokes and to Louise Decelles for bringing green touches in the staff-lounge.

I also received a lot of support and motivation from outside the physics department.

The first person I immediately think of is Hélène, my love. Her presence in my life helps me become a better person every day. I am looking forward to live the next chapter of our entangled lives. Then comes my family. I thank them for their moral support and for listening patiently to what probably appeared to them as science gibberish. Thanks to my dad for his tough love, introducing me to science in my early age and generously supporting me throughout my studies. Thanks to my mom for enabling my creativity and for her love. I also wish to thank my godfather for fostering my interest in science and for his numerous visits to Montreal. Finally, I thank my friends from Montreal, Switzerland and around the world for sharing a part of their life paths with me and for all the interesting conversations.

Finally, I would like to acknowledge financial support from Swiss National Foundation through the Doc.mobility fellowship.

STATEMENT OF ORIGINALITY

This thesis reflects my original contribution to condensed matter physics. The previously published results are cited and the following list details my specific contributions:

- *Apparatus*: the low-temperature setup described in section 3.1.1 was already present upon the author's (PFD) arrival. It has been designed and built by Michel Savard (MS) under Guillaume Gervais (GG) supervision. PFD built an entirely new low-temperature setup, described in 3.1.2, based on a modified design of the previous setup. This new experimental setup was mounted on a dry dilution fridge and enabled access to a temperature range lower than the previous one.
- *Sample preparation*: the silicon nitride membranes were purchased from commercial suppliers an the nanopores were drilled and subsequently imaged either by PFD, Matei Petrescu (MP) or by the TEM technician. The handling of the nanopores and the cooldown procedure were performed by PFD.
- *Mass flow measurements*: PFD performed most of the superfluid mass flow measurements in the ∼3 nm radius pore. MP helped with flow measurements in the gas phase and the continuous operation of the helium–3 fridge. MS performed the data acquisition and analysis of the ∼8 nm and ∼20 nm radii pores. PFD was trained to the data acquisition by MS during the measurements of the ∼8 nm pore, which MS presented in his own thesis. The superfluid flow results of the ∼3 nm radius pore and the comparison with previous results

were published as original work with PFD as first author in the American Association for the Advancement of Science (AAAS) open source journal Science Advances (Sci. Adv. 2015;1:e1400222 (2015)).

Contents

LIST OF TABLES

LIST OF FIGURES

LIST OF ACRONYMS

AAAS	American Association for the Advancement of Science. x
AC	Alternating Current. 114
ALD	Atomic Layer Deposition. 69
BCS	Bardeen–Cooper–Schrieffer. 102
BEC	Bose–Einstein Condensate. 34, 39, 120
CAD	Computer-Aided Design. 55, 62, 64
CDW	Charged Density Wave. 14, 18, 28
DC	Direct Current. 4
FL	Fermi liquid. 14, 16, 17, 18, 19, 20, 22, 29
GPIB	General Purpose Interface Bus (computer parallel interface). 81
HfO	Hafnium Oxide. 69
LAMH	Langer–Ambegaokar–McCumber–Halperin. 119
MBE	Molecular-Beam Epitaxy. 2

NIST	National Institute of Standard and Technology. 57, 63, 80
NMR	Nuclear Magnetic Resonance. 3, 4
OFHC	Oxygen-free High Conductivity. 57
PID	Proportional-Integral-Derivative. 55
QMC	quantum Monte Carlo. 3, 31
RG	Renormalization Group. 12
RS-232	Recommended Standard 232 (computer serial interface). 81
RuOx	Ruthenium oxide. 57
SEM	Scanning Electron Microscope. 69
Si_3N_4	Silicon Nitride. 55, 66, 67, 69, 72, 73, 86, 89, 132
STM	Scanning Tunneling Microscope. 2
SVP	Saturated Vapor Pressure. 33, 34, 40, 55, 93, 97, 100, 104, 107, 116, 142
TEM	Transmission Electron Microscope. 67, 69, 72, 79, 86, 89
TL	Tomonaga–Luttinger. 22, 24, 25, 26, 28, 29, 30, 31

TLL Tomonaga–Luttinger Liquid. 1, 3, 31, 33

CHAPTER 1

Introduction

While in modern physics the theoretical approach enjoys the great freedom of choosing the physical constraints on a specific system in order to model it, in experiments one has to craft a system that is as close as possible to the theoretical one, in spite of the many physical constraints imposed by the system.

It is the case of the experiments presented in this thesis, which build on the work initiated by Michel Savard at McGill University [1] and aim to achieve a *one-dimensional (1D) confinement of strongly interacting particles in a quantum fluid*, as schematically illustrated in Fig. 1–1. The motivation for this work stems from seminal theoretical works by Tomonaga [2], Luttinger [3], and Haldane [4] showing that interacting particles in one dimension should exhibit a strikingly different behavior than in two or three dimensions. For example, the Tomonaga–Luttinger Liquid (TLL) theory predicts correlation functions decaying as power laws with exponents controlled by a single parameter depending on the specific interactions of the system considered. Another prediction is that spin and charge excitations occuring in a 1D system should become independent from one another and propagate at different velocities. Moreover, bosons and fermions are predicted to be indistinguishable in one dimension since two particles cannot strickly speaking undergo spacial exchange as a result of the lower dimensionality, and ultimately their hard-core interactions.

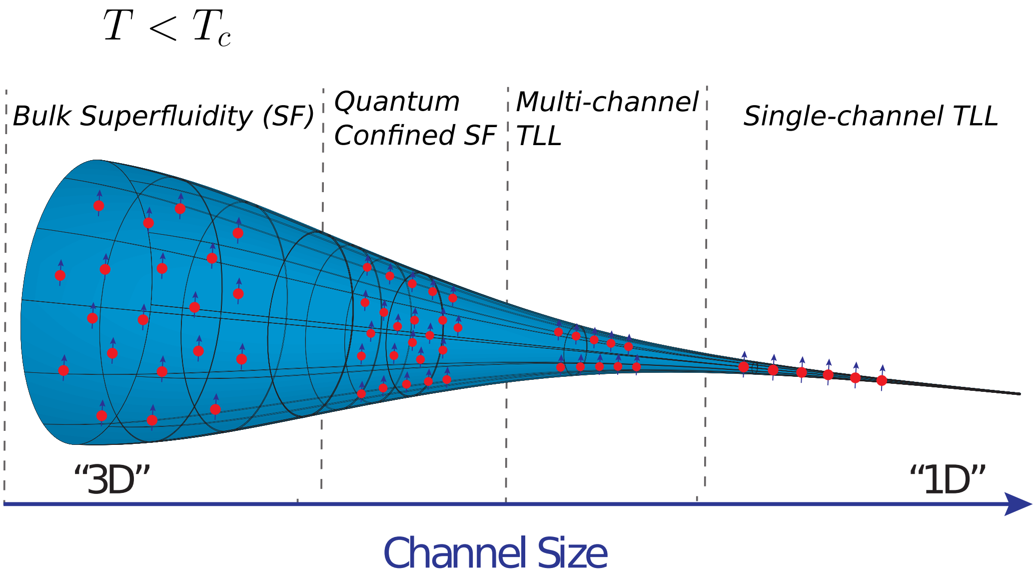

Figure 1–1: Schematic transition from a bulk "3D" state to a confined "1D" state. *Art credits*: Samuel Gaucher.

In general, the dimensionality of a system depends on how the intrinsic length scales of the particles interactions compare to its physical size. In condensed matter physics, a system is said to be in the mesoscopic regime when its size becomes comparable to intrinsic length scales, such as the de Broglie wavelength, or the coherence length of the macroscopic wave function in the case of superfluid ^{4}He [5]. In this regime, quantum effects become important, and can even dominate the physical properties of the system. A good mesoscopic example is the quantization of the electrical conductance in a quasi–one-dimensional wire when its cross-section diameter becomes comparable to the Fermi length of the electron transported through it. When this is the case the conductance exhibits quantum "steps" quantized in units of e^2/h.

The first experiments on one-dimensional systems were only accomplished several decades after the first theoretical predictions in the 1950s [2, 3]. Some of these experimental prouesses have been possible in the past decades, owing to impressive progress in our ability to control matter at the nanoscopic scale thanks to techniques such as Molecular-Beam Epitaxy (MBE) [6] and Scanning Tunneling Microscope (STM) [7]. As of now, several one-dimensional systems have been realized [8–10]. One-dimensional systems for electrons (fermions) were realized with quantum wires consisting of carbon nanotubes [11–14] or semiconductor heterostructures [15–17]. Some organic conductors have been shown to exhibit one-dimensional behavior [18], as well as the quantum spin-ladder material $(C_5H_12N)_2CuBr_4$ under high magnetic field [19, 20]. One-dimensional trapping of particles in low-density bosonic and fermionic systems have also been realized by the cold atom community [21–24].

To this day, an experimental realization of a high-density and strongly interacting one-dimensional bosonic system is still lacking. Helium–4 is an excellent candidate to engineer such a system. Indeed, it was shown to undergo TLL crossover theoretically using a quantum Monte Carlo (QMC) algorithm to simulate ^{4}He atoms confined into a cylindrical channel [25–27]. One of the key advantages of ^{4}He is that it remains liquid even at zero temperatures and so open the door to access the very low energy scales necessary to probe the fascinating physics of TLL. Another advantage of this element is the existence of the Helium–3 fermion isotope, which would allow the investigation of the indistinguishability of bosons and fermions in one dimension.

Previous investigations of helium confined at the nanometer scale have focused on porous media such as in Vycor® [28], and more recently in the zeolites and other mesoporous media [29, 30]. These studies have shown a possible new thermodynamic phase of ^{4}He stabilized at low temperature [29] as well as Nuclear Magnetic Resonance (NMR) signature of a one-dimensional crossover for ^{3}He [30]. While these advances are certainly considerable in the search for a strongly-interacting one-dimensional neutral quantum liquid, their approaches require an extremely large number of nanoscopic channels to gain enough signal for a bulk-probe detection technique.

Our experiment differs much in spirit from those cited above since the ^{4}He atoms are confined inside a *single, nearly cylindrical* pore. This lone pore, or channel, is tailor-made from an amorphous Si_3N_4 membrane that can be fabricated with radii ranging from $R \sim 1$–100 nm [31, 32]. The main advantage of this approach is that there is no *ensemble averaging* over pore distributions and/or potential defects of the sample. Its main drawback, however, is that traditional bulk measurement techniques, such as specific heat or NMR most likely cannot be performed in a single nanopore containing only $\sim 10^4$ to 10^5 helium atoms. Rather, the mass flow through the nanopore is measured with a mass spectrometer, *i.e.* we perform a Direct Current (DC) transport measurement, similar to measuring the conductance of an electrical circuit. To the best of our knowledge, since the 50's, the only other attempt to measure DC flow through a single nanopore was performed subsequent to the first results of our own group, by Prof. Taborek group, in very large aspect-ratio pores fabricated by ion-track etching of polymer or mica foils [33]. The radius of these pores is however one order of magnitude larger than our smallest pore and thus further away from the one-dimensional confinement regime.

In contrast, the measurements of superfluid flow through the smallest nanopore presented in this thesis represent the first glimpse inside the mesoscopic regime. Indeed, in our experiment, several intrinsic ^{4}He length scales such as coherence length, thermal length and de Broglie wavelength become comparable to the pore radius in the temperature range between 1 K and the superfluid transition temperature ($\sim$2.17 K). As a result, the experiment in the smallest nanopore was found to be strikingly different from results obtained in larger pores, both for results from our own group and from those previously reported in the literature [1, 32, 33]

This thesis is organized as following. We provide the necessary theoretical background in chapter 2, and in chapter 3, the experimental methods and apparatus used to perform the measurements are described. Results are reported and analyzed in chapter 4. Finally, the key original contributions of this thesis are summarized in chapter 5, together with some outlooks for future experiments.

References

[1] Savard, M. *Towards a One-Dimensional State of Neutral Matter*. Ph.D. thesis, McGill University (2014). `http://gervaislab.mcgill.ca/Savard_PhD_Thesis.pdf`.

[2] Tomonaga, S.-I. *Progr. Theor. Phys.* **5**, 544–569 (1950).

[3] Luttinger, J. M. *J. Math. Phys.* **4**, 1154–1162 (1963).

[4] Haldane, F. D. M. *J. Phys. C: Solid State Phys.* **14**, 2585–2609 (1981).

[5] Ando, T., Arakawa, Y., Furuya, K., Komiyama, S. & H., N. *Mesoscopic physics and electronics* (Springer, Amsterdam, 1998).

[6] Herman, M. A. & Sitter, H. *Molecular Beam Epitaxy* (Springer, Berlin, 1996).

[7] Binnig, G., Rohrer, H., Gerber, C. & Weibel, E. *Phys. Rev. Lett.* **49**, 57–61 (1982).

[8] Deshpande, V., Bockrath, M., Glazman, L. I. & Yacoby, A. *Nature* **464**, 209–216 (2010).

[9] Giamarchi, T. *Int. J. Mod. Phys. B* **26**, 1244004 (2012).

[10] Giamarchi, T. *C. R. Phys.* **17**, 322–331 (2016).

[11] Bockrath, M. *et al. Nature* **397**, 598–601 (1999).

[12] Ishii, H. *et al. Nature* **426**, 540–544 (2003).

[13] Chudow, J. D., Santavicca, D. F. & Prober, D. E. *Nano Lett.* **16**, 4909–4916 (2016).

[14] Zhao, S. *et al. Phys. Rev. Lett.* **121**, 047702 (2018).

[15] Auslaender, O. M. *et al. Science* **308**, 88–92 (2005).

[16] Steinberg, H. *et al. Nature Phys.* **4**, 116–119 (2007).

[17] Laroche, D., Gervais, G., Lilly, M. P. & Reno, J. L. *Science* **343**, 631–634 (2014).

[18] Schwartz, A. *et al.* *Phys. Rev. B* **58**, 1261–1271 (1998).

[19] Thielemann, B. *et al.* *Phys. Rev. Lett.* **102**, 107204 (2009).

[20] Povarov, K. Y., Schmidiger, D., Reynolds, N., Bewley, R. & Zheludev, A. *Phys. Rev. B* **91**, 020406 (2015).

[21] Greiner, M., Bloch, I., Mandel, O., Hänsch, T. W. & Esslinger, T. *Phys. Rev. Lett.* **87**, 160405 (2001).

[22] Görlitz, A. *et al.* *Phys. Rev. Lett.* **87**, 130402 (2001).

[23] Schreck, F. *et al.* *Phys. Rev. Lett.* **87**, 080403 (2001).

[24] Haller, E. *et al.* *Nature* **466**, 597–600 (2010).

[25] Del Maestro, A. & Affleck, I. *Phys. Rev. B* **82**, 060515 (2010).

[26] Del Maestro, A., Boninsegni, M. & Affleck, I. *Phys. Rev. Lett.* **106**, 105303 (2011).

[27] Kulchytskyy, B., Gervais, G. & Del Maestro, A. *Phys. Rev. B* **88**, 064512 (2013).

[28] Zassenhaus, G. M. & Reppy, J. D. *Phys. Rev. Lett.* **83**, 4800–4803 (1999).

[29] Taniguchi, J., Demura, K. & Suzuki, M. *Phys. Rev. B* **88** (2013).

[30] Yager, B. *et al.* *Phys. Rev. Lett.* **111** (2013).

[31] Savard, M., Tremblay-Darveau, C. & Gervais, G. *Phys. Rev. Lett.* **103**, 104502 (2009).

[32] Savard, M., Dauphinais, G. & Gervais, G. *Phys. Rev. Lett.* **107**, 254501 (2011).

[33] Velasco, A. E., Yang, C., Siwy, Z. S., Toimil-Molares, M. E. & Taborek, P. *Appl. Phys. Lett.* **105**, 033101 (2014).

CHAPTER 2

Theoretical background

In this chapter, we will first introduce a general terminology of phase transitions so as to discuss the superfluid phase transition of bulk ^{4}He in the last section. Next, we will discuss the Fermi liquid model for correlated fermions and show how it dramatically fails in one dimension. We will then introduce the Tomonaga–Luttinger and the Tomonaga–Luttinger liquid models which can successfully capture the physics of both bosons and fermions in one dimension. Finally, we will discuss the properties of the superfluid phase transition of ^{4}He, of the utmost importance to chapter 4.

2.1 Phase transitions and criticality

The aim of this section is to provide the reader with basic knowledge of some important concepts about phase transitions and critical phenomena that will be used throughout this thesis. We will focus on transitions between two distinct phases, and the importance of dimensionality in the context of phase transitions will be discussed.

One way to introduce phase transitions at the conceptual level is to consider the Helmoltz free energy F of a system,

$$F(T,V,N) = E(S,V,N) - TS, \tag{2.1}$$

where E is the internal energy of the system which depends on the entropy S, the volume V and the particle number N, and T is the temperature. At high[1] fixed temperature and volume, increasing the entropy of the system decreases its free energy F and it thus favors disordered states. Depending on the system, there might exist a finite *critical temperature* T_c under which the internal energy term dominates and for which the entropy does not influence anymore the free energy. This flags a phase transition from a disordered phase towards an ordered phase[2]. Exactly at T_c, there is no difference between the two phases. However any departure from T_c will lead, in the ideal case, to the equilibrium of one or the other phase only [1]. This critical temperature is determined by the microscopic interactions responsible for the ordered phase and is not an universal quantity [2].

The phases on both sides of a transition are characterized by one or several order parameters, φ_i. An order parameter is a variable which is usually equal to zero in one phase and non-zero in the other phase. One example of such order parameter is the difference between the density ρ and the specific gas density ρ_G, $\varphi = \rho - \rho_G$, at the liquid-gas transition. Another example is the thermodynamic average of the spontaneous magnetization $\varphi \simeq \langle \vec{m} \rangle$ in the paramagnetic-ferromagnetic phase transition. An illustration of the magnetization as a function of temperature is shown in Fig. 2–1. In certain cases, such as the ferromagnetic one, the symmetry of the ordered phase is lower than that of the paramagnetic disordered phase. In the paramagnetic phase, the system is invariant under uniform rotation of all spins.

---

[1] High temperature here means higher than a phase transition temperature provided such a temperature exists. This will become clear later in the text.

[2] T_c is referred as the critical transition temperature.

However, in the ferromagnetic phase, this symmetry is broken in the system since only two configurations are now preferred : most spins up or most spins down. This is referred to as a *spontaneous symmetry breaking* phase transition.

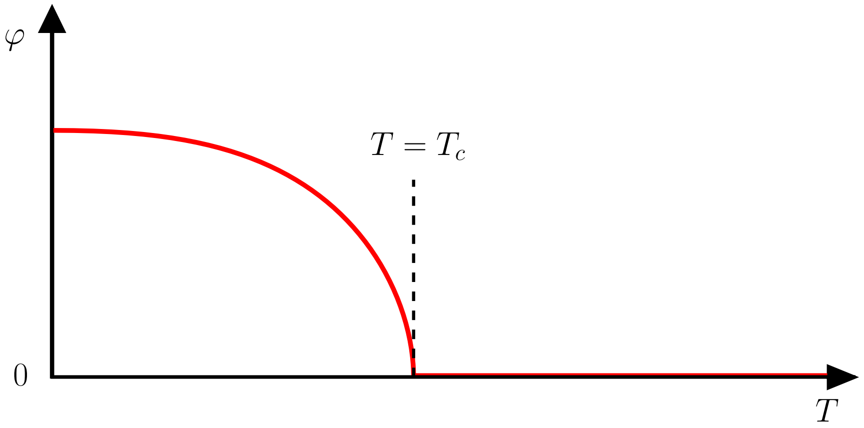

Figure 2–1: Typical example of ferromagnetic phase transition at T_c. The magnetization $\varphi \simeq \langle \vec{m} \rangle$ is the order parameter and it varies as a function of temperature. Its value is zero above T_c, and finite below T_c. This is an example of higher-order phase transition as the order parameter value increases continuously across the transition.

The thermodynamic properties of a system near a phase transition can be described by one of its thermodynamical potentials near the transition. Here, we will consider F as our potential. It is usually assumed that the free energy is an analytic function of the temperature T and of the order parameters $\{\varphi_i\}$ [3]. Phase transitions for which $\frac{\partial F}{\partial T}$ is discontinuous are referred to as *first-order phase transitions*, such as the celebrated liquid-gas transition. Our focus throughout the thesis will consist mainly on phase transitions for which $\frac{\partial^2 F}{\partial T^2}$ is discontinuous or infinite while $\frac{\partial F}{\partial T}$ is continuous. These transitions are referred to as *higher-order* or *continuous* phase transitions [4]. The higher-order phase transitions can also be characterized by a continuous behavior of the order parameter as a function of the temperature whereas the order parameter jumps from zero to a finite value at T_c for first-order transitions.

An important characteristic of the ordered phase is the existence of long-range correlations of its order parameter. For example, in the case of the ferromagnetic phase, the correlation between the magnetization of two different regions has a finite value when the distance between the two regions tends to infinity. This is called long-range order and is in general true for any dimension larger than two. Mermin and Wagner's theorem predicts that in two-dimensional systems with short range interactions and continuous symmetry, the correlations are algebraically suppressed with distance by thermal fluctuations for any finite temperature $(T > 0)$. This leads to a quasi–long-range order and prevents a phase transition to an ordered state [5]. However, at $T = 0$, the two-dimensional case with continuous symmetry can still exhibit a long-range order and therefore a phase transition to an ordered phase at $T_c = 0$ is possible. In contrast, for the one-dimensional case, thermal fluctuations lead to an exponential decay of the correlations as a function of distance. This holds true even at $T = 0$ for classical models, and so it precludes any phase transition. One-dimensional quantum systems will be covered further in section 2.3.

In a ferromagnet, the overall non-zero magnetization arises because spins separated by large distances align in a coherent fashion below the transition temperature T_c. The distance over which spin fluctuations are correlated is called the correlation length $\xi(T)$, and it has the property to become infinite at the critical temperature, *i.e.* $\xi(T \to T_c) \to \infty$. One striking characteristic of the correlation length, and of many other thermodynamic functions such as the specific heat or the magnetic susceptibility, is its power law behavior controlled by critical exponents near T_c. Such critical exponents for a generic function f with a single order parameter φ, $f(t,\varphi)$, where $t \equiv \frac{T-T_c}{T_c}$ is the reduced temperature, is defined as

$$\lambda^{\pm} \equiv \lim_{t\to 0} \frac{\ln f(t)}{\ln(\pm t)}, \tag{2.2}$$

where $f(t) \equiv f(t, \varphi = 0)$ and "+/−" stands for approaching the transition from above/below T_c. We note that as the order parameter goes to zero, a similar definition can be set for $f(\varphi) \equiv f(t = 0, \varphi)$, yielding another critical exponent.

The different critical exponents are related via fundamental thermodynamic inequalities, known as *scaling relations*. A possible route to retrieve the relations is to invoke the *scaling hypothesis* [1]. This hypothesis assumes that the singular part of the thermodynamic potential near the critical point is a generalized homogeneous function, *i.e.* it satisfies

$$f(L^{a_t} t, L^{a_\varphi} \varphi) = L f(t,\varphi), \tag{2.3}$$

where $L \in \mathbb{R}_+^*$ and a_t, $a_\varphi \in \mathbb{R}$. This property is extensible to Legendre transforms or derivatives of $f(t,\varphi)$ and thus all thermodynamic functions are generalized homogeneous functions if the scaling hypothesis holds [6]. The relations between a_t, a_φ and all the critical exponents can then be found using the property in Eq. (2.3). Therefore, the values of only two critical exponents are required to determine all others. Thanks to *Renormalization Group* (RG) theory, the scaling hypothesis has been shown to be valid in the vicinity of T_c. Using RG theory, the critical exponents can be estimated numerically, and are found in good agreement with their experimental values [7]. A full description of RG theory goes beyond the scope of this thesis, however we point the following reviews on the subject [6–8] to the interested reader.

Many examples of ferromagnetic phase transitions can be covered by a class of interacting classical spins models, called the n-vector or O(n) model, and are described by the following Hamiltonian,

$$\mathcal{H} = -J \sum_{\langle i,j \rangle} \vec{S}_i \cdot \vec{S}_j. \tag{2.4}$$

Here, $\vec{S}_i$ are n-component spin vectors and $J \in \mathbb{R}$ sets the energy scale of the interaction. In particular, the case with $n = 2$ is called the XY model[3]. This special case has two-component order parameter and shares the same critical exponents as superfluid ^{4}He. It means that the critical exponents are independent of the microscopic details of the system. Since they describe a universal behavior of very different systems near their critical points, these critical exponents are referred to as *universal exponents* and different systems are then said to belong to the same *universality class* [8].

---

[3] $n = 1$ corresponds to the Ising model and $n = 3$ to the Heisenberg model.

2.2 Fermi liquid theory in three and two dimensions

In 1957, Lev Davidovich Landau developed his famous *Fermi liquid* (FL) theory [9], a model for interacting fermions which is asymptotically exact for excitations at low energies and long-wavelengths. This model has been extremely successful at describing electrons in most metals, as well as atoms in non-superfluid liquid ^{3}He. The FL model however fails to describe any quantum phase which involves symmetry breaking. Examples of such quantum phases are Wigner crystals and Charged Density Waves (CDW) for which translational symmetry is broken [10, 11]. Quantum Hall effects and itinerant magnetism also lack time-reversal symmetry [12]. Materials exhibiting superconductor or superfluid behavior break global gauge symmetry. Furthermore, FL theory also breaks down in one-dimensional systems. This current section will provide a brief introduction of the FL theory, and in next section we will discuss the one-dimensional case.

The starting point of FL theory is a set of non-interacting fermions whose momentum distribution is given by Fermi statistics, *i.e.* a *Fermi gas* [13]. At zero temperature ($T = 0$), all energy states are occupied up to an energy labeled as the *Fermi energy*[4], E_F. In terms of momentum, all states with momentum k below k_F ($E_\mathrm{F} = \hbar^2 k_\mathrm{F}^2/2m$), the *Fermi momentum*, are occupied[5] and all states above k_F are empty[6]. In momentum space the *Fermi surface* corresponds to a surface spanned

---

[4] $E_\mathrm{F} = \mu(T = 0)$, where $\mu(T)$ is the chemical potential in the Fermi distribution.

[5] This set of states is called the *Fermi sea.*

[6] From here and until section 2.4, $\hbar = 1$.

by k-vectors for which $E(k) = E_{\mathrm{F}}$. A Fermi surface of free fermions is illustrated in Fig. 2–2.

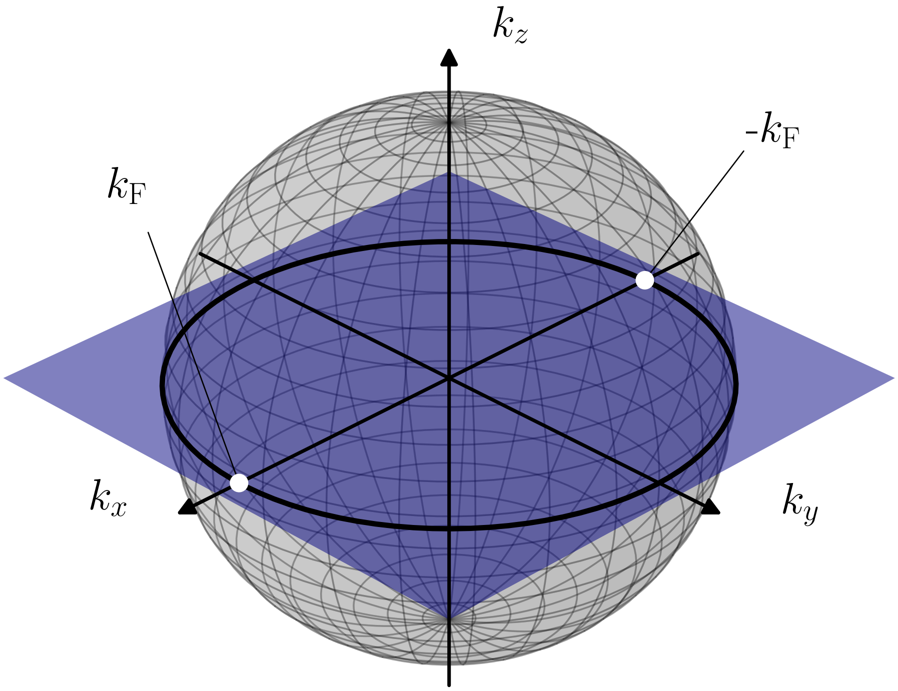

Figure 2–2: Fermi surfaces of free fermions in several dimensions, with quadratic dispersion $E(k) = k^2/2m$. The sphere corresponds to a 3D Fermi surface, with k having 3 components. The solid line circle from the intersection of the sphere and the k_x-k_y plane forms a 2D Fermi surface, with k having two components. The two white dots located at $\pm k_{\mathrm{F}}$ on k_x represent a 1D Fermi "surface", where k has only one component.

The momentum distribution of the Fermi gas is represented by the dashed line shown in Fig. 2–3 (A). The departure from the Fermi gas model is obtained by switching on fermion-fermion interactions adiabatically. These interactions modify the free energy of the system and as a result, change the momentum distribution. A simple approach to this complex many-body problem is to construct a mean-field theory by averaging out the individual interactions into a term that renormalizes the energy. Importantly, it can be shown that the momentum distribution of the free particles is only slightly modified near k_{F}. The solid line in Fig. 2–3 (A) shows the effect of such interactions. The excitations in the mean-field model can be described by quasi-particles with well-defined momentum, charge and spin, within a one-to-one correspondence with the free fermions in the adiabaticity limit [9, 14]. The energy-momentum dispersion relation for these quasi-particle excitations is displayed in Fig. 2–3 (B).

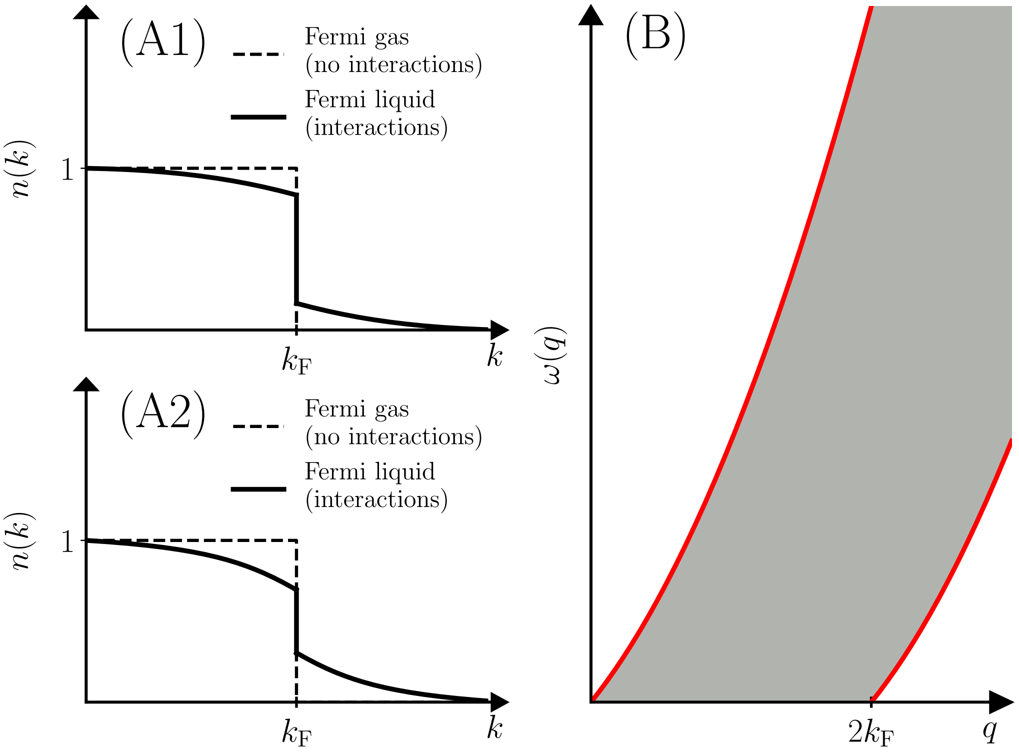

Figure 2–3: **(A1-A2)** Momentum distributions of free fermions in the cases of a Fermi gas (dashed line) and a Fermi liquid (solid line). **(A1)** For weak interactions, the jump at k_{F} is still close to one. **(A2)** For stronger interactions the jump at k_{F} becomes smaller. **(B)** Positive momentum part of fermion-hole excitation spectrum of three, or two–dimensional free fermions. The shaded area is the excited states continuum. The solid red line corresponds to fermion-hole excitations for which $k_{hole} = \pm(k_{\mathrm{F}} + \delta)$, with $\delta \ll 1$. *Based on* [15].

The FL theory is thus a Fermi gas description of quasi-particles containing the interactions. The thermodynamic properties are hence similar, with only parameters such as the effective mass being renormalized by interactions. For this model to hold, it is essential for the momentum of these quasi-particles to remain well-defined. Landau has shown theoretically that it is indeed the case in three dimensions, provided their energy remains small compared to the Fermi energy, *i.e* in the low-energy limit, and their momentum small, *i.e.* long-wavelength limit [9]. The fact that the Fermi energy of most metals is on the order of 10^4 K explains why this model can successfully be applied so broadly [16].

In two dimensions, there are not a large variety of examples where the FL picture fails without explicit symmetry breaking [17]. The few breakdowns were only found in theoretical lattice models. Anderson suggested that the strongly coupled 2D Hubbard model could be an example of failure of the FL description [18, 19]. Some other work reached a similar conclusion [20, 21]. However for the same model in the low electron density limit (weak coupling), the FL picture was shown to be valid [17, 22]. One reason put forth by Anderson for the breakdown of the FL model was the similarities between the 2D Hubbard model at half-filling and one-dimensional fermionic models. This now leads us to the next section where we discuss why the FL picture fails in 1D and what other model could provide a good description for the low-energy, long-wavelengths excitations of the system.

2.3 One-dimensional systems

The one-dimensional case is truly special since it can be described by models with exact analytical solutions, thanks to the relative simplicity brought by reducing the number of degrees-of-freedom. The problem of correlated fermions or bosons in 1D was first tackled as a theoretical problem and remained theoretical for a long time. The level of technical expertise required to craft one-dimensional systems experimentally has only recently become available, and as of today it remains a formidable challenge. These experimental aspects will be described in detail later in chapter 3, and here onwards the focus will remain theoretical. We will first explain why the FL theory breaks down in 1D due to the *Peierls instability* and then we will describe the *Tomonaga–Luttinger* model as its replacement. Finally we will introduce the *Tomonaga–Luttinger liquid* as an extension of the *Tomonaga–Luttinger* model to account for more realistic systems.

Our emphasis is put on extracting the physics behind the model in the hope to provide the reader with an intuitive understanding. While the mathematical description of the model will be introduced, efforts have been purposely made to focus on the concepts. The reader interested in the numerous mathematical details can find them in the following reviews, [14–16].

2.3.1 Failure of Fermi liquid theory

FL theory fails in one-dimensional systems due to a phenomenon referred to as *Peierls instability.* Peierls showed that a periodic potential of periodicity q in momentum space applied to a free electron gas would open a gap at $\pm\frac{1}{2}q$ in the electron bands modulated by this potential [11]. In the one-dimensional case, if the potential is $q = 2k_{\mathrm{F}}$ periodic, the gap opens exactly at the Fermi surface. This in turns prevents the excitation of low-energy quasi-particle bound states, a concept at the core the FL model. Such a potential could be realized by electron-phonon interactions as illustrated in Fig. 2–4 leading to CDW. Another justification for the breakdown of the FL theory is that the CDW break translational symmetry and FL being a mean-field theory, it cannot break any symmetry.

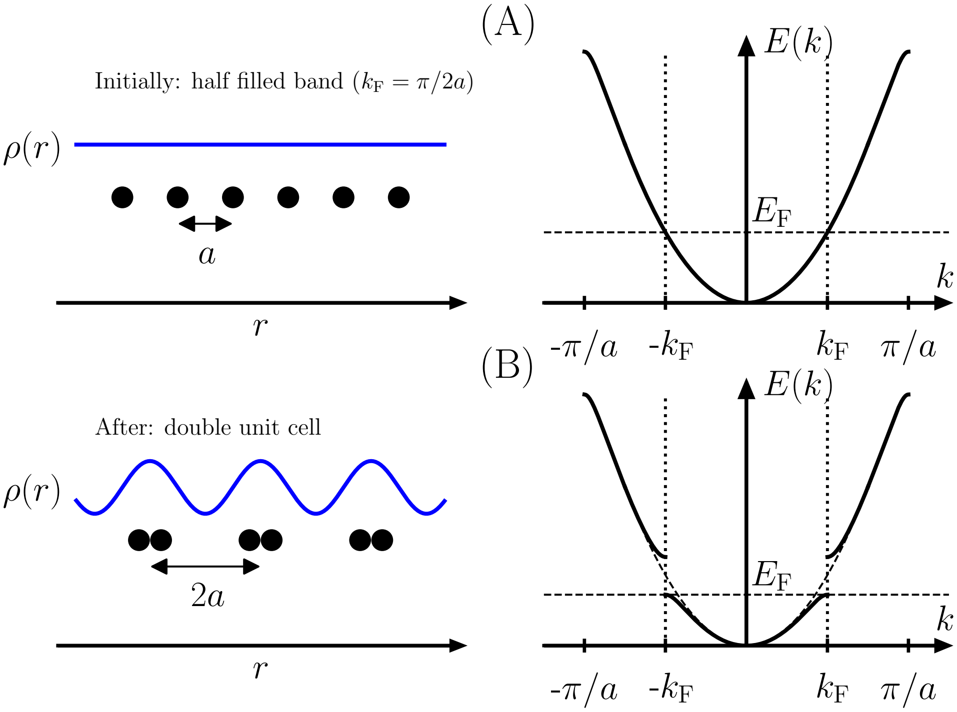

Figure 2–4: **(A)** N atoms are homogeneously spread in a lattice of spacing a as shown on the left panel. Each atom possesses a weakly bound electron which can occupy two states. The density of states is then $n = \frac{1}{2}\frac{2\pi}{L} = \frac{\pi}{Na}$ where L is the size of the lattice. If the band is half-filled, *i.e.* $n = \frac{2k_F}{N}$, then $k_F = \frac{\pi}{2a}$. **(B)** Attractive interactions can distort the lattice as shown in the left panel. In this example the lattice spacing is doubled. The right panel shows a band gap opening at $\frac{\pi}{2a}$, at the Fermi wavevector, k_F. The energy cost of the lattice distortion is offset by the reduced kinetic energy of the electrons at the edge of the band. The excitations close to the Fermi surface are now gapped and the FL description fails. *Source*: Quantum condensed matter lectures by Aashish Clark at McGill University.

2.3.2 A replacement model : Tomonaga–Luttinger model

In one-dimensional systems, the Fermi surface reduces to only two points ($\pm k_{\mathrm{F}}$), as displayed in Fig. 2–2. The energy dispersion relation of free fermions $E(k)$ is illustrated in Fig. 2–5 (A). The dispersion relation of the excitations $\omega(q)$ is shown

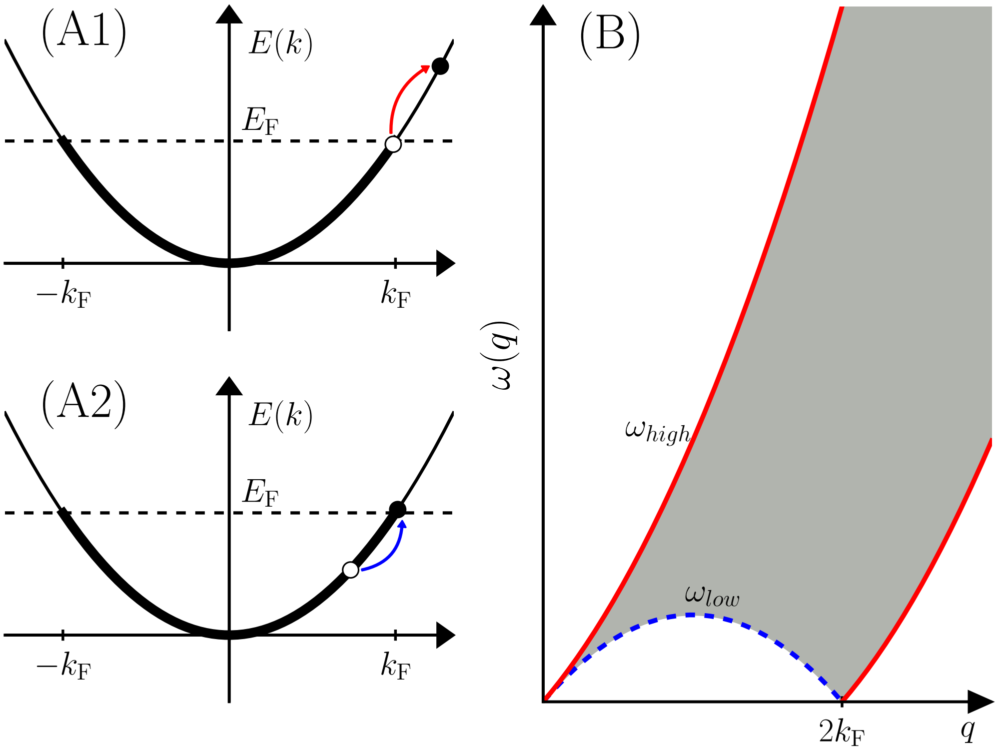

Figure 2–5: **(A1-A2)** Energy dispersion relation for one-dimensional free fermions. The fermions in the ground state lie on the solid line below E_{F}. **(A1)** Example of fermion-hole excitation with momentum q and energy $\omega(q)$, corresponding to the solid red line (ω_{high}) starting at $q = 0$ in (B). **(A2)** Example of fermion-hole excitation with momentum q and energy $\omega(q)$, corresponding to the dashed blue line (ω_{low}) in (B). **(B)** Positive momentum part of fermion-hole excitation spectrum of one-dimensional free fermions. The shaded area represents the excited states continuum. Note the absence of low-energy states away from $q = 0$ or $q = 2k_{\mathrm{F}}$. The solid red lines (ω_{high}) correspond to fermion-hole excitations for which $k_{hole} = \pm(k_{\mathrm{F}} + \delta)$, with $\delta \ll 1$. The dashed blue line (ω_{low}) corresponds to fermion-hole excitations for which $k_{fermion} = k_{\mathrm{F}} + \delta$. *Based on* [23, 24].

in Fig. 2–5 (B). The comparison of this excitation spectrum with the excitation spectrum of the 3D FL displayed in Fig. 2–3 (B) provides an intuitive idea of why FL theory cannot be accurate in 1D: at low-energy, there is no continuum of states with momentum larger than zero to accommodate a quasi-particle description of the excitations. Low energy excitations are only available close to momenta transfer $q = 0$ and $q = 2k_\mathrm{F}$. Therefore, the low-energy excitations consist solely of left ($k \simeq -k_\mathrm{F}$), or right movers ($k \simeq +k_\mathrm{F}$).

In 1950, Tomonaga introduced a model of interacting one-dimensional spinless fermions which was based on the linearization of the energy dispersion relation near

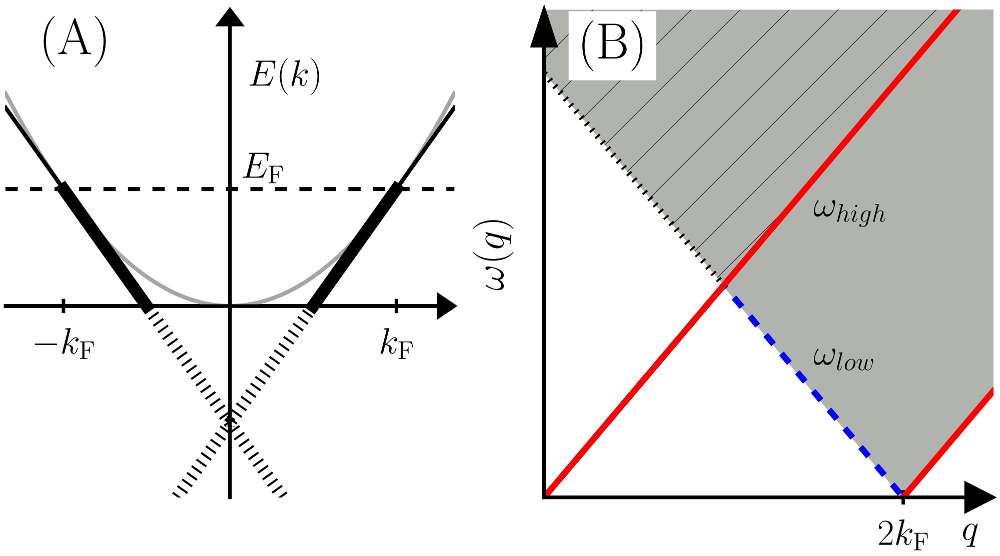

Figure 2–6: **(A)** Linearized energy dispersion relation for one-dimensional free fermions. The possible states only lie on the solid line below E_F. The dotted line corresponds to unphysical negative energy states created by the linear approximation. The grey line represents the one-dimensional free fermions energy dispersion relation. **(B)** Positive part of fermion-hole excitation spectrum based on the energy dispersion relation shown in (A). The shaded area represents the excited states continuum. Note that the hashed area corresponds to excitations of the unphysical negative energy states. The solid red lines (ω_{high}) correspond to fermion-hole excitations for which $k_{hole} = \pm(k_\mathrm{F} \mp \delta)$, with ($\delta \ll 1$). The dashed blue line (ω_{low}) corresponds to fermion-hole excitations for which $k_{fermion} = k_\mathrm{F} + \delta$. *Based on* [24].

the Fermi points [25]. The linearized dispersion relation can be seen in Fig. 2–6 (A). While simplifying the mathematical treatment, this modified dispersion gives rise to an unphysical infinite number of negative energy states, represented by the dotted line in Fig. 2–6 (A). Tomonaga had originally introduced cutoffs to tackle this problem. Unfortunately, these cutoffs prevented the derivation of an exact solution of the model [14]. A similar model was developed independently by Luttinger a decade later [26]. Unlike the Tomonaga model, the Luttinger model is based on the whole range of momentum vectors k from ∞ to $-\infty$. To acknowledge Tomonaga's earlier work, the model has been coined the *Tomonaga–Luttinger* model.

In the Tomonaga–Luttinger (TL) model, the linearized energy dispersion near the Fermi points is given by

$$E_r(k) = v_{\mathrm{F}}(rk - k_{\mathrm{F}}) + E_{\mathrm{F}}, \tag{2.5}$$

where $v_{\mathrm{F}} = \left.\frac{\partial E(k)}{\partial k}\right|_{k=k_{\mathrm{F}}}$ is the Fermi velocity and $r = \pm$ is used to refer to the right $(r = +)$ and left $(r = -)$ branches of the energy dispersion relation close to k_{F}. Therefore, the energy $\varepsilon_r(q)$ of a fermion-hole pair excitation with momentum q is given by[7]

$$\varepsilon_r(q) = E_r(k+q) - E_r(k) = r v_{\mathrm{F}} q. \tag{2.6}$$

This dispersion relation is similar to that of a sound wave (*i.e.* a collective mode excitation). The fact that it is independent of k provides another justification for the failure of the quasi-particle description of the FL model as k is no longer a good quantum number to label excited states [15].

---

[7] $\omega(q) = \varepsilon_r(|q|)$ in Figs. 2–5 (B) and 2–6 (B).

In order to build a model that includes interactions between fermion-hole pairs, one has to consider scattering processes between the pairs. The simplest model only accounts for scattering processes which conserve both energy and momentum of the lattice. Those are limited to the four cases displayed in Fig. 2–7 : forward[8] scattering of particles on different branches ($\mathcal{H}_2$), forward scattering of two particles on the same branch ($\mathcal{H}_4$), backscattering of particles on different branches ($\mathcal{H}_1$) and Umklapp processes ($\mathcal{H}_3$). The $\mathcal{H}_1$ and $\mathcal{H}_3$ processes were not included in the TL model originally as its focus was on the low momentum ($q \ll k_{\mathrm{F}}$) and low-energy ($\varepsilon_r(q) \ll v_{\mathrm{F}} k_{\mathrm{F}}$) excitations. However they will be discussed briefly towards the end of this section.

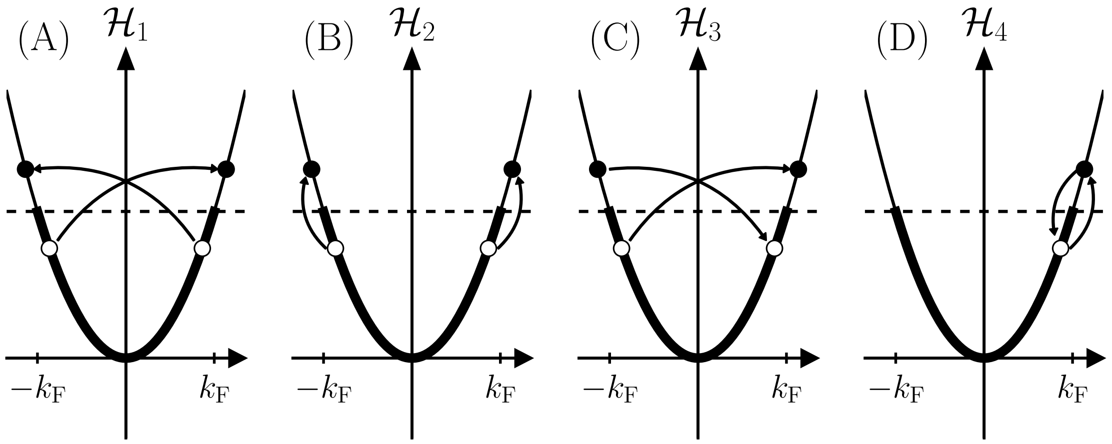

Figure 2–7: Spinless scattering processes conserving energy and momentum of the lattice. The processes are illustrated on a one-dimensional energy dispersion relation. The dashed horizontal line corresponds to E_{F}. **(A)** Backscattering of particles on different branches. **(B)** Forward scattering of particles on different branches. **(C)** Umklapp process. **(D)** Forward scattering of particles on the same branch, this process also occur on the $r = -$ branch but was only illustrated on the $r = +$ side. *Based on* [14].

---

[8] Forward means that the momentum of each scattered particle does not change sign upon interaction.

The Hamiltonian of the TL model consists of three distinct terms

$$\mathcal{H}^{T-L} = \mathcal{H}_0 + \mathcal{H}_2 + \mathcal{H}_4, \tag{2.7}$$

where $\mathcal{H}_0$ in Eq. (2.9) is the kinetic term and $\mathcal{H}_2$ in Eq. (2.10), $\mathcal{H}_4$ in Eq. (2.11) are the two forward scattering terms.

In the spinless case, the Hamiltonian can be expressed in terms of a fermionic density operator

$$\rho_r(q) = \sum_k : c^\dagger_{r,k+q} c_{r,k} := \rho^\dagger_r(-q), \tag{2.8}$$

where $c_{r,k}$ is a destruction operator of a fermion with momentum k located on branch r and : ... : denotes normal ordering of the operators.

Using Eq. (2.8), the terms of Eq. (2.7) reads

$$\mathcal{H}_0 = \frac{2\pi v_\mathrm{F}}{L} \sum_{r=\pm} \sum_{q>0} \rho_r(rq)\rho_r(-rq), \tag{2.9}$$

$$\mathcal{H}_2 = \frac{1}{L} \sum_q g_2 \rho_+(q)\rho_-(-q), \tag{2.10}$$

$$\mathcal{H}_4 = \frac{1}{2L} \sum_q g_4 \left[\rho_+(q)\rho_+(-q) + \rho_-(q)\rho_-(-q)\right]. \tag{2.11}$$

Here, the parameters g_2 and g_4 control the strength of the respective interactions, and the $\mathcal{H}_2$ term gives rise to fermion-hole pairs excitations out of the Fermi sea. It does not commute with $\mathcal{H}_0$ and is responsible for scattering of fermion-hole pairs at arbitrarily small momentum. On the other hand, the $\mathcal{H}_4$ term commutes with the kinetic term and, as a result, it does not create excitations above the ground state but it lifts the degeneracies present in excited states [14, 16]. This is best expressed by the renormalization of the collective mode's velocity in Eq. (2.6) in terms of the coupling strength parameter g_4,

$$v_S = v_\mathrm{F}\left(1 + \frac{g_4}{\pi v_\mathrm{F}}\right). \tag{2.12}$$

Remarkably, the Hamiltonian of the TL model can be solved exactly, *i.e.* it can be written in a quadratic form of bosonic operators by means of a Bogoliubov transformation. The mathematical details of the procedure can be found in Refs. [14–16, 27]. The final form is not presented here as it does not add much physical insights. Rather, we discuss another approach introduced by Haldane in which the TL Hamiltonian employs a particle field bosonic operator $\Psi(x)$ [24]. This operator is defined by two canonical conjugate fields[9] $\theta_N(x)$ and $\theta_J(x)$,

$$\Psi^\dagger(x) \sim \sqrt{\partial_x \theta_N(x)}\, e^{i\theta_J(x)}, \tag{2.13}$$

where $\partial_x \theta_N(x)$ corresponds to the $q \simeq 0$ part of density fluctuations at point x, and $\partial_x \theta_J(x)$ is proportional to the difference between the left and right movers [16, 28]. Within this prescription, the TL Hamiltonian is now given in terms of two fields,

$$\mathcal{H}^{T-L} = \frac{1}{2\pi}\int \mathrm{d}x\,[v_N(\partial_x\theta_N(x))^2 + v_J(\partial_x\theta_J(x))^2\,], \tag{2.14}$$

or,

$$\mathcal{H}^{T-L} = \frac{v_S}{2\pi}\int \mathrm{d}x\,[K(\partial_x\theta_N(x))^2 + \frac{1}{K}(\partial_x\theta_J(x))^2\,], \tag{2.15}$$

where

$$v_S = \sqrt{\left(v_\mathrm{F} + \frac{g_4}{\pi}\right)^2 - \left(\frac{g_2}{\pi}\right)^2} = \sqrt{v_N v_J}, \tag{2.16}$$

---

[9] *i.e.*, they obey the relation $[\theta_J(x'), \partial_x\theta_N(x)] = i\pi\delta(x' - x)$.

and

$$K = \sqrt{\frac{\pi v_{\mathrm{F}} + g_4 + g_2}{\pi v_{\mathrm{F}} + g_4 - g_2}}, \tag{2.17}$$

$$v_N = v_S K \text{ and } v_J = \frac{v_S}{K}. \tag{2.18}$$

Notably, this Hamiltonian can be diagonalized by a Bogoliubov transformation. The formulation given in Eq. (2.14) is extremely concise and provides an explicit description of the elementary low-energy excitations allowed in the TL model, *i.e.* the collective density fluctuations (controlled by v_S, the phonon modes), the charge excitations (controlled by v_N) and the current excitations (controlled by v_J) [24]. The integer numbers N and J are also both good quantum numbers. They represent the symmetric and anti-symmetric parts in the left-right movers description : N is proportional to $N_+ + N_-$, and J is proportional to $N_+ - N_-$. The physical interpretation of N is the total electronic charge, whereas J is related to the average current $j = v_J \frac{J}{L}$, where L is the size of the system. Those two quantities are conserved in the TL model as the number of right (N_+) and left (N_-) movers are conserved quantities because they commute with the Hamiltonian [14],

$$[N_\pm, \mathcal{H}^{T-L}] = 0. \tag{2.19}$$

This can also be viewed as the consequence of the symmetries of the $\mathcal{H}_2$ and $\mathcal{H}_4$ scattering processes. The addition of the $\mathcal{H}_1$ and $\mathcal{H}_3$ scattering processes will no longer conserve N and J because they break these symmetries.

The Hamiltonian given in Eq. (2.15) is a different reformulation of Eq. (2.14) that defines a dimensionless parameter K called "Luttinger parameter"[10] in Eq. (2.17). This parameter encompasses the physics of the interactions induced by g_2 and g_4. A value of $K = 1$ describes the non-interacting case. If $K > 1$, interactions are repulsive and if $K < 1$, they are attractive. At $T = 0$, it can be shown that K describes a crossover from a superfluid state ($K = 0$) to a state with solid order ($K \to \infty$) [28], as illustrated in Fig. 2–8. Importantly, K also controls the algebraic decay[11] properties of correlation functions which will be briefly discussed at the end of this section.

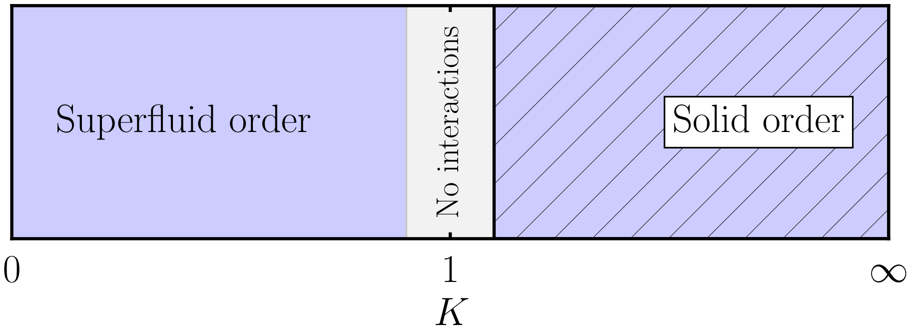

Figure 2–8: Physical interpretation of the Luttinger parameter K at $T = 0$.

So far we have only considered the spinless case. In order to take the spin into consideration, the operators have to be modified to avoid a violation of the Pauli principle during fermionic scattering processes. An explicit description of these operators goes beyond the scope of this thesis, and so we only provide here a short

---

[10] This parameter is not defined uniquely across the literature. The definition presented here is from [24] but some reviews use $\frac{1}{K}$ as K [14–16].

[11] *i.e.* the correlations decay as a power law of the distance. It is slower than exponential decay.

discussion. The Hamiltonian with spin can be diagonalized by way of a Bogoliubov transformation and the interesting outcome is that its formulation then explicits separation of spin and charge excitations. This spinful Hamiltonian is written as a sum of two independent quadratic terms

$$\mathcal{H}^{T-L} = \mathcal{H}_{\rho}^{T-L} + \mathcal{H}_{\sigma}^{T-L}, \tag{2.20}$$

respectively for the charge (CDW) and spin (SDW) collective excitations. These collective excitations propagate at different velocities and give rise to the phenomenon of spin-charge separation. The relations in Eqs. (2.16), (2.17) and (2.18) are still valid, however the parameters g_2 and g_4 now have different values for spin and charge excitations[12].

One way to illustrate this separation is to consider an anti-ferromagnetic spin chain, as displayed in Fig. 2–9. Note that the spin-charge separation arises directly from the conservations of the charge and spin of the right and left movers. This would not hold if Umklapp processes ($\mathcal{H}_3$) were enabled [15, 29].

In addition to the fascinating spin-charge separation occurring in the TL model, one important specificity is that it can be derived from *both* fermionic and bosonic operators. Remarkably, the kinetic term $\mathcal{H}_4$ of the Hamiltonian yields the exact same energy spectrum for both operators [24]. In the interacting case including $\mathcal{H}_2$ and $\mathcal{H}_4$, the bosonic representation of the Hamiltonian in Eq. (2.15) is more concise whereas the fermionic operators are handier to compute the correlation functions [14]. However, the low-energy excitations can be described in terms of either operators [15].

---

[12] This would typically be indicated by a sub or superscript σ and ρ respectively. For simplicity, this notation will not be used in the remainder of this thesis.

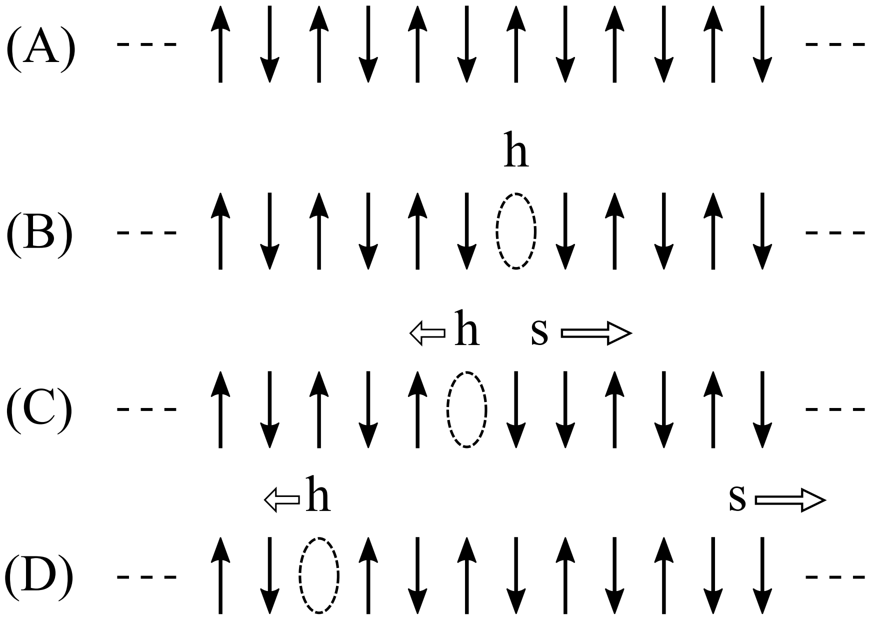

Figure 2–9: **(A)** A one-dimensional anti-ferromagnetic spin chain (typically a 1D Hubbard model with strong coupling and half-filling of the sites, *i.e.* each site contains only one spin). **(B)** A spin is removed from a site creating a *holon* surrounded by two aligned spins. **(C)** The holon is moved to the left thanks to the kinetic term of the Hamiltonian. It is now surrounded by anti-aligned spins and creates a *spinon*, a pair of adjacent aligned spins. **(D)** If the Hamiltonian contains spin exchange processes, the spinon can move along the chain with a velocity not necessarily equal to the holon's, as illustrated in the figure. *Based on* Fig. 3–4 in Ref. [16].

This correspondence between boson and fermion systems is a unique characteristic of one-dimensional system, a property that was actually already highlighted before the TL model [30].

The physics of a one-dimensional system is exemplified by determining single particle (spectral) or density-density correlation functions. The single-electron spectral function $A(q, \omega)$[13] in the TL model is shown together with the spectral functions

---

[13] The spectral function is a count of the excited states with energy ω that can be created by the addition of an electron with momentum q to the system.

of the Fermi gas and FL in Fig. 2–10 The spectral function of the TL model displays power law decay with non-universal[14] exponents greatly differing from FL theory. A very important result from the TL model is that these power law exponents are <u>all</u> controlled by the Luttinger parameter K.

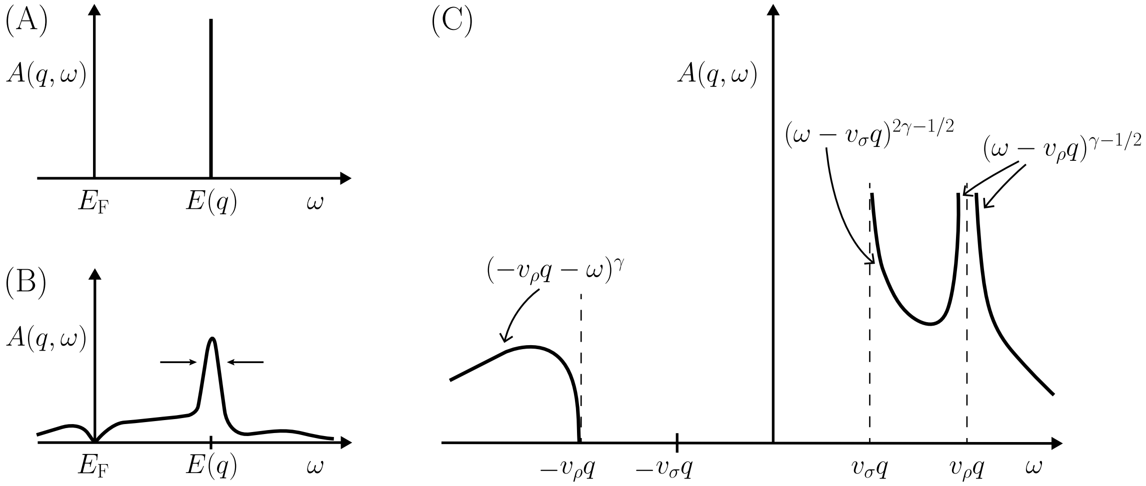

Figure 2–10: Spectral function $A(q,\omega) = \sum_f \left|\langle f|c_q^\dagger|0\rangle\right|^2 \delta(E_f - E_0 - \omega)$ where f labels the excited states above the ground state $|0\rangle$. All figures are at $T = 0$. **(A)** The spectral function of a free fermion is a Dirac delta function at the frequency $\omega = E(q)$. **(B)** The spectral function of a Fermi liquid is a peak broader than a Dirac delta function, exhibiting quasi-particle excitations at energy $E(q)$ and momentum q (the width is inversely proportional to the lifetime of the quasi-particle). **(C)** The spectral function in the TL model with $g_2 \neq 0$ and $g_4 \neq 0$. One can clearly see the two peaks rising on the $\omega > 0$ quadrant. They correspond to spin and charge excitations and are located at $\omega = v_\sigma q$ and $\omega = v_\rho q$. The behavior in the vicinity of these peaks follows power laws dictated by non-universal exponents that are functions of K, $\gamma = \frac{1}{8}(K + K^{-1} - 2)$. *Based on* [14, 31].

---

[14] *i.e.* because they depend on the microscopic details of the system, they do not belong to a universality class.

The TL model introduced in this section is exactly solvable, but it has limitations [27]. Those are inherent to the linear approximation of the energy distribution at the Fermi points and the omission of scattering processes ($\mathcal{H}_1$ and $\mathcal{H}_3$). The linearization prevents a description including cross-scattering of excitations themselves. For example, the process $\mathcal{H}_1$ accounts for backscattering of particles by impurities and is likely present in experimental systems. The Umklapp processes, described by $\mathcal{H}_3$, play a role for large momentum excitations ($q \simeq 4k_\mathrm{F}$) only. In the next section, we will focus on the generalization of the one-dimensional model beyond the linear approximation near the Fermi surface.

2.3.3 Generalization to the Tomonaga–Luttinger liquid model

Intuitively, one may fear that a more realistic model including backscattering and a non-linear energy dispersion close to the Fermi surface would not be solvable. Haldane showed that, at low-energy, the TL structure was preserved even for a model with a non-linear energy distribution near the Fermi surface [24]. This being said, Haldane argued that such a model is indeed similar to a TL model with added interactions between its low-energy excitations. The fundamental relations in Eq. (2.18) between the velocities associated with the spin and charge excitations, and the Luttinger parameters K and v_S were shown by him to still hold. In the non-linear regime, the values of K and v_S are simply renormalized by the interactions between the excitations. Haldane called this model the *Tomonaga–Luttinger liquid* (TLL) model in analogy to the Fermi liquid which is a solvable model of the Fermi gas in the presence of strong interactions. In general, in the limit $q \to 0$ and $\omega \to 0$, a one-dimensional many-body system of correlated particles featuring a branch of gapless excitations will accurately be described by a renormalized TL model [14].

Haldane's conjecture is quite powerful as it implies that one only needs the knowledge of K and v_S at low-energy and to renormalize them in the case of higher energies excitations. In principle, the parameters K and v_S could be determined experimentally either from spin susceptibility, specific heat or compressibility[15] since these quantities are simply renormalized by the interactions. In the case of ^{4}He flow though a nanopore, K could be determined from the non-universal exponents of mass flow power laws dependences on pressure ($Q_{m,1D} \sim \Delta P^{\beta}$) and temperature ($Q_{m,1D} \sim T^{\gamma}$). Another possible route would be to directly probe the correlation functions and extract K from fits, as is done in a QMC simulation [28].

---

[15] *i.e.* the rate of change of density with respect to the chemical potential.

2.4 Phase transitions in liquid ^{4}He

In order to probe TLL behavior in a real and tangible liquid, helium appears to be the only suitable candidate. Indeed, all other elements freeze at the temperatures required for an experimental realization of a TLL, which is on the order of the hundreds of mK. In contrast, helium does not solidify at atmospheric pressure due to the zero-point motion of its constituent atoms. Moreover, below a critical transition temperature, both isotopes ^{3}He and ^{4}He undergo a phase transition from a normal fluid phase into a quantum ordered phase called a *superfluid*. The hallmark of this quantum phase is a vanishing viscosity, thereby enabling frictionless flow. This property is a valuable asset for measuring flows in increasingly confined geometries, and towards the one-dimensional limit. In addition, experiments in helium could also be realized with either ^{4}He or ^{3}He which follow bosonic and fermionic statistics, respectively. This could be important to demonstrate the indistinguishability of bosons and fermions in one-dimensional systems.

The critical superfluid transition temperature of ^{4}He, $T_\lambda = 2.17$ K at saturated vapor pressure (SVP), is much larger than that of ^{3}He, $T_{c,^3\mathrm{He}} = 2.7$ mK. It justifies our initial focus on the bosonic species. The extraordinarily high price of ^{3}He, rising to several thousands of US dollars for a liter of gas, is also another motivation to first use ^{4}He as a benchmark for flow experiments in confined geometries. In the following subsections, the main characteristics of the superfluid phase of ^{4}He will be introduced, and its relevant flow properties described in details. A special focus will be made on the dissipation mechanisms occuring in a superfluid.

2.4.1 Superfluidity

The liquid phase of ^{4}He at SVP was first observed on July 10th 1908 by Kamerlingh–Onnes and co-workers in Leiden. On that day, they also crossed the transition temperature to the superfluid phase but did not notice the difference with the normal liquid phase [32, 33]. The transition to the superfluid phase was reproduced twenty years later in the same laboratory by Keesom and Wolfke[16]. They proposed the names Helium I and Helium II for the liquids above and below the transition temperature, respectively [34]. The phase diagram of ^{4}He is shown in Fig. 2–11.

In 1932, Keesom and Clusius measured the specific heat of liquid ^{4}He and observed that it displays a discontinuity at the transition temperature in the shape of the greek letter λ [36]. They named it the "λ transition". In 1938, the ability of Helium II to flow without apparent viscosity was discovered conjointly by Kapitza [37] and Allen and Misener [38].

The first theoretical models of ^{4}He superfluidity were developed by London, Tisza and Landau shortly after its experimental discovery. London proposed to describe superfluidity as a Bose–Einstein Condensate (BEC), whereas Landau and Tisza independently proposed a model based on the hydrodynamic properties of superfluid helium, the well known *two-fluid model* [39–42]. The two approaches were first perceived as contradictory but eventually were reconciled by Bogolyubov's theory of weakly interacting Bose gas and in the Feynman path integral formulation [43, 44]. Anderson, building on the works of Feynman, Onsager and Penrose firmly established the concept of macroscopic wave function with a well-defined coherent

---

[16] They mention that Kamerlingh–Onnes had already noticed a strange behavior in the liquid density near 2.17 K, *i.e.* near T_λ.

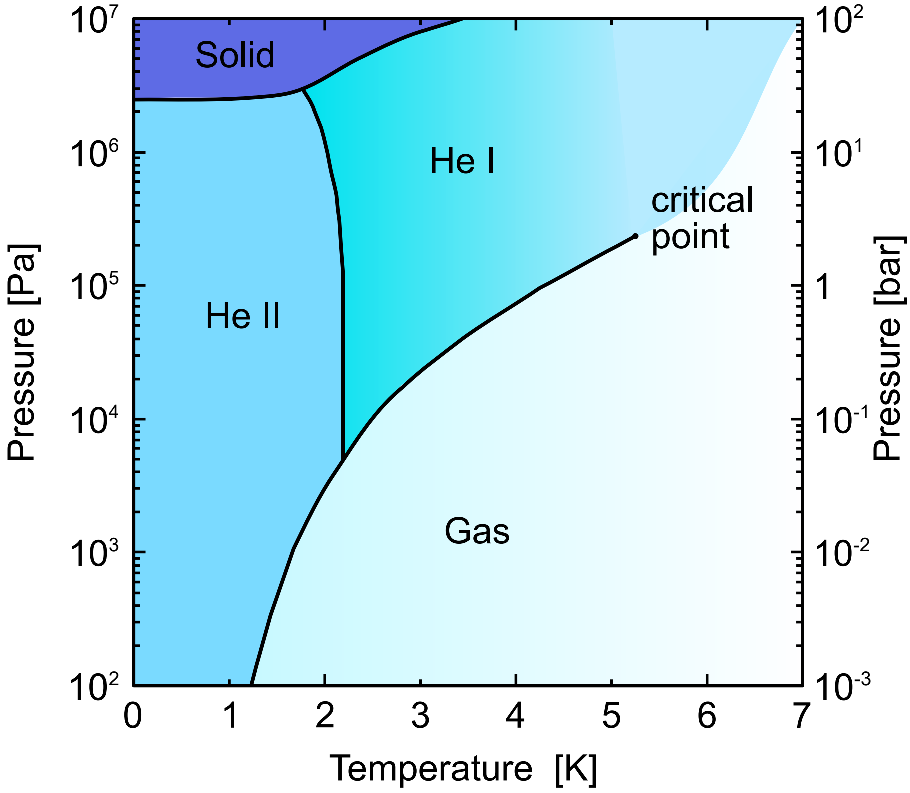

Figure 2–11: Pressure-temperature phase diagram of bulk ^{4}He. The transition between the liquid phase (He I) and the superfluid phase (He II) occurs at T_λ near 2.17 K at SVP. A unique property of ^{4}He is the absence of a solid phase at pressures below ~ 25 atm. *Based on* [35].

phase. This formalism successfully describes the superfluid phase and the evolution of its macroscopic quantities [44–47].

The ^{4}He superfluid is thus characterized by a macroscopic complex wave function $\Psi(r,t)$, dependent on position r and time t. This wave function is a coarse grained average of the single particle field operator $\psi(r,t)$ over small elements of volume containing nevertheless a macroscopic number of particles [46]

$$\langle \psi(r,t) \rangle = \Psi(r,t) = \Psi_0(r,t) e^{i\Phi(r,t)}, \tag{2.21}$$

where $\Phi(r,t)$ is the coherent phase and the amplitude $\Psi_0(r,t)$ is related to the superfluid fraction of the total density ρ and the mass of an ^{4}He atom m_4 through $\Psi_0^\dagger(r,t)\Psi_0(r,t) = \rho_s/m_4$. In the bulk of a superfluid, it is assumed that both $\Psi_0(r,t)$ and $\Phi(r,t)$ are slowly varying in space without sharp discontinuities[17], *i.e.* the strong correlations between bosons in a dense system as well as the amplitude and phase fluctuations due to atomic motions are smoothed out by the coarse grained average [47]. The order parameters at the superfluid phase transition are the superfluid density ρ_s, and the phase Φ. The symmetry which is broken[18] below the transition temperature is the choice of the phase Φ.

Anderson has shown that the number of particles N and the phase Φ of the superfluid obey to canonical relations analogous to the position and momentum of a single particle [46]. The commutation relation of Φ with the Hamiltonian of the system $\mathcal{H}$ yields an equation of motion for the phase,

$$\hbar\frac{\partial\Phi}{\partial t} = [\mathcal{H},\Phi] = -\frac{\partial\mathcal{H}}{\partial N}. \tag{2.22}$$

Upon taking the mean value of Eq. (2.22), $\mathcal{H}$ becomes equal to the energy E of the superfluid and $\frac{\partial E}{\partial N}$ can be identified as the chemical potential μ,

$$\hbar\frac{\partial\Phi}{\partial t} = -\mu. \tag{2.23}$$

---

[17] In the remainder of the thesis, the explicit position and time dependence of $\Phi(r,t)$ will be dropped.

[18] For historical reasons, it is referred to as “broken gauge symmetry” although it is related to the phase [47].

This relation is extremely important as it links the quantum mechanical phase of a superfluid to its macroscopic properties. According to Eq. (2.23), when there exists a chemical potential difference across two parts of a superfluid, their respective phase difference must vary in time. This can be interpreted as an acceleration of the superfluid component by taking the gradient on both sides of Eq. (2.23),

$$\frac{\partial(\hbar\vec{\nabla}\Phi)}{\partial t} = -\vec{\nabla}\mu = \vec{F}, \tag{2.24}$$

where $\vec{F}$ is a force acting on the particles of the superfluid. Eq. (2.24) is similar to Euler's equation for inviscid flow, where $\hbar\vec{\nabla}\Phi$ here corresponds to a momentum. It states that the superfluid may flow without friction by way of a chemical potential difference[19]. The velocity of the superfluid particles is then simply defined as

$$\vec{v}_s = \frac{\hbar}{m_4}\vec{\nabla}\Phi. \tag{2.25}$$

We shall come back to Eq. (2.25) in section 2.4.3 when considering dissipations in superfluid flow.

Landau and Tisza assumed that below the superfluid transition temperature T_λ, the Helium II phase consists of normal and superfluid components, independent from each other and with distinct physical properties [40, 41]. Mathematically, this is expressed as

$$\rho = \rho_n + \rho_s, \tag{2.26}$$

---

[19] For example, the chemical potential difference can arise from a pressure or temperature difference across the superfluid, or a combination of both.

where ρ stands for the total density. The superfluid component ρ_s carries no entropy and is inviscid, whereas the normal component ρ_n solely carries the viscosity and entropy. The temperature dependence for the two densities is shown in Fig. 2–12.

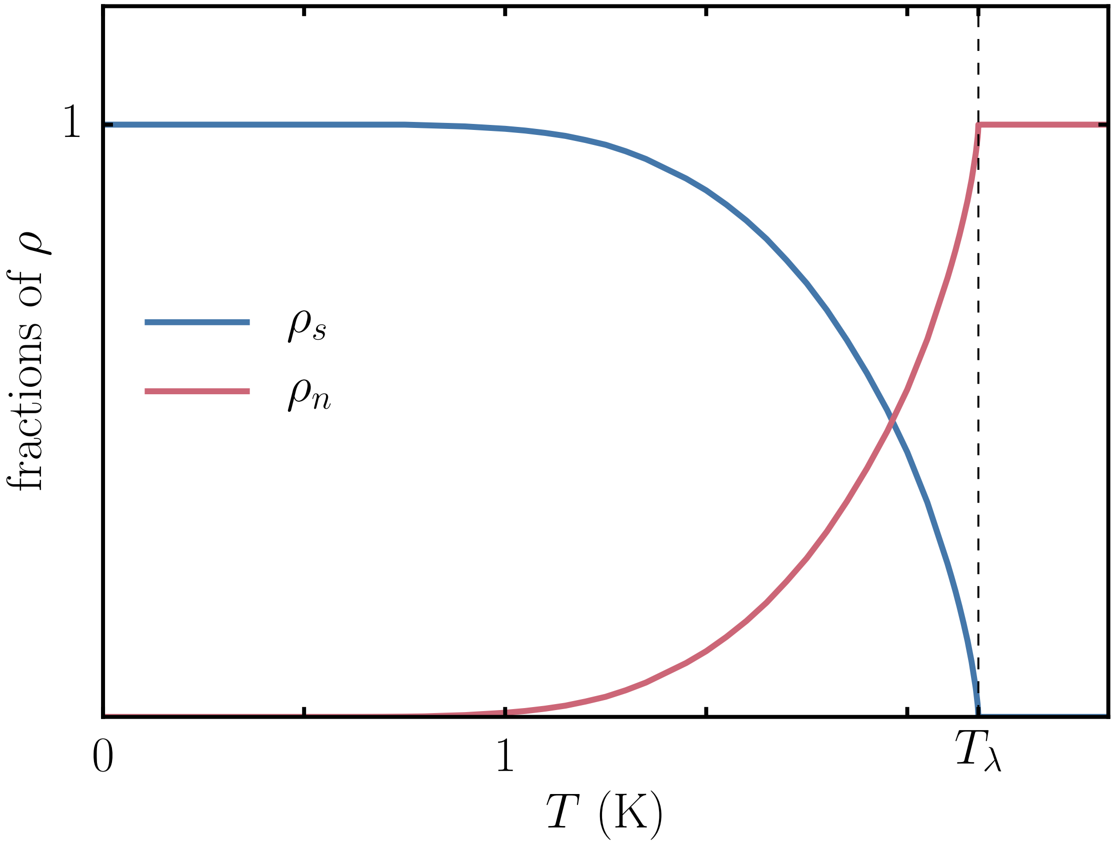

Figure 2–12: Illustration of the two-fluid model densities. As temperature decreases below T_λ, the superfluid part of Helium II, ρ_s, becomes more and more dominant over the normal part, ρ_n, due to the decrease in numbers of thermal excitations (*cf.* section 2.4.2). Below 1 K, liquid ^{4}He consists for the most part of the Helium II phase and $\rho = \rho_s$. Close to T_λ, the superfluid density scales as $(1 - \frac{T}{T_\lambda})^{-\nu}$, with $\nu \simeq 0.67$ [48]. *Data source*: [49].

Straightforward connexion of the superfluid density ρ_s to the BEC aspect of the superfluidity, *i.e.* the number of atoms forming the condensate, is tempting at first but inaccurate. Neutron scattering experiments could directly measure the fraction of atoms inside the BEC and it was found to be far from unity [50, 51]. This fraction was first estimated theoretically to 8% by Penrose and Onsager [45]. However, later experiments found values closer to 10% [51]. The fraction of atoms in the condensate is therefore not equal to the fraction of the superfluid density ρ_s/ρ. Rather, the superfluid density "stands for the inertia of the superfluid fraction" [47]. It consists of atoms in the condensate as well as atoms excited out of the condensate by interatomic interactions[20] [52]. Oscillating disc experiments have been used to define ρ_s, as they are sensitive to the inertial decoupling of the superfluid part [53]. Finally, when the fluid is set into laminar motion, its normal part moves independently from its superfluid part and the total current density $\vec{J}_{\text{tot}}$ is given by

$$\vec{J}_{\text{tot}} = \vec{J}_n + \vec{J}_s = \rho_n \vec{v}_n + \rho_s \vec{v}_s, \tag{2.27}$$

where $\vec{v}_n$ obeys the Navier-Stokes equation for viscous flow and $\vec{v}_s$ is described by Eq. (2.25).

2.4.2 Superfluid elementary excitations

At low temperatures, thermal excitations above the superfluid ground state are scarce and can be modeled as a non-interacting gas of quasi-particles. The energy dispersion relation for the excitations of ^{4}He, measured by neutron scattering is illustrated in Fig. 2–13. As can be seen on the figure, there are two types of excitations:

---

[20] In the BEC picture, the normal fluid consists of thermal excitations above the ground state [52].

phonons and rotons. Below 0.8 K, phonons are the dominant excitations whereas rotons dominate above that temperature [48]. The two-fluid model is solely based on phonons and rotons as possible dissipations from the superfluid state. Section 2.4.3 will introduce other dissipation mechanisms which occur when the superfluid is set into motion.

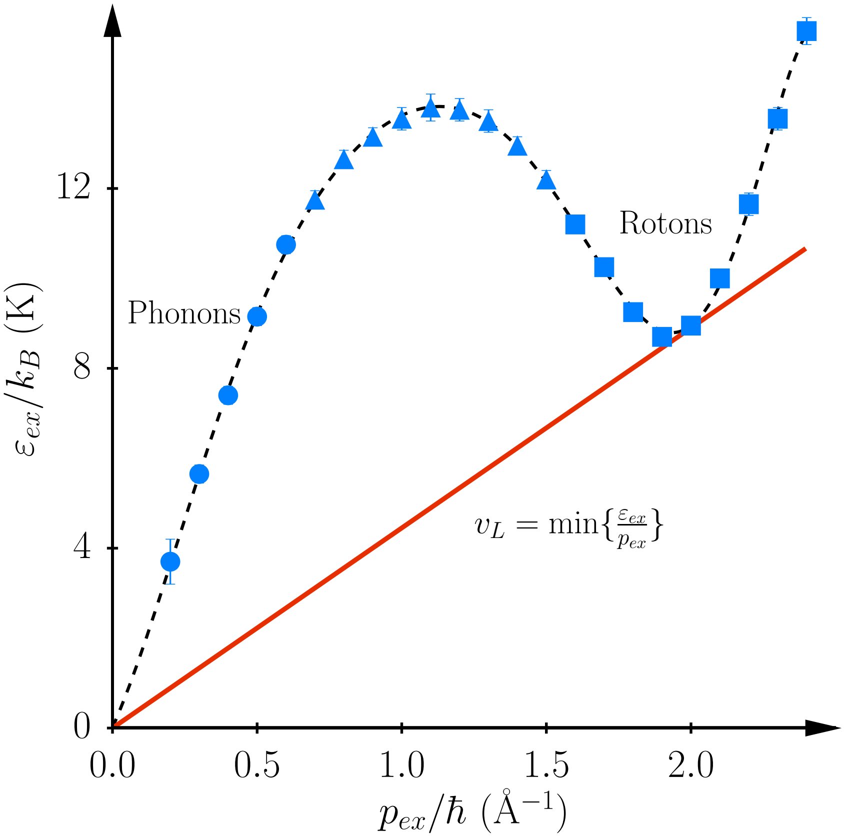

Figure 2–13: Energy dispersion relation for excitations in ^{4}He. The data originates from neutron scattering experiments at 1.1 K and SVP. There are two main branches. The phonon branch (circles), where the wavelength associated with the momentum is large compared to the interatomic distances (small momenta), features a linear dispersion relation. The roton branch (squares) is located to the local minimum of the dispersion relation, corresponding to wavelengths comparable with the interatomic distances [48]. The orange slope correspond to the Landau critical velocity of 58 m/s and the dashed line is a 8th degree polynomial fit of the data. *Data source*: [54].

2.4.3 Dissipation mechanisms in superfluid flow

2.4.3.1 Landau critical velocity

The velocity at which superfluid ^{4}He can flow has an upper bound, for which the flow can no longer be accelerated. Above a certain velocity, any additional energy will lead to the creation of an excitation, flagging onset of dissipation. Within the two-fluid model, Landau has determined this velocity by invoking energy and momentum conservation. The creation of an excitation reduces the kinetic energy of a superfluid with mass M initially flowing at a velocity v_s. Therefore, the energy of the excitation is equal to

$$\varepsilon_{ex} = \frac{1}{2}M(v_s^2 - v_s'^2) = \frac{1}{2}M(v_s - v_s')(v_s + v_s') \simeq M(v_s - v_s')v_s, \tag{2.28}$$

where v_s' is the velocity after the excitation is created. The last step is possible if one assumes that the energy of a single excitation is very small compared to the kinetic energy of the superfluid, *i.e.* $\varepsilon_{ex} \ll \frac{1}{2}Mv_s^2$. The momentum conservation dictates that

$$Mv_s = p_{ex} + Mv_s', \tag{2.29}$$

and so, combining Eqs. (2.28) and (2.29) yields

$$v_s = \frac{\varepsilon_{ex}}{p_{ex}}. \tag{2.30}$$

Therefore, the minimum critical velocity v_c that the superfluid must reach before creating an excitation is given by

$$v_c = \min\{\frac{\varepsilon_{ex}}{p_{ex}}\}, \tag{2.31}$$

and within the two-fluid model, this velocity is called the *Landau critical velocity*. It corresponds to the largest slope that can be sketched on the energy dispersion relation shown in Fig. 2–13 before meeting the spectrum. This slope stretches from the origin to the roton minimum, yielding a numerical value of $v_c = v_{c,L} = 58$ m/s.

However, years of experiments have shown that superfluid ^{4}He exhibits a critical velocity well below $v_{c,L}$ [55]. When Landau had calculated this velocity, he had considered that phonons and rotons are the lowest energy excitations available for dissipation in the flow. Since then, vortices were discovered as better candidates for dissipation mechanisms [56]. Nevertheless, Landau's approach to determine the critical velocity of the superfluid remains valid at the conceptual level and can equally be applied to vortices. We shall now introduce the rotation of Helium II and vortices as well as the critical velocity associated to their creation.

2.4.3.2 Vortices in ^{4}He superfluid

An important result from oscillating discs experiments in Helium II is that the superfluid part cannot be set into rotation by the drag of the disc [57]. This property is predicted by the definition of the velocity's potential in Eq. (2.25):

$$\vec{\nabla} \times \vec{v}_s = \vec{\nabla} \times \vec{\nabla}\Phi \equiv \vec{0}. \tag{2.32}$$

This expression states that the superfluid part of Helium II is irrotational. A mathematical equivalent to Eq. (2.32) can be found by applying Stokes' theorem to the circulation κ of v_s along a closed contour ∂A inside the superfluid part,

$$\kappa \equiv \oint_{\partial A} \vec{v}_s \cdot \mathrm{d}\vec{l} = \iint_A \vec{\nabla} \times \vec{v}_s \cdot \mathrm{d}\vec{a} = 0, \tag{2.33}$$

where A is a surface spanning the contour ∂A. From Eq. (2.33) we see that the circulation of the superfluid velocity v_s along a closed loop should always remain zero. This property has been challenged by experiments consisting of a rotating bucket filled with liquid ^{4}He. At large rotation speeds Ω, the same meniscus was visible at the top surface of both Helium I and Helium II [58, 59]. Additional experiments showed that the superfluid part in the Helium II was still present[21] despite the meniscus. Furthermore, the rotation velocity was too small to consider effects from Landau's critical velocity. This meant that the circulation along a circle of radius almost equal to the bucket's radius R_b and concentric with the bucket's axis had to be close to $2\pi R_b^2 \Omega$ in both cases. As this quantity is non-zero, the expression in Eq. (2.33) was thus directly contradicted by experiments.

Theory and experiment could nevertheless be reconciled. The fact that the superfluid phase is still present in rotating Helium II means that the macroscopic wave function $\Psi(r,t)$ should remain non zero and single valued [44, 46]. However, the phase Φ can change by $2\pi n$, with $n \in \mathbb{Z}$, without affecting the wave function. Combining this observation with Eq. (2.25) and Eq. (2.33) yields

$$\kappa = \oint \vec{v}_s \cdot \mathrm{d}\vec{l} = \frac{\hbar}{m_4} \oint \vec{\nabla}\Phi \cdot \mathrm{d}\vec{l} = \frac{\hbar}{m_4}\Delta\Phi = \pm\frac{2\pi\hbar}{m_4}n = \pm n\kappa_0, \tag{2.34}$$

where $\kappa_0 = h/m_4$ is the quantum of circulation. Thus, the circulation around a closed loop inside the superfluid is not necessarily zero and Eq. (2.34) states that quantized excitations exist inside rotating Helium II. Physically, this can be interpreted as portions of Helium II leaving the superfluid state and acquiring a circulation while being surrounded by a superfluid at rest. These portions are called *line vortices* and are defined by a velocity field v_v in the following way,

$$\kappa = \oint \vec{v}_v \cdot \mathrm{d}\vec{l} = 2\pi r v_v. \tag{2.35}$$

---

[21] This was done by observing the “fountain effect”, the ability of superfluid to flow through tiny pores [58].

For the sake of simplicity, the circulation is taken here along a circle around a straight line vortex. Therefore,

$$v_v(r) = \frac{\kappa}{2\pi r} \sim \frac{1}{r}. \tag{2.36}$$

and it guarantees that v_v vanishes away from the line vortex, consistent with the irrotationality of the superfluid. For v_v to not become infinite, the expression in Eq. (2.36) becomes invalid below some distance a_0, comparable with interatomic length scales. The core of the line vortex is assumed to be close to a_0, which is on the order of a few tenths of nanometers [56]. The line vortex stretches until the boundaries of the superfluid, *i.e.* the walls or the surface of Helium II. In the case of a linear flow, the ends of the vortex can connect together, thereby forming a ring vortex which axis is parallel to the flow. Alternatively, a line vortex can also form in a channel flow. In such a case, its ends are pinned to the walls of the channel. Schematic representations of a line vortex and a ring vortex inside a cylindrical channel are displayed in Fig. 2–14.

It can be shown that a vortex which possesses n quanta of circulation κ_0 is thermodynamically unstable and will likely separate into n vortices carrying a single quantum of circulation each [48, 53]. This is important to explain the appearance of a meniscus in rotating Helium II bucket experiment [56]. If the circulation would consist only of a few vortices carrying many quantum of circulation, then the tangential velocity as a function of the radial distance from the center of the bucket would experience abrupt discontinuous jumps. In the case of Helium I, the tangential velocity of the liquid obeys the linear relation relation $v(r) = \Omega r$. Therefore, the solution to approach this linear relation as closely as possible is to increase the

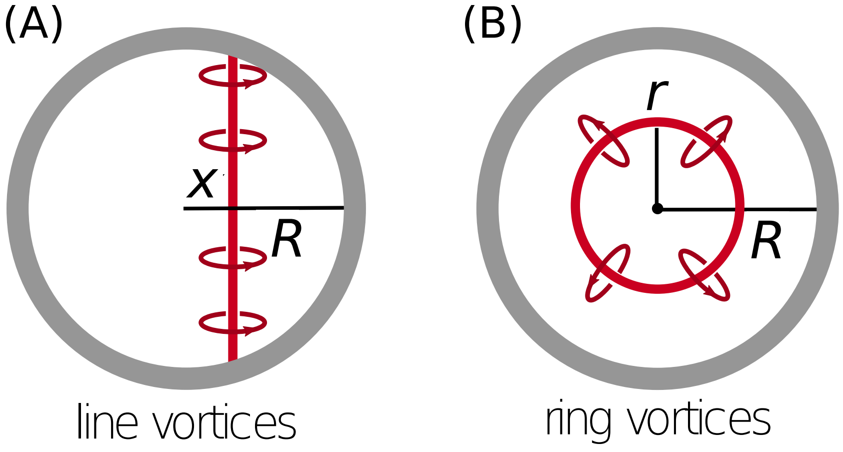

Figure 2–14: Two vortex types that can be nucleated in a cylindrical channel of radius R by a superfluid flow. The flow is coming out of the page. **(A)** A line vortex located a distance x from the center of the channel. The line vortex begins and ends on the boundaries of the channel. **(B)** A ring vortex of radius r centered around the axis of the channel. The direction of the circulation is indicated around the cores of the vortices. *Source*: [60].

number of quantized vortices. In order to do so without changing the total circulation within the bucket, the solution is to break the vortices into a large number of vortices carrying one quantum of circulation κ_0.

2.4.3.3 Feynman critical velocity

Because the core of the vortex is not constituted of superfluid, the order parameter (*i.e.* ρ_s) has to vanish there. This means that the vortices cores are nodes of the macroscopic wave function and this is another hint that some kind of excitation exists [56]. Although there is now a consensus that vortices are elementary excitations of superfluid helium, the exact microscopic dynamics which govern the nucleation of these topological defects remains an open problem in condensed matter physics. The Landau criterion for the maximal velocity at which the superfluid can flow before nucleating vortices in Eq. (2.31) is still valid. This new critical velocity was computed by Feynman in the case of ring vortex of radius r,

$$v_{c,F} \simeq \frac{\kappa_0}{4\pi r} \ln \frac{2r}{a_0}, \tag{2.37}$$

and it is valid as long as $r \gg a_0$. If a superflow is to take place within a restricted geometry, such as a cylindrical channel of radius R, the largest ring vortices that can be created in the channel will have a size limited by the channel's radius, $R = \max(r)$. Thus, the critical velocity will be scaling as $\ln(2R)/2R$, *i.e.* it should increase as the channel gets smaller as illustrated in Fig. 2–15.

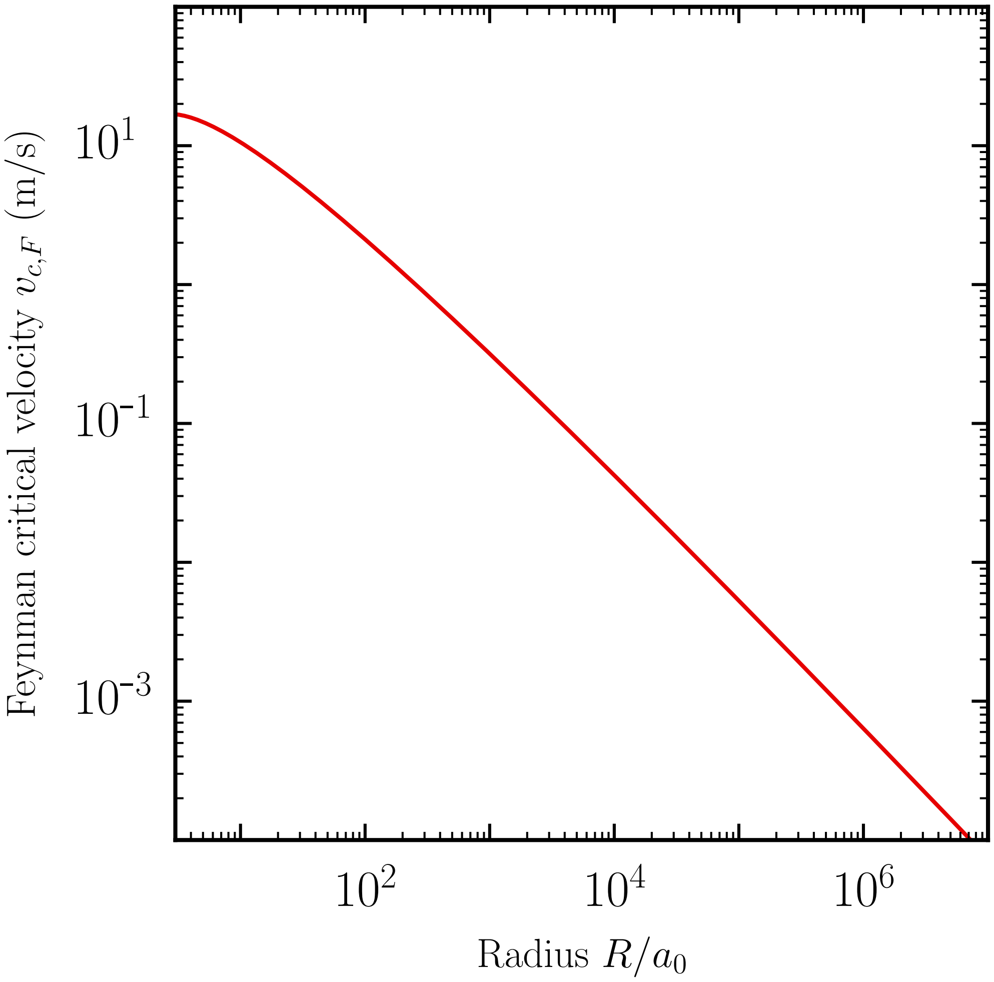

Figure 2–15: Feynman critical velocity from Eq. (2.37) with $a_0 = 0.345$ nm.

In chapter 4, we will return to this topic as the experimental results presented in this thesis will be compared with Feynman's theoretical prediction Eq. (2.37) for the critical velocity. Newer theoretical predictions for the critical velocities in channel and orifice flows, as well as phase slippage dissipation mechanisms, will also be discussed [60].

References

[1] Fisher, M. E. *Rep. Prog. Phys.* **30**, 615 (1967).

[2] Uzunov, D. I. *Introduction to the Theory of Critical Phenomena* (World Scientific, 1993).

[3] Ahlers, G. *Rev. Mod. Phys.* **52**, 489–503 (1980).

[4] Stanley, H. E. *Introduction to Phase Transitions and Critical Phenomena* (Oxford University Press, London, 1971).

[5] Mermin, N. D. & Wagner, H. *Phys. Rev. Lett.* **17**, 1133–1136 (1966).

[6] Stanley, H. E. *Rev. Mod. Phys.* **71**, S358–S366 (1999).

[7] Fisher, M. E. *Rev. Mod. Phys.* **70**, 653–681 (1998).

[8] Fisher, M. E. *Rev. Mod. Phys.* **46**, 597–616 (1974).

[9] Landau, L. D. *Zh. Eksp. Teor. Fiz.* **3**, 1058–1064 (1957).

[10] Wigner, E. *Phys. Rev.* **46**, 1002–1011 (1934).

[11] Peierls, R. E. *Ann. Phys.* **396**, 121–148 (1930).

[12] Moriya, T. *J. Magn. Magn. Mater.* **100**, 261–271 (1991).

[13] Ashcroft, N. W. & Mermin, N. D. *Solid state physics* (New York, 1976).

[14] Voit, J. *Rep. Prog. Phys.* **58**, 977–1116 (1995).

[15] Varma, C., Nussinov, Z. & van Saarloos, W. *Phys. Rep.* **361**, 267–417 (2002).

[16] Giamarchi, T. *Quantum Physics in One Dimension* (Oxford University press, 2004).

[17] Engelbrecht, J. R. & Randeria, M. *Phys. Rev. Lett.* **65**, 1032–1035 (1990).

[18] Anderson, P. W. *Phys. Rev. Lett.* **64**, 1839–1841 (1990).

[19] Anderson, P. W. & Ren, Y. *Ann. N. Y. Acad. Sci.* **581**, 44–65 (1990).

[20] Edwards, D. M. *J. Phys. Condens. Matter* **5**, 161 (1993).

[21] Luchini, M. U. & Edwards, D. M. *J. Low Temp. Phys.* **99**, 305–310 (1995).

[22] Benfatto, G., Giuliani, A. & Mastropietro, V. *Ann. Henri Poincaré* **7**, 809–898 (2006).

[23] Imambekov, A., Schmidt, T. L. & Glazman, L. I. *Rev. Mod. Phys.* **84**, 1253–1306 (2012).

[24] Haldane, F. D. M. *J. Phys. C: Solid State Phys.* **14**, 2585–2609 (1981).

[25] Tomonaga, S.-I. *Progr. Theor. Phys.* **5**, 544–569 (1950).

[26] Luttinger, J. M. *J. Math. Phys.* **4**, 1154–1162 (1963).

[27] Lieb, E. & Mattis, D. *J. of Math. Phys.* **6**, 304–312 (1965).

[28] Del Maestro, A., Boninsegni, M. & Affleck, I. *Phys. Rev. Lett.* **106**, 105303 (2011).

[29] Giamarchi, T. & Schulz, H. J. *Phys. Rev. B* **37**, 325–340 (1988).

[30] Girardeau, M. *J. Math. Phys* **1**, 516–523 (1960).

[31] Voit, J. *J. Phys. Condens. Matter* **5**, 8305 (1993).

[32] Kamerlingh Onnes, H. *Proc. Roy. Acad. Amsterdam* **11**, 168–185 (1908).

[33] van Delft, D. *Europhysics News* **39**, 23–25 (2008).

[34] Keesom, W. H. & Wolfke, M. *Proc. Roy. Acad. Amsterdam* **31**, 90–94 (1928).

[35] Savard, M. *Towards a One-Dimensional State of Neutral Matter.* Ph.D. thesis, McGill University (2014).

[36] Keesom, W. H. & Clusius, K. *Proc. Roy. Acad. Amsterdam* **35**, 307–320 (1932).

[37] Kapitza, P. *Nature* **141**, 74 (1938).

[38] Allen, J. F. & Misener, A. D. *Nature* **141**, 75 (1938).

[39] London, F. *Nature* **141**, 643 (1938).

[40] Landau, L. *Phys. Rev.* **60**, 356–358 (1941).

[41] Tisza, L. *J. Phys. Radium* **1**, 350–358 (1940).

[42] Balibar, S. *C. R. Phys.* **18**, 586–591 (2017).

[43] Bogolyubov, N. *J. Phys. U.S.S.R.* **11**, 23–32 (1947).

[44] Feynman, R. P. *Phys. Rev.* **94**, 262–277 (1954).

[45] Penrose, O. & Onsager, L. *Phys. Rev.* **104**, 576–584 (1956).

[46] Anderson, P. W. *Rev. Mod. Phys.* **38**, 298–310 (1966).

[47] Varoquaux, E. *Rev. Mod. Phys.* **87**, 803–854 (2015).

[48] Lifshitz, E. M. & Pitaevski, L. P. *Statistical Physics* (Butterworth-Heinemann, 1980).

[49] Donnelly, J. R. & Barenghi, C. F. *J. Phys. Chem. Ref. Data* **27**, 1217–1274 (1998).

[50] Fåk, B., Keller, T., Zhitomirsky, M. E. & Chernyshev, A. L. *Phys. Rev. Lett.* **109**, 155305 (2012).

[51] Azuah, R. T., Diallo, S. O., Adams, M. A., Kirichek, O. & Glyde, H. R. *Phys. Rev. B* **88**, 024510 (2013).

[52] Tilley, D. R. & Tilley, J. *Superfluidity and Superconductivity* (Institute of Physics Publishing, 1990), 3rd edn.

[53] Andronikashvili, E. L. & Mamaladze, Y. G. *Rev. Mod. Phys.* **38**, 567–625 (1966).

[54] Cowley, R. A. & Woods, A. D. B. *Can. J. Phys.* **49**, 177–200 (1971).

[55] Varoquaux, E. *C. R. Phys.* **7**, 1101–1120 (2006).

[56] Feynman, R. P. *Application of Quantum Mechanics to Liquid Helium - Chap. II* (Elsevier, 1955).

[57] Andronikashvili, E. L. *J. Phys. USSR* **10**, 201 (1946).

[58] Andronikashvili, E. L. & Kaverkin, I. P. *Zh. Eksp. Teor. Fiz.* **28**, 174–176 (1955).

[59] Hall, H. E. & Vinen, W. F. *Phil. Mag.* **46**, 546 (1955).

[60] Del Maestro, A. & Rosenow, B. *Phys. Rev. B* **95**, 140507 (2017).

CHAPTER 3

Materials and methods

In this chapter, we will introduce the experimental techniques used to acquire the data presented in chapter 4. We will first describe the two refrigerators used to cool down the nanopores below the ^{4}He superfluid transition temperature. The newer refrigerator will be described, although no data presented in this thesis were acquired with it. Nevertheless, future successors of this project may benefit from a description of this newer experimental setup. We will then present the nanopores' fabrication and mounting procedure within the experimental cell. Finally, we will discuss the measurement scheme and instrumentation of the flow experiments.

3.1 Cryogenics and thermometry

Reaching temperatures in the mK range is usually done in two main steps. The first step is to reach the temperature of liquid ^{4}He ($\simeq$4 K). A temperature of $\simeq$4 K is achieved either by means of a compressor and a Stirling cycle[1], which extracts the heat, or by providing a liquid ^{4}He bath. The two designs are referred to as *dry* and *wet*, respectively. A wet refrigerator requires weekly transfers of about 100 L of liquid ^{4}He, which becomes increasingly costly as the world's reserves of ^{4}He are getting scarcer [2]. Coupling the exhaust of a wet refrigerator to a liquefier is an efficient way to recycle the ^{4}He. A dry refrigerator takes longer to cool its inner components but does not require weekly liquid ^{4}He transfers after reaching the base temperature. The drawback is its consumption of large amounts of electrical power, thus making it sensitive to power shutdowns.

Once a temperature close to 4 K is achieved, there are few different routes to reach temperatures below 1 K. We will describe the two that are relevant to our refrigerators in the following sections.

The experimental setup used in previous works [3, 4] was mounted inside a Janis® ^{3}He wet refrigerator. The data presented in chapter 4 were also acquired using this experimental setup. However, the prospect of achieving stable temperatures down to a few mK motivated the design and construction of a second experimental setup on a BlueFors Cryogenics© dilution dry refrigerator. The two distinct experimental setups will be described in sections 3.1.1 and 3.1.2, respectively.

---

[1] called a *pulse tube* [1].

3.1.1 ^{3}He wet refrigerator

The ^{3}He wet refrigerator consists of two main parts: a *dewar*, which contains the liquid ^{4}He bath, and an *insert* enclosed in a *vacuum chamber*, which reaches the lowest temperatures. The insert, shown in Fig. 3–1, thermalizes towards 4 K thanks to ^{4}He gas inside the vacuum chamber which thermally connects it to the liquid ^{4}He bath. Once close to 20 K, the insert is thermally isolated from the ^{4}He bath by pumping the ^{4}He gas from the vacuum chamber. The insert reaches 4 K by filling the 1 K pot with liquid ^{4}He. Temperatures below 1 K are then obtained in two steps. The first step is to fill the 1 K pot with some liquid ^{4}He from the dewar's bath and pump on it with a utility pump to create evaporative cooling, thereby reaching temperatures on the order of 1.2 K. As soon as the temperature of the 1 K pot reaches below the ^{3}He liquefaction transition, $\simeq$3.2 K, the ^{3}He gas in the central tube shown in Fig. 3–1 will start to condense and drop into the ^{3}He pot. Once all available ^{3}He gas is liquefied, the second step consists in activating the charcoal sorption pump by cooling it using liquid ^{4}He from the dewar's bath. This will once again create evaporative cooling, and reach temperatures on the order of a few hundred mK. The ^{3}He pot is therefore the coldest part of this refrigerator, which is why the experimental cell was mounted on a coin silver[2] rod firmly attached to it. The lowest temperature can be maintained as long as liquid ^{3}He remains, which normally lasts between 2 and 4 days with this refrigerator. However, the capillary circuit carrying ^{4}He to our experimental cell created heat leaks and the lowest temperature could only be maintained for 5 to 6 hours (see section 3.1.1.3).

---

[2] Coin silver consists of 10% copper and 90 % silver and has high thermal conductivity at low temperature.

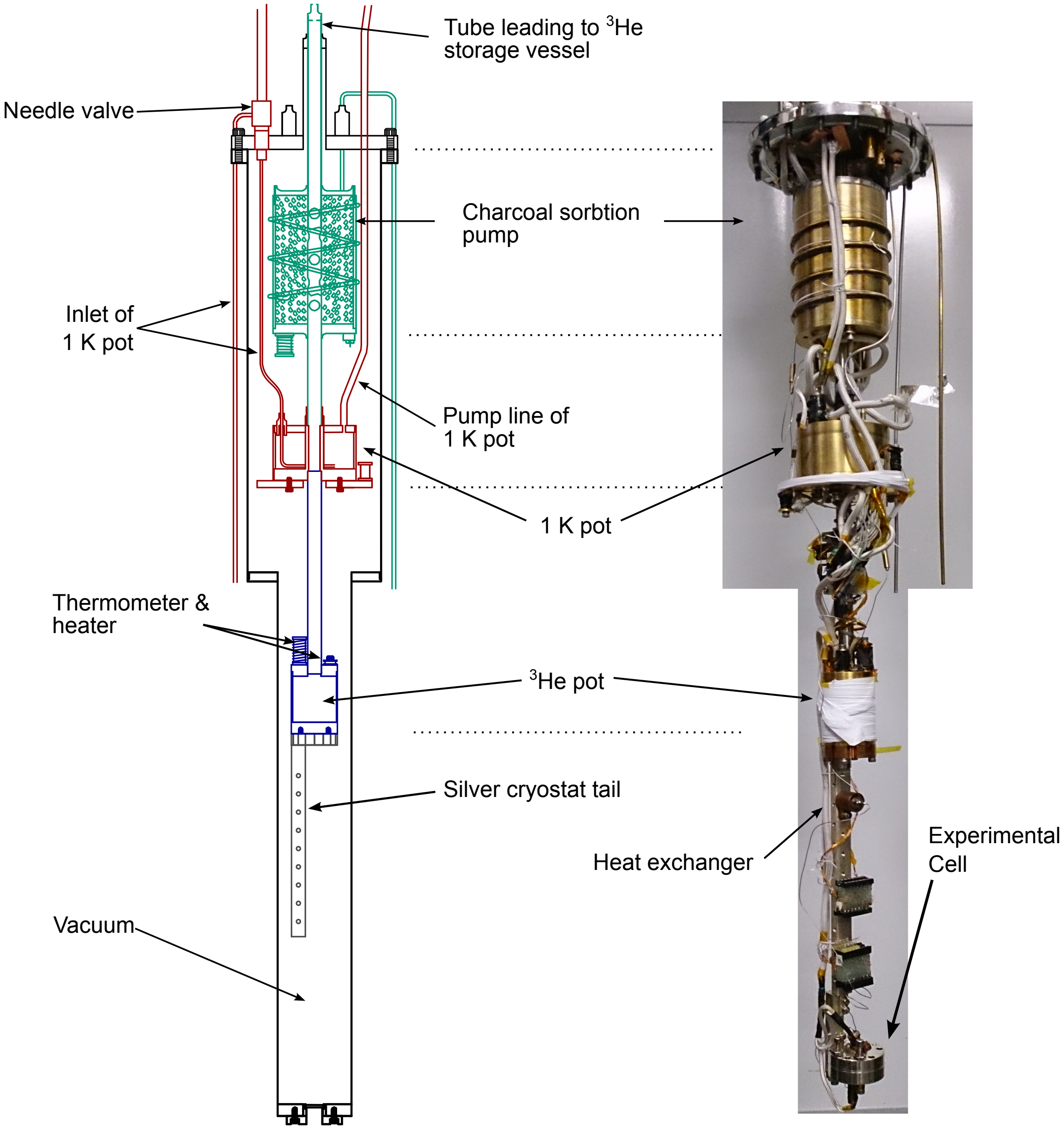

Figure 3–1: Diagram of the main ^{3}He refrigerator's insert components. On the right side is a photograph of the insert matching the schematics on the left. In black: the vacuum chamber immersed in the ^{4}He bath of the external dewar. In green: charcoal sorption pump parts. The central tube leads to a ^{3}He gas storage vessel on top of the external dewar (not visible). In blue: the central tube connects to the ^{3}He pot. In red: the liquid ^{4}He inlet to the 1 K pot from the ^{4}He bath, passing through the needle valve. In green: on the opposite side is a pumping line for evaporative cooling. In grey: silver tail, the coldest part of the insert and the volume dedicated for samples and the experimental cell. The diagram is a modified version of the drawings by the manufacturer, Janis Research Company, LLC. *Based on* [4].

3.1.1.1 Experimental cell

The experimental cell consists of two coin silver flanges, as illustrated in Fig. 3–2. The two flanges both bear a through-hole along their axis, serving as inlet (I) and outlet (O) for the ^{4}He. The cell can be closed hermetically with an o-ring (R) which is hand-crafted from a 1 mm diameter indium wire[3]. Brass screws (6-32) are used to firmly press and hold the two flanges tightly together. The through-hole of the bottom part of the cell on Fig. 3–2 is encircled by a groove in which another hand-crafted indium o-ring is used to seal the surrounding of the Silicon Nitride (Si_3N_4) membrane. The membrane is pressed against the o-ring (R) with an Invar® 42 (42% nickel) plate (P) and brass screws[4] (0-80). One side of these screws have been cut with a diamond saw to prevent air trapping at the bottom of the screws' pit. The inlet and outlet of the cell are connected to the experimental circuit by means of brass adapters. The capillaries used to transport the ^{4}He in and out of the cell are silver braised onto the brass adapters. The adapters then are firmly attached to the flanges of the cell with brass screws (2-56) and indium o-rings (R) are once more used for sealing.

3.1.1.2 Measurement and control of the temperature

A precise measurement of the temperature inside the cell is key. Indeed, a reliable control of the temperature cannot be achieved without it. The temperature is

---

[3] In the initial design, the seal was a copper ring against a knife-edge, but the larger thermal contraction of copper tended to open leaks at low temperatures.

[4] In the new design described in section 3.1.2, the 0-80 brass screws are replaced by stainless steel 316 ones. This is to avoid that the nickel contained in brass screws, due to its high SVP, constitutes a source of impurities when pumping on the cell.

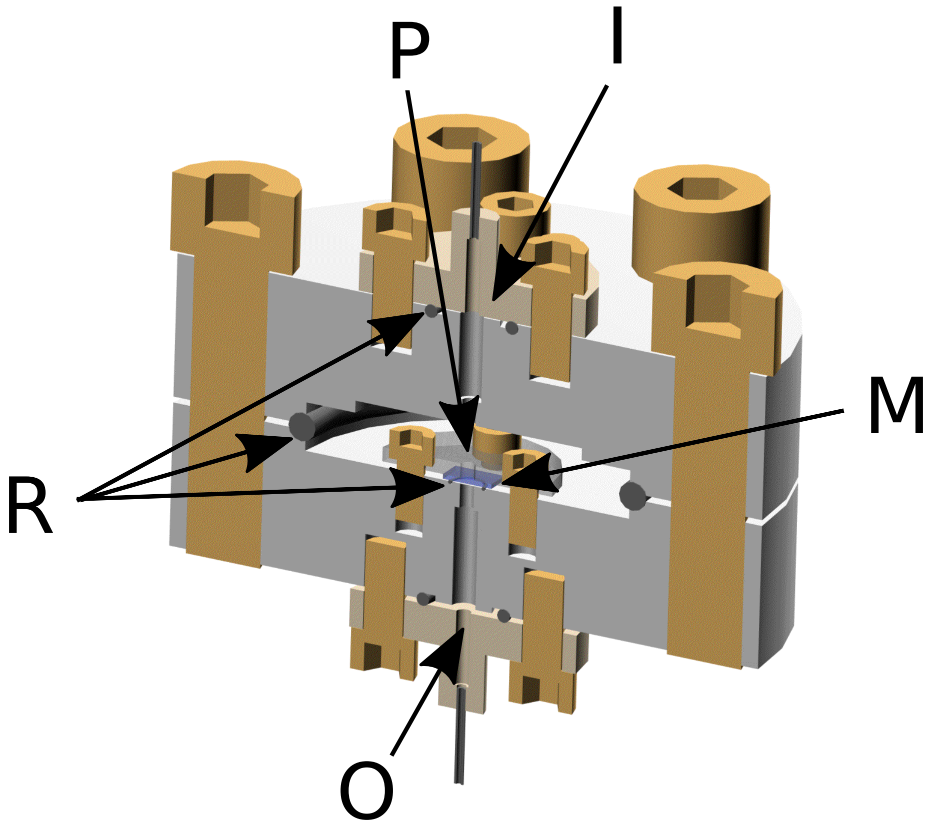

Figure 3–2: Computer-Aided design (CAD) drawing of the coin silver experimental cell which was mounted inside the ^{3}He refrigerator. The inlet/source (I) and outlet/drain (O) reservoirs are connected to the top and bottom parts of the cell, and sealed with indium o-rings (R). The silicon substrate, holding the Si_3N_4 membrane (M), is itself sealed to the bottom part of the cell with an indium o-ring (R) and a push-on Invar® plate (P). The initial design from Ref. [4] employed a copper o-ring to seal the bottom and top parts. However, due to the thermal expansion of copper compared to coin silver, the seal often did not work. An indium o-ring (R) was therefore used instead. The diameter of the flanges is 1-1/8 inch. The available volume of the main chamber (subtracting the volume of the screws and of the Invar® plate) is $\simeq$0.70 cm^3. *Art credits*: Richard Talbot.

regulated using Joule heating to warm the experimental cell above the base temperature provided by the refrigerator. A target temperature is reached by a PID loop which provides the adequate amount of current I to a resistive heater firmly screwed on the experimental cell. The heater thus brings a controlled heat load of power

$P_h = R_{heater} I^2$ to the experimental cell. The heater consists of a resistive 0.1 mm diameter manganin wire.

The thermometer used to monitor the temperature of the experimental cell is a Ruthenium oxide (RuOx) resistance chip. It was installed by Michel Savard [4]. The resistance chip was placed inside a copper bobbin, as shown in Fig. 3–3 and covered with Stycast® 2850. The leads connecting to the thermometer were tightly wound around the bobbin's shaft and glued in place with Stycast® 2850 to ensure their good thermalization. The bobbin was fixed onto the silver cell with a 4-40 stainless steel screw. The resistance of the thermometer was measured with a resistance bridge, a LakeShore® 340, in a 4-point measurement scheme to minimize the importance of the leads' resistance. The resistance of the thermometer was related to temperature using a Chebychev polynomial fitting on a National Institute of Standard and Technology (NIST) traceable calibration curve provided by LakeShore®.

3.1.1.3 Heat exchangers

When the refrigerator is cold, bringing ^{4}He to the experimental cell is not a straightforward task. This is because, at low temperature, superfluid ^{4}He is amongst the best thermal conductors[5] known to humankind. Hence, a capillary filled with it creates heat leakage to the experimental cell inside the refrigerator. This heat leakage eventually prevents the refrigerator to reach its lowest operating temperatures and often alters temperature stability. A look at Eq. (A.1) suggests that an efficient way to decrease heat leak is to reduce the cross section, and increase the length of the capillaries transporting ^{4}He to the experimental cell. Unfortunately, reducing the

---

[5] The thermal conductivity of superfluid ^{4}He at T_λ is one order of magnitude above that of silver's maximal thermal conductivity at $T = 10$ K [6].

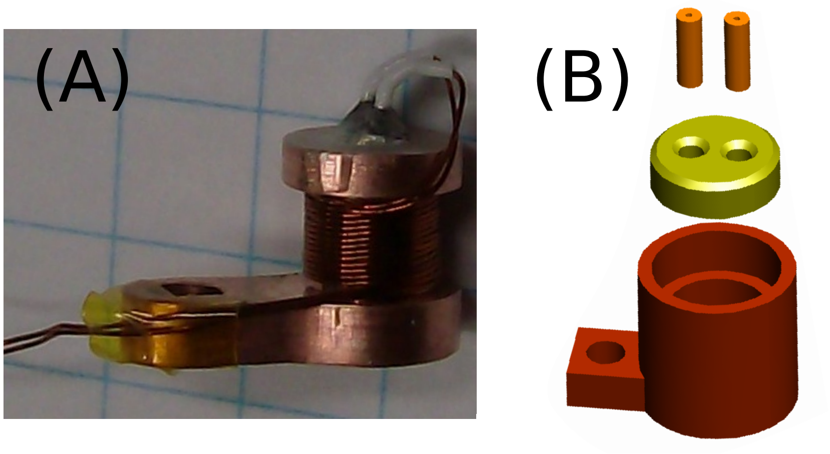

Figure 3–3: **(A)** Thermometer inside an Oxygen-free High Conductivity (OFHC) copper piece milled in a bobbin shape. The electrical leads can be wound around the post thereby ensuring that the whole unit is well thermalized. The RuOx resistive element is (hidden from view) inside the bobbin within a protective canister. **(B)** Exploded view of a heat exchanger where the bottom part is filled with pressure-sintered silver powder. The two posts are silver-brazed to the cap of the small container and capillaries are soldered to them. The cap is then closed and sealed with Stycast® 2850. Superfluid helium entering from one capillary into the heat exchanger will rapidly fill the silver powder crevices and be in thermal contact with the whole unit over a large area. Each silver sinter is filled with ~1 g of silver powder and has a surface area of typically 1 to 3 m^2 [5]. *Source*: [4].

cross section of the capillaries will also increase the pumping time of the experimental cell for up to several days. This creates issues for evacuating the experimental cell and reducing the impurities within a reasonable timeframe.

Another route to minimize heat leaks, according to Eq. (A.1), is to reduce the thermal gradient across the circuit where the thermal conductivity of ^{4}He is highest. To achieve this, the capillary coming inside the refrigerator is connected to a series of heat exchangers, as shown in Fig. 3–3, which will efficiently precool the ^{4}He in stages before reaching the cell. The heat exchangers are made out of copper cylinders with a blind hole filled with sintered silver powder[6]. The granularity of the sinter tremendously increases the surface area and so the thermal exchange between the ^{4}He inside the capillary circuit and the part of the refrigerator holding the exchanger. Meanwhile the high thermal conductivity of silver helps to achieve a high heat transfer rate. In this design implemented by Michel Savard [4], a first heat exchanger is located near the 1 K pot. A second one is located between the ^{3}He pot and the cell, on the silver tail. Unfortunately, the ^{4}He inside the capillaries did create a heat leak from the 1 K pot to the colder ^{3}He pot and thus prevented the refrigerator to cool down to its normal base temperature of 300 mK. The lowest stable temperature that could be achieved was 0.87 K and it could only be maintained for 5 to 6 hours before the ^{3}He liquid had completely boiled off.

---

[6] Sintering is the process of forming a solid mass of material by compacting a powder and/or heating it below its temperature of liquefaction [5, 7].

3.1.2 Dilution dry refrigerator

The functional principle of a dry dilution refrigerator is based on some interesting properties of the ^{3}He and ^{4}He quantum liquids when mixed together. The diluted fraction of ^{3}He inside a ^{3}He – ^{4}He mixture does not phase separate from the ^{4}He fraction, even as $T \to 0$, but indeed remains soluble into ^{4}He. This remarkable fact is due to the smaller mass and hence larger zero-point motion of the ^{3}He atoms. As a result, they are more likely to "bind" with ^{4}He atoms than with other ^{3}He atoms. The diluted fraction of ^{3}He can represent up to 6.6% of the total number of atoms inside the mixture [6]. When ^{3}He atoms dilute themselves from a pure liquid of ^{3}He inside the ^{3}He – ^{4}He mixture, there is a net enthalpy difference which thermodynamically contributes to carry heat away from the pure liquid ^{3}He. This is the crucial process which allows cooling to occur inside a dilution refrigerator. In a dry refrigerator, the mixture is liquefied and cooled by the combined action of a compressor and a pulse tube, which acts at the 4 K plate level shown in Fig. 3–4. Once the liquefied mixture fills the circuit below the 4 K plate, a mechanical pump located outside the refrigerator is activated to lower the pressure inside the *still*. Because the saturated vapor pressure of ^{3}He is larger than that of ^{4}He, preferentially the ^{3}He atoms will leave the mixture, will be then collected at the pump exhaust and re-liquefied by the pulse tube prior to being integrated back to the *mixing chamber*. The ^{3}He is further cooled on its way down to the mixing chamber by way of heat exchange with the still pot and the cold ^{3}He rich mixture going from the mixing chamber up to the still. Once the liquid ^{3}He reaches the mixing chamber, approximately 6–6.6% will be diluted in the ^{3}He – ^{4}He mixture.

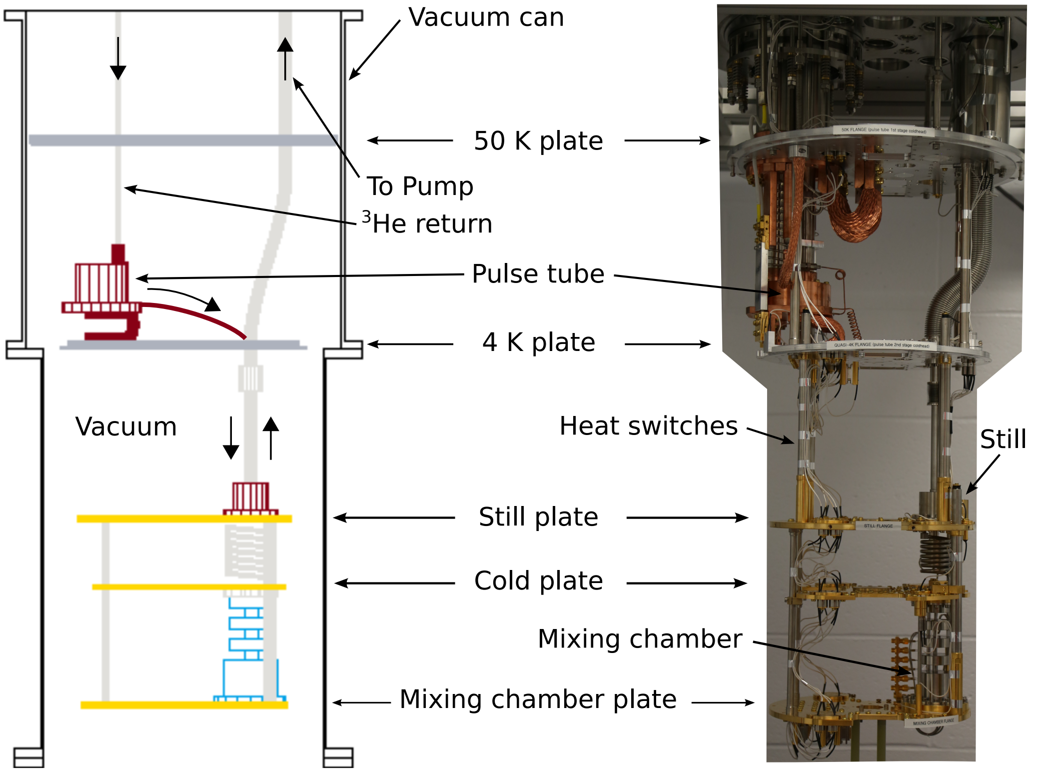

Figure 3–4: Diagram and photograph of the main components of a dilution dry refrigerator. On the right side is a photograph of the refrigerator matching the schematics on the left. All components inside the vacuum can are maintained in vacuum by a turbo pump ($3 \cdot 10^{-6}$ mbar). Not shown in the diagram are the copper and aluminum cans used to shield the components from radiations. The 4 K plate is cooled by the pulse tube, and all the lower plates are subsequently cooled by the dilution cycle described in the text. Although the coldest point of the refrigerator is the mixing chamber plate, the experimental cell is mounted on the cold plate so as to avoid heat leakage reaching the mixing chamber via the capillaries. The lowest temperature reached by the cold plate is between 30 and 50 mK. The diagram is based on the manufacturer's plans, BlueFors Cryogenics©. The distance between the 50 K plate and the mixing chamber plate is 80 cm. A schematic of a dilution cycle can be found in Appendix B–1.

3.1.2.1 Experimental cell

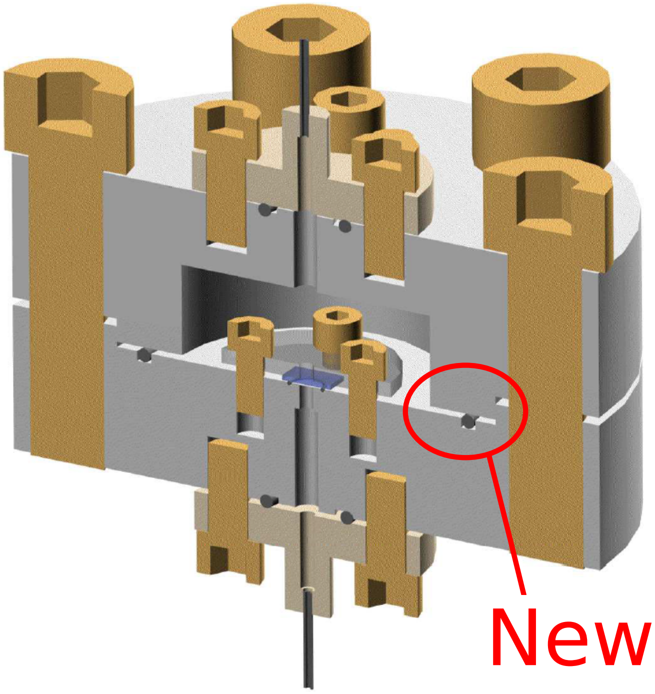

Figure 3–5: CAD drawing of the coin silver experimental cell which was mounted inside the dilution refrigerator. Its design is very similar to the previous experimental cell (*cf.* Fig. 3–2). It was improved only by carving a groove in the bottom part (see red ellipse) for seating the indium o-ring sealing the top and bottom parts. Although a simple design improvement, it tremendously helped to reduce the seal's failures of the experimental cell. The available volume of the main chamber (subtracting the volume of the screws and of the Invar® plate) is $\simeq$0.42 cm^3. *Art credits*: Richard Talbot.

Only two modifications were made to the design of the experimental cell described in section 3.1.1.1. First, a larger groove was carved in the bottom flange, as shown in Fig. 3–5. Second, the top flange had a step designed to press against an indium o-ring placed in the bottom's groove. These modifications drastically improved the reliability of sealing the cell hermetically and greatly reduced leakage from the inside of the cell to the vacuum can at low temperatures. The 0-80 screws holding the Invar® plate are in stainless steel 316.

3.1.2.2 Measurement and control of the temperature

The thermometer used to monitor the temperature of the experimental cell is a RuOx resistive chip thermometer (LakeShore® Rx102A-BR). It was calibrated against the NIST calibrated mixing plate thermometer provided with the BlueFors Cryogenics© dilution refrigerator. It is then mounted on a gold plated copper holder with Apiezon® grease. The holder includes a spool for the winding of thermometer leads and it ensures that both are well thermalized. The leads are connected in such a way that its resistance is measured in a 4-point configuration. The holder is tightly maintained on the silver cell with a 316 stainless steel screw.

3.1.2.3 Heat exchangers

The experimental circuit mounted on the dilution refrigerator contains several heat exchangers anchored on each plate of the refrigerator, namely the 50 K plate, the 4 K plate, the still plate and the cold plate. The design of the heat exchanger, in display in Fig. 3–6, is the same for all the plates. The heat exchanger consists of a copper body and a brass cap. A cavity was drilled inside the body and silver powder was sintered in it. The internal surface of the cavity was first coated with a few nanometers of gold to avoid oxidation. Then, silver powder (Alfa Aesar 120 mesh, Premion® 99.999%) was pressed with a packing fraction of $\sim$0.5 inside the cavity. Each heat exchanger holds between 0.7 and 0.8 g of silver powder, which represents between 0.7 and 2.4 m^3 of surface area. The procedure was inspired from Ref. [5]. The brass cap was tapped to fit in the 3/8-24 threads of the copper body's shaft, allowing the cap to be screwed onto the body. The heat exchanger is sealed using indium wire coiled around the threads of the copper body. The indium is pressed against the threads with a soldering iron at 150 °C and the cap is screwed on and off repeatedly, until the indium has coated the threads uniformly over at least 3 whole loops. This sealing method has the advantage to only expose the ^{4}He inside the capillary circuit to metals, as opposed to the previous design using Stycast® 2850. Indeed, glues are known to outgas and this could lead to an increase in impurities ultimately risking to block the nanopore during the cooldowns.

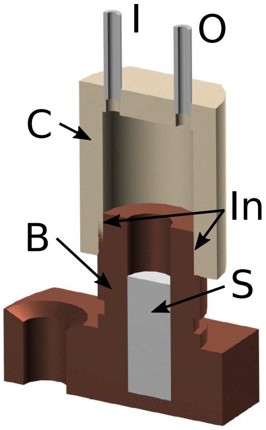

Figure 3–6: CAD drawing of the heat exchanger which was installed inside the dilution refrigerator. The stainless steel capillaries at the inlet (I) and outlet (O) are silver-soldered to the brass cap (C) of the heat exchanger, whereas the copper-nickel capillaries are tin-soldered. The sinter (S) is made out of an Alfa Aesar 120 mesh, Premion® 99.999% silver powder compacted to a ∼0.5 packing fraction. The cap can be screwed onto the copper body (B) which is threaded. The seal between the body and the cap is made with indium (In) spread onto the threads of the body. *Art credits*: Richard Talbot.

The choice of material and dimensioning of the capillaries were made to optimize the setup under several constraints:

i. The heat leak to each plate due to ^{4}He inside the capillaries should be as small as possible, *i.e.* the capillaries should be long and have a small inner diameter.

ii. The pumpdown time for the whole circuit should be as short as possible, *i.e.* the capillaries should be short and have a large inner diameter.

iii. The heat leak due to the empty capillaries should not prevent the refrigerator to reach its base temperature when used for other experiments, *i.e.* the capillaries should have thin walls and the material should have a poor thermal conductivity at low temperatures.

The capillaries from the gas panel down to the still plate were chosen to be made out of stainless steel. As the temperature gets closer to a few Kelvin, the thermal conductivity of stainless steel becomes very poor compared to its room temperature value. To efficiently cool the stainless steel capillaries, several copper braids were silver-brazed around them. The braids were then firmly held onto the plates with screws for thermal anchoring. The capillaries from the still plate down to the experimental cell, located onto the cold plate, are made out of copper nickel. The return line from the experimental cell up to the top of the fridge is made out of a single stainless steel capillary, thermally anchored to the 4 K and 50 K plates with silver-soldered copper braids. The dimensions of the capillaries as well as the estimated heat leaks in vacuum are given in Appendix C.

3.2 Solid-state nanopore

Regarding potential ways to confine a fluid in a flow experiment, one obvious geometry comes to mind: a pipe. When adding the constraint that the pipe should have nanometric dimensions, one may think at first about carbon nanotubes. The problem here is leak-tightness. While perhaps not impossible, it would be extremely difficult to manipulate and seal a single nanotube into a macroscopic circuit. It would even be harder to do so if the fluid in question is amongst the least viscous ones, namely superfluid ^{4}He, flowing through the tinniest cracks.

Thankfully, there is another approach which is to craft a pipe by “drilling” a hole into a membrane. Indeed, this makes no difference for the fluid confined inside the pipe, but it allows for the handling of the “pipe” on a macroscopic scale, thereby greatly simplifying the sealing problem. The next section will discuss the technique used to fabricate the nanopores, as well as potential alternatives which were developed by other research groups during the course of this thesis work.

3.2.1 Nanopore fabrication procedure

Over the past 10 years, interest in employing nanopores as nanosensors (*i.e.* DNA sequencing, or molecule filtering [8, 9]) stimulated the development of reliable nanopore fabrication processes [10]. This resulted in a number of approaches to fabricate nanopores in various types of membranes, such as ion/electron beam drilling [11, 12], track etching [13, 14], or dielectric breakdown [15]. As we are interested in creating a *single* nanopore, the beam techniques was found to be more adapted to our needs. The smallest beam spot that can be achieved is with an electron beam (0.5–1 nm, limited by magnetic lenses aberrations), which makes it an ideal candidate for our experiment.

3.2.1.1 Nanopore substrates

Single nanopores were drilled into commercially-available[7] , low-stress, amorphous silicon nitride (Si_3N_4) membranes. The Si_3N_4 membrane is free-standing onto a silicon substrate, as shown in Fig. 3–7. The size of the silicon substrate is 2 x 2 mm and 200 μm thick. It can be conveniently handled with plastic tweezers cleaned with isopropanol. The window of free-standing Si_3N_4 is usually a square with sides ranging from 10 to 50 μm, depending on the thickness of the membrane. Smaller pores are easier to drill in thinner membranes. However, as Si_3N_4 is amorphous, the fear of ^{4}He diffusing through the membrane led us to limit ourselves to a minimum thickness of 20 nm for our nanopores. The only nanopore we produced and in which we could measure superfluid ^{4}He flow was drilled into a 30 nm thick membrane[8] .

3.2.1.2 Transmission Electron Microscope

The focused electron beam of a Transmission Electron Microscope (TEM) was used to drill a single nanopore through the Si_3N_4 membrane. The TEM employed is a JEM-2100F, located at the École Polytechnique de Montréal. The electrons accelerating voltage was set to 200 kV.

After adjusting the settings to have a well-focused image at a magnification of 500kX, the largest beam aperture was chosen to maximize the beam intensity available for drilling. The beam was first converged as close as possible to a single

---

[7] The membranes used for this work were purchased from Silson® or Norcada®.

[8] Failure to measure superfluid flow can have several origins: the nanopore can get filled by impurities (Appendix A1 of Ref. [4]), the Si_3N_4 membrane can break, or one of the indium seals can leak at low temperature.

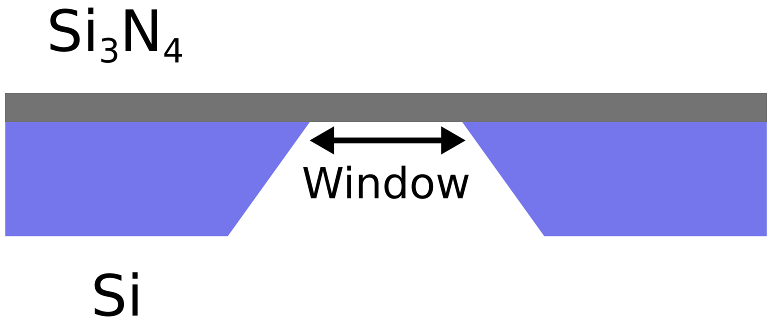

Figure 3–7: Schematic side view of a TEM membrane used for drilling a single nanopore. A Si_3N_4 layer (grey/top) of controlled thickness is deposited on a silicon substrate (blue/bottom), which is then etched to expose a free standing window of Si_3N_4. The nanopore is drilled in this window. The suppliers quote them with an uncertainty in the thickness within 7% of the total thickness [16].

spot, and then defocused to +1500 nm to begin the drilling process[9]. The pore would then typically open within minutes of exposure, sometimes even less than a minute for the 10 nm thick membranes. When the beam is converged in one spot, it is no longer possible to visualize the membrane simultaneously. It is therefore difficult to estimate when a pore opens across the membrane and to stop the drilling process. Nevertheless, a signature of an open pore is the appearance of a faint thin ring around the beam spot. Therefore, the smallest nanopore achievable with this technique depends on the beam spot size of the TEM. The beam spot size is mainly limited by the spherical aberrations of the objective lense. For the JEM-2100F, the beam spot could not be made smaller than 0.5–1 nm. Pores as small as 0.7 nm could be drilled with this TEM, although they would unfortunately not remain open

---

[9] This defocusing value was experimentally found to drill well.

for more than a few hours [17]. Other groups report nanopores with similar sizes [12, 18].

Pores would sometime close within hours after being opened. In order to decrease the risk of mounting an unstable pore inside the experimental cell, our procedure was to wait at least one day, and then re-image the membrane. If the pore was still open then, we would proceed and mount it inside the experimental cell for a cooldown.

3.2.1.3 Atomic Layer Deposition

In an attempt to reduce the size of the larger nanopores (*i.e.* those with more than 10 nm diameter) produced with the TEM, Atomic Layer Deposition (ALD) of Hafnium Oxide (HfO) was also employed. ALD is an isotropic process depositing successive layers of a material onto three-dimensional structures through cycles of injection and purge. The total thickness of the HfO layer can be controlled with a precision down to 0.1 nm [19]. The membrane would then be coated as shown in Fig. 3–8, and the layer of HfO helps to reduce the diameter of an existing pore.

Alternatively, it was demonstrated in Ref. [18] that a nanopore can be drilled directly in a HfO membrane. Thus, a thin layer of HfO of a few nanometers only, could also be deposited on top of a blank Si_3N_4 membrane prior to the drilling process. The stability of a pore opened by this procedure should be better than that of a pore in bare Si_3N_4, according to the results in Ref. [18]. We unfortunately did not have the time to conduct enough successful trials of this pre-layer of HfO ALD procedure, nor master the ALD deposition reactor. However we could successfully achieve a proof-of-concept verification for the filling of an already open pore.

One of our few experimental trials is shown in Fig. 3–9, which displays a ∼21 nm diameter pore drilled through a 30 nm membrane before and after a HfO ALD.

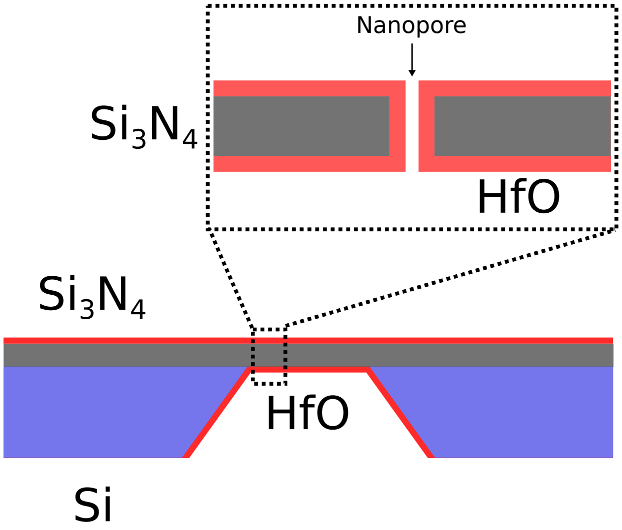

Figure 3–8: Schematic side view of a TEM membrane coated with a layer of HfO deposited by ALD. The insert illustrates how a pre-existing nanopore can be filled by ALD, in principle.

The image clearly shows HfO deposited on the inner wall of the pore. A recent publication also reports HfO ALD in porous silicon, with an average pore diameter of 4.8 nm [20]. Scanning Electron Microscope (SEM) imaging of their sample showed that HfO ALD coated the first 100 nm inside the pores. This gives us confidence in the technique, and that indeed it can help us to uniformly reduce the size of our pores. The downside of this approach, however, is that it adds more steps to the sample fabrication process, *i.e.* extra TEM imaging sessions before and after the ALD process and the ALD process itself. These extra steps might increase the nanopore production time by several days, as both the ALD reactor and the TEM are shared-user facilities.

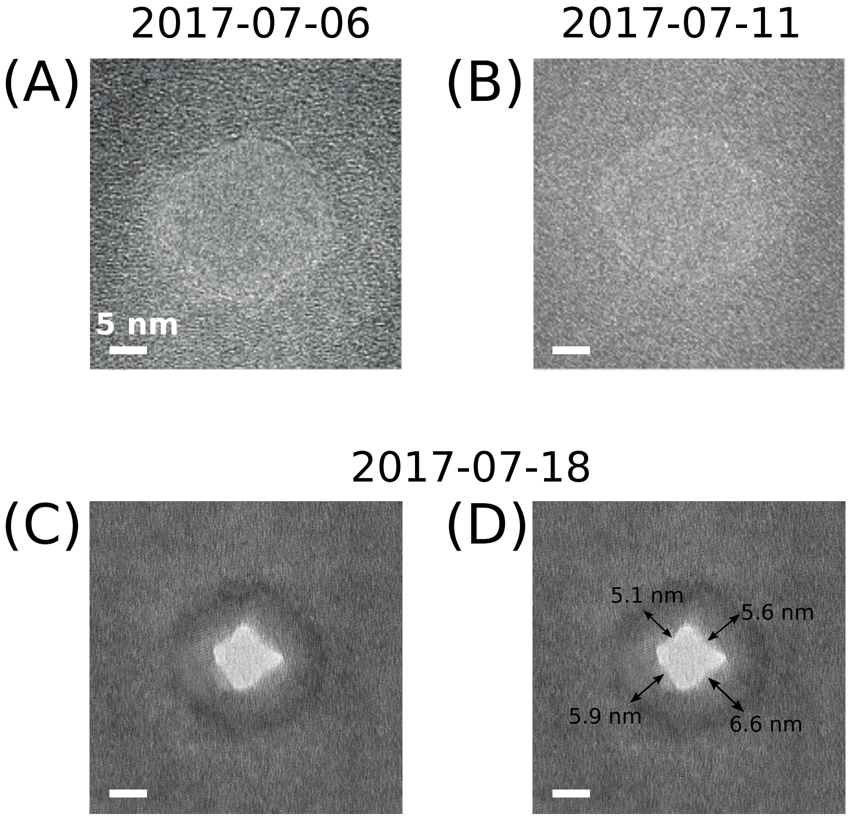

Figure 3–9: TEM top views of a nanopore in a 30 nm thick Si_3N_4 membrane, illustrating how the ALD process can be employed to significantly reduce the size of pre-existing nanopores. **(A)** Nanopore on the day of its drilling. **(B)** The same nanopore a week later. Its shape became more circular, with an approximate diameter of ∼21 nm. **(C)** The same nanopore following HfO ALD. The previous dimension remains clearly visible, highlighted by a darker area. This darker area is a proof that ALD occurred on the inner wall of the pore. Indeed, the brightness of the image is correlated with the amount of HfO the electrons must cross prior to reaching the camera. **(D)** Estimates of the ALD layer thickness. This picture illustrates the sensitivity of the technique to the initial shape of the pore. Here, the ALD resulted in a channel with a squared cross section.

3.2.1.4 Controlled dielectric breakdown

During the course of this work, another technique to drill nanopores was developed, consisting in applying a low voltage (typically 18 V) across a TEM Si_3N_4 membrane dipped in a molar solution [15]. Due to the small thickness of the membrane, the induced electric field across the latter can reach several thousand V/m. Then, redox reactions occur stochastically on the surface of the membrane and there is a probability for two redox reactions to occur *vis-a-vis* from both sides. When this occurs, the thickness is reduced locally, thus increasing the tunneling probability of electrons. This triggers a runaway process where increased tunneling leads to local resistive heating, in turns leading to a higher probability of tunneling until the membrane melts due to Joule heating. This local melting process creates a nanopore. Once a pore is open, the ionic current across the membrane increases drastically. This increase is used as a trigger to drop the voltage to zero. The inventors of this method claim that only one pore opens across the membrane.

A major drawback of this technique for our use is that the nanopore appears at a random location on the membrane. When imaging the membrane with a TEM, it is thus very difficult and time-consuming to find the nanopore. For this reason alone, it was decided not to try this technique as consistency with our previous procedure was judged more important. Recently however, the same research group reported improvements of the technique by applying it to membranes with a thinned region [21]. The thickness of the membrane being inversely proportional to the probability of a dielectric breakdown across it, it narrows the area over which the nanopore is formed. In the future, this could become an alternative route to produce nanopores for our experiment.

3.2.2 Mount and cooldown procedure

In order to avoid as much as possible contaminants inside the circuit, the source and the drain (inlet and outlet as shown in Fig. 3–5, respectively) of the experimental cell are connected to 5N purity ^{4}He gas reservoir (overpressurized) when the cell is open to room atmosphere (*i.e.* $\simeq$70 mbar above atmospheric pressure). This way, a constant flow of ^{4}He prevents impurities to flow back inside the heat exchangers and the capillaries. The ^{4}He from the reservoir passes through a cold trap filled with activated charcoal in liquid nitrogen before reaching the source part of the capillary circuit inside the refrigerator.

The membrane is deposited on an indium o-ring made out of a 70 μm diameter indium wire. The o-ring itself sits on a groove in the silver cell's drain part, as displayed in Fig. 3–5. Using curved-tips tweezers, the Invar® plate with two 0-80 screws is placed above the silicon chip holding the Si_3N_4 membrane, without touching it. The two screws are delicately screwed into their holes to guide the plate, which is maintained parallel to the chip by the tweezers, until the plate touches the chip. The screws should not be tightened at this stage. The pit in the silicon chip leading to the Si_3N_4 membrane should be visible from the through hole of the Invar® plate when looking from above. A microscope camera connected to a computer was used for convenience. If the pit is not visible, it means that the membrane is not aligned with the drain and that ^{4}He will not be able to flow through the nanopore. The above procedure should then be repeated (the indium seal does not need to be replaced as it was not pressed on). Once the membrane's pit is visible through the Invar® plate hole, the two remaining 0-80 screws are inserted and all four screws are tightened to press the silicon chip uniformly on the indium o-ring. Care should be taken not to break the silicon chip by applying too much torque on the screws.

At this stage, the ^{4}He gas overpressure with respect to the atmosphere should be almost suppressed in the drain. This minimizes lateral motions of the silicon chip as it is pressed against its indium seal. Once the membrane seal is made, the cell is closed with another indium seal[10]. While starting to tighten the screws[11] in a star pattern, moisture inside the cell is purged by flowing ^{4}He gas through the source. The ^{4}He gas pressure at the source is monitored constantly while the cell is closed. Before the screws are too tight, the overpressure at the source is typically set to 120–160 mbar. It should decrease to 10–20 mbar before tightening the screws as this contributes to flush air outside the experimental cell.

The leak-tightness of the seal is tested several times during the cooldown procedure. A successful test at room temperature does not guarantee that the seal will be leak-tight at lower temperatures. However, a failed test at room temperature allows for another seal to be made prior to starting the cooldown. The first leak-test is performed by looking at the graph of the source overpressure versus time. As the screws are tightened, the overpressure should slowly stop decreasing and should become stable if the sealing is successful. The overpressure is then raised to 200 mbar. If it does not decrease over time, the source and drain part of the cell are being pumped on simultaneously to start the cleaning procedure. After an hour of pumping, the valve to the pump is closed to perform another leak-tightness test. If the pressure stabilizes after five minutes, the seal is considered leak-tight and the cleaning procedure starts.

---

[10] This seal is made with a 1 mm diameter indium wire.

[11] Each screw is turned a sixth of a turn at the time.

The cell is cleaned with 5 cycles of purge-pump of ^{4}He gas. Both the source and the drain are simultaneously filled with $\simeq$1000 mbar of ^{4}He gas and then pumped down until the pressure reaches $\simeq$30 mbar. Then, the source and drain are pumped down for a day. Our current gauge saturates at a pressure of approximately 8 mbar so it is not possible to know exactly the final pressure reached. A last leak-test of the cell's seal is performed at room temperature by releasing ^{4}He gas around the cell while pumping on it with a leak detector. Finally, a low pressure of ^{4}He gas ($\simeq$35–70 mbar) is set in the source side before the cooldown, while the drain side keeps being pumped on. This allows for early detection of a membrane or seal failure. In the case of a cooldown with the dry refrigerator, which can take up to 36 hours, having this pressure difference across the membrane is also useful to monitor the mass flow through the nanopore while the temperature decreases. When crossing the nitrogen solidification temperature, the flow has been observed to drop to its background level most likely due to some remaining nitrogen ice clogging the pore. Indeed, warming up the cell above liquid nitrogen temperature and cooling it back down was most of the time sufficient to restore the flow.

In order to minimize impurities inside the experimental cell, we designed a mini-activated charcoal cold trap, shown in Fig. 3–10. The impurities trap consists of a small amount ($\simeq$1–2 mg) of activated coconut charcoal powder wrapped in a copper mesh with grid size less than a micron. The copper mesh prevents bits of charcoal to wander around inside the experimental cell. Tin solder was used to seal the wrap. The activated charcoal provides a good *in situ* sorption pump to trap a high number of impurities as the temperature is lowered towards 4 K. The activated surface area of coconut charcoal varies between 1000 and 2000 m^2 per gram [22, 23]. Thus, our cold trap has a surface area of a few m^2. In comparison, the surface inside the experimental cell is on the order of 10^{-4} m^2. The maximum dimensions of the wrap are limited by the available space inside the cell (see Fig. 3–5). If the wrap sits on the 0-80 screws, its maximum thickness is 2 mm and its shape should fit within a circle of 6.9 mm radius. The wrap can be made thicker if it can fit within the four 0-80 screws. In the case of the experimental cell within the dry refrigerator, the thickness can be 3.3 mm and the wrap should either fit within a square of 4.7 mm side or within a circle of 2.4 mm radius. It is safer to make the dimensions a little bit smaller than the maximum dimensions to avoid ripping the copper mesh when closing the cell.

As this impurities trap was developed while installing the circuit on the dry refrigerator, we unfortunately did not have time to test it. Indeed, the cooldowns were first intended to check for leaks and we did not want to add an extra parameter that could modify the way the pressure varies inside the cell.

3.3 Mass flow measurement scheme

The experimental measurement of the mass flow is analogous to an electrical transport measurement in many aspects. A basic electrical characterization of a material is to measure its current-voltage (IV) curve, *i.e.* a known voltage is applied across a piece of the material and the current flowing between the contacts is measured. The procedure is then repeated for different voltages. The resistance R of the element is determined from the derivative of the IV graph. In the simple case of Ohm's law, the relation is linear,

$$V = RI. \tag{3.1}$$

In the fluid dynamics analogy, the pressure difference ΔP across the nanopore corresponds to the voltage V and the mass flow of ^{4}He atoms Q_m to the current of

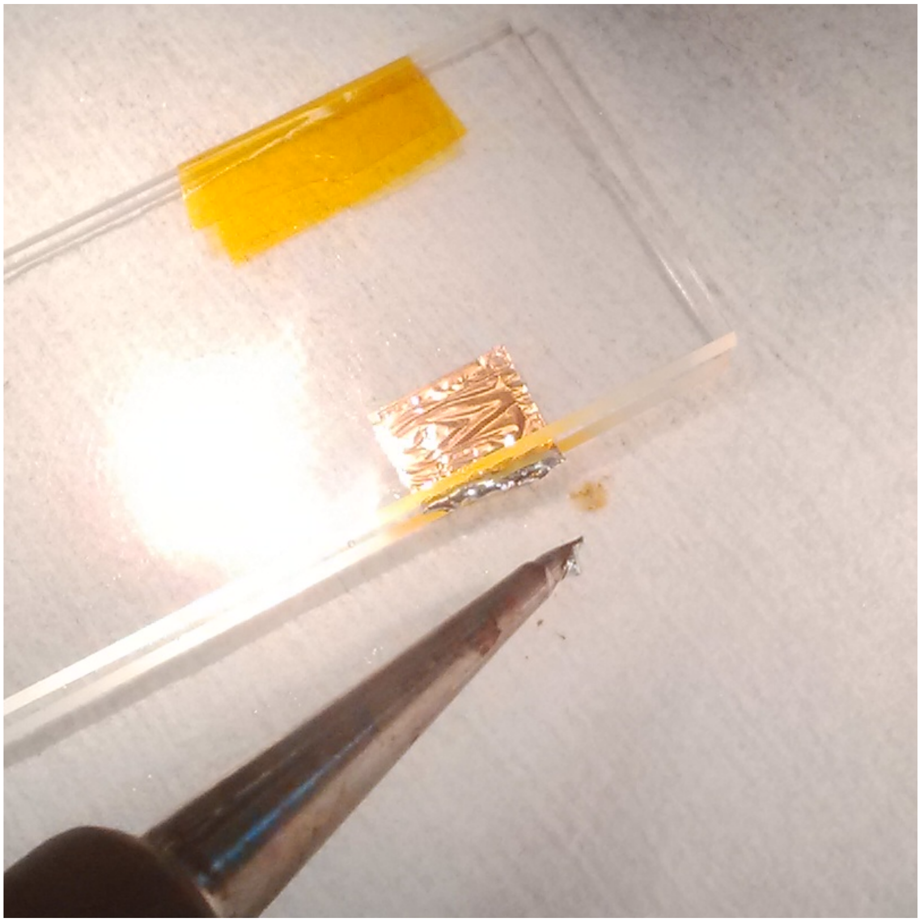

Figure 3–10: Activated charcoal cold trap in preparation: closing of the copper mesh wrap with tin solder. The wrap is similar in concept to a coffee pod. It is crafted by folding a rectangular sheet of copper mesh in two to create a square poach. The two sides adjacent to the folded side are folded on themselves using a tweezer. The poach is filled with charcoal powder and closed. The wrap cannot be too thick as the available space inside the cell is narrow (see text). This wrap measures 8 by 9 mm and was designed for the experimental cell of the wet ^{3}He refrigerator.

electrons I. The parameter linking Q_m and ΔP, which is usually of interest in fluid dynamics, is the conductance G, *i. e.* the inverse of the resistance to the flow. By analogy, Eq. (3.1) then reads,

$$\Delta P = \frac{1}{G} Q_m. \tag{3.2}$$

The mass flow rate Q_m in this thesis is always expressed in [pg·s^{-1}] and the pressure gradient ΔP will be displayed in [mbar]. However, we converted the mass flow rates into [kg·s^{-1}] and the pressures into [Pa] to compute the conductance G, so that it can be conveniently expressed in SI units, namely [m·s].

When measuring the resistance of electrical elements, in a 2-point configuration circuit, the resistance of the wires leading to the element should be made small compared to the resistance of the element itself so that the total resistance is almost equal to that of the element alone. Similarly, the conductance of the source and drain circuits should be much larger than the conductance of the nanopore, so that the mass flow through the circuit is essentially limited by the conductance of the nanopore, as can be seen in Fig. 3–11.

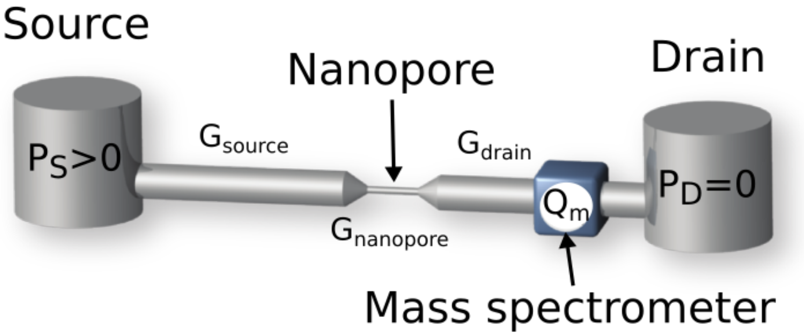

Figure 3–11: Experimental scheme of the measurement. A pressure gradient $\Delta P = P_S - P_D \simeq P_S$ is applied across the circuit and leads to a mass flow Q_m, which is measured with a mass spectrometer. The mass flow is limited by $G_{nanopore}$, because it is orders of magnitude smaller than the conductance of the source and drain circuits. In the analogous electrical analogy, if the resistance of a 3.14 nm radius and 30 nm long nanopore is set to 1 MΩ, then the resistances of the source and drain would be 15 mΩ and 3.1 Ω, respectively, for the ^{3}He refrigerator's circuit. For the dry refrigerator's circuit, the resistances of the source and drain would be 16 mΩ and 4 mΩ, respectively. *Based on* [4].

Calculations of the circuit's conductance G in the case of infinite pipe Poiseuille ^{4}He gas flow,

$$Q_{m,pipe,viscous} = \frac{\pi r^4}{8\eta L}\Delta P = G_{pipe,viscous}\Delta P, \tag{3.3}$$

and in the case of a Knudsen free-molecular flow,

$$Q_{m,pipe,Kn} = \frac{8r^3}{3L}\sqrt{\frac{\pi}{2R_s T}}\Delta P = G_{pipe,Kn}\Delta P, \tag{3.4}$$

were carried out for both experimental setups. Here, R_s is the specific perfect gas constant[12] for ^{4}He, L the pipe's length, r its radius, η the ^{4}He viscosity and T its temperature. The typical conductance of a nanopore lies five orders of magnitude below that of the circuits' conductance in both refrigerators. This therefore justifies neglecting the conductance of the n circuit's parts $G_{circuit,i}$ $(i \in \{1..., n\})$ in the data analysis since the total conductance, G_{tot}, is dominated by the pore's conductance $G_{nanopore}$,

$$G_{tot}^{-1} = G_{nanopore}^{-1} + \sum_{i=1}^{n} G_{circuit,i}^{-1} \simeq G_{nanopore}^{-1}. \tag{3.5}$$

As the nanopore diameter is decreased, the conductance of the pore will decrease even further, thus allowing us to keep neglecting the conductance of the circuit.

Mass flow measurements were carried out in three different phases of ^{4}He, *i.e.* gaseous (at liquid nitrogen temperature, 77 K), liquid (from 4–5 K to $T_\lambda \simeq 2.17$ K) and superfluid (from $T_\lambda \simeq 2.17$ K to 1 K in our case). Measurements in the first two phases are used to characterize $G_{nanopore}$ as a function of pressure at a fixed temperature and compare it to theoretical models of conductance. This will be further described in section 4.1. Fitting the experimental data to these models

---

[12] It is equal to the product of Avogadro's number N_A and Boltzmann's constant divided by the molar mass M_m of the gas, $R_s = \frac{N_A k_B}{M_m}$.

provides us with two independent *in situ*[13] estimates of the nanopore's dimensions. The superfluid phase is however the most interesting one and the ultimate goal of this study. Measurements of the mass flow as a function of the pressure at constant temperature as well as measurements of the mass flow as a function of temperature at constant pressure were performed in superfluid ^{4}He, with the results presented in chapter 4.

3.4 Mass flow measurement instrumentation

The ^{4}He mass flow is measured with a commercial leak detector (Pfeiffer Smart Test® HLT560). It consists of a vacuum turbomolecular pump connected in series to a mass spectrometer. Only the atoms with an atomic mass from 2 to 4 can be measured with this mass spectrometer, enabling us to measure both ^{4}He or ^{3}He flow.

3.4.1 Calibration

The leak detector was calibrated with ^{4}He standard leaks NIST certified, with values of $4.5 \pm 10\%$ pg/s and $3.7 \cdot 10^{-2} \pm 25\%$ pg/s. The calibration was performed regularly between measurements and after extended periods when the leak detector was left idling. The calibrated leaks consist of ^{4}He gas cylinders with an initial overpressure from one standard atmospheric pressure on the order of $\simeq$70 mbar, connected in series to a valve and a leak element. The leak elements provides a controlled ^{4}He gas flow rate which is used for the calibration of the mass spectrometer [24]. The flow rate on the calibration day has to be adjusted from the certified value

---

[13] These *in situ* estimates are important because the nanopore could shrink after the TEM imaging, or there could be impurities on the pore's inner surface, reducing its effective radius.

based on the time Δt elapsed since the certification date, the variation from the certification temperature ΔT. The depletions coefficients C_t and C_T are provided by the manufacturer. The exact relations between these parameters are also provided by the manufacturers.

3.4.2 Signal-to-noise ratio improvement: ^{4}He background removal

The leak detector is sensitive to ^{4}He gas in the air surrounding them since KF vacuum flanges do have a small leak rate[14]. This was problematic as in a low temperature laboratory with wet refrigerators, large amounts of ^{4}He gas are then released (during cryogen transfer or simply due to normal boil-off). To circumvent this, a special cabinet was built to enclose the mass spectrometer and designed to be slightly overpressurized above one atmosphere. It is displayed in Fig. 3–12. The cabinet was overpressurized with compressed air. The cabinet successfully decreased the lowest background ^{4}He signal of the mass spectrometer by a factor five, down to $1.6 \cdot 10^{-2}$ pg/s. It also attenuated the rise in the background signal during liquid ^{4}He transfers into the wet refrigerators by one order of magnitude, reducing the timeframe needed for the background signal to go back to its lowest value from a whole day to a few hours.

---

[14] The ^{4}He leak rate of one KF25 flange due to permeation of ^{4}He through the Viton® o-rings is estimated to be on the order of $1.1 \cdot 10^{-2}$ pg/s per o-ring. For a pressure difference of 10^5 Pa, this leads to a conductance of $1.1 \cdot 10^{-22}$ m·s. The electrical analog is a leak to electrical ground with a resistance of 182 MΩ, provided the resistance due to the nanopore is equivalent to 1 MΩ as in Fig. 3–11.

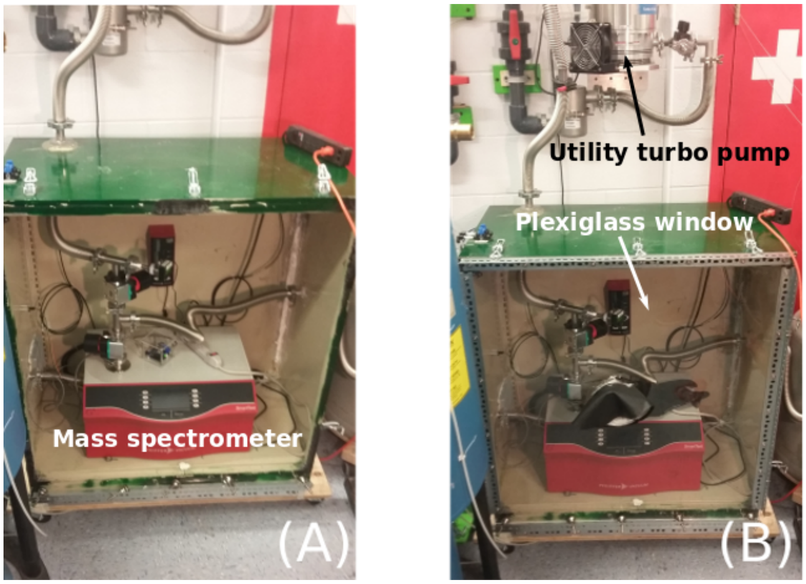

Figure 3–12: **(A)** Cabinet enclosing the mass spectrometer. The tube coming from the right connects to the experimental circuit inside the refrigerator. The tube going upwards connects to a utility turbo pump. The valves allow either the mass spectrometer or the utility pump to connect to the circuit inside the refrigerator. **(B)** Cabinet closed by a Plexiglas window. A glove is used to operate the valves. Above the cabinet, the utility turbo molecular pump can be seen.

3.4.3 Data acquisition and analysis tools

The data outputted by the pressure gauges, resistance bridge (thermometers) and mass spectrometer were acquired remotely with a computer software and RS-232 or GPIB interfaces. The computer software was entirely developed in Python 2 language by Benjamin Schmidt and the author of this thesis [25] (recently also compatible for Python 3 [26]). The entire code is too large to be included in the Appendix, however it can be found on the publicly available GitHub [27] or GitLab [28]. All further data treatment, analysis, publication figures, as well as figures in the present thesis, were performed with the open source Python modules *Matplotlib* and *Scipy* [29, 30].

References

[1] de Waele, A. T. A. M. *J. Low Temp. Phys.* **164**, 179 (2011).

[2] URL : Responding to the U.S. research community's liquid helium crisis (2016). `https://www.aps.org/policy/reports/popa-reports/upload/HeliumReport.pdf`.

[3] Savard, M., Dauphinais, G. & Gervais, G. *Phys. Rev. Lett.* **107**, 254501 (2011).

[4] Savard, M. *Towards a One-Dimensional State of Neutral Matter.* Ph.D. thesis, McGill University (2014). `http://gervaislab.mcgill.ca/Savard_PhD_Thesis.pdf`.

[5] Robertson, R. J., Guillon, F. & Harrison, J. P. *Can. J. Phys.* **61**, 164–176 (1983).

[6] Pobell, F. *Matter and methods at low temperatures* (Springer, 2007).

[7] URL : Wikipedia article on sintering (2018). `https://en.wikipedia.org/wiki/Sintering`.

[8] Li, J., Gershow, M., Stein, D., Brandin, E. & Golovchenko, J. A. *Nat. Mater.* **2**, 611–615 (2003).

[9] Branton, D. *et al.* *Nat. Biotechnol.* **26**, 1146–1153 (2008).

[10] Tang, Z. *et al.* *J. Nanomater. Nanotechnol.* **6**, 35 (2016).

[11] Krapf, D. *et al.* *Nano Lett.* **6**, 105–109 (2006).

[12] van den Hout M. *et al.* *Nanotechnology* **21**, 115304 (2010).

[13] Siwy, Z. *et al.* *Surf. Sci.* **532-535**, 1061–1066 (2003).

[14] Velasco, A. E., Friedman, S. G., Pevarnik, M., Siwy, Z. S. & Taborek, P. *Phys. Rev. E* **86** (2012).

[15] Kwok, H., Briggs, K. & Tabard-Cossa, V. *PLoS ONE* **9**, e92880 (2014).

[16] Norcada. TEM membranes spec. sheet (2017). `https://www.norcada.com/wp-content/uploads/2017/03/TEM-Grid-Specsheet-Rev-6.pdf`.

[17] Dauphinais, G. *Fabrication, Structural Relaxation, and Flow in Solid-State Nanopores.* Master's thesis, McGill University (2011). `http://gervaislab.mcgill.ca/Dauphinais_MSc_Thesis.pdf`.

[18] Larkin, J. *et al. ACS Nano* **7**, 10121—-10128 (2013).

[19] Johnson, R., Hultqvist, A. & Bent, S. F. *Mater. Today* **17**, 236–246 (2014).

[20] Kovacs, A. & Mescheder, U. *J. Vac. Sci. Technol.* **36**, 031508 (2018).

[21] Carlsen, A. T., Briggs, K., Hall, A. R. & Tabard-Cossa, V. *Nanotechnology* **28**, 085304 (2017).

[22] Yang, K. *et al. Bioresour. Technol.* **101**, 6163–6169 (2010).

[23] Martins, D. *et al.* Low temperature adsorption versus pore size in activated carbons. In *Proc. 16th International Cryocooler Conference, Inc.* (2011).

[24] URL : Laco tracer gas leak standards (2018). `https://www.lacotech.com/c/leak-standards/tracer-gas-leak-standards-with-gas-reservoir`.

[25] URL : (Py2). `https://www.python.org/downloads/release/python-2715/`.

[26] URL : (Py3). `https://www.python.org/downloads/release/python-365/`.

[27] URL : Schimdt, B. & Duc, P.-F. Labgui data acquisition on github (2013). `https://github.com/LabGUI/LabGUI`.

[28] URL : Schimdt, B. & Duc, P.-F. Labgui data acquisition on gitlab (2018). `https://gitlab.com/Bachibouzouk/LabGUI`.

[29] URL : (Matplotlib). `https://matplotlib.org/`.

[30] URL : (Scipy). `https://www.scipy.org/`.

CHAPTER 4

Quasi–one-dimensional superfluidity

In this chapter, we will first present mass flow measurements made through a *single* nanopore with the smallest radius ever used in a helium transport experiment [1]. We will then compare these measurements with previous data obtained by our research group in larger nanopores [2, 3], as well as with data previously reported in the literature. We will discuss at length the effects caused by the strong radial confinement. Finally, the scaling of the critical velocity and the recent theoretical advances made by Adrian Del Maestro and Bernd Rosenow [4] will be discussed.

The proof-of-concept experiment of superfluid mass transport though a nanopore was achieved by Michel Savard *et al.* at McGill University. For extensive details on the theory of mass flow through a nanopore, we refer the reader to his thesis [3] and earlier works [2, 5].

4.1 ^{4}He mass flow in a sub-ten nanometer pore

Since our aim is to study how lowering the dimensionality affects superfluidity, an accurate determination of the nanopore's geometry is of the utmost importance. In particular, the radius of the pore is the most important parameter governing the crossover between a 3D and 1D quantum state. In our work, we determine its value using three independent methods. The first one is based on straightforward TEM imaging of the pore shortly before the sample is mounted into the experimental cell, as shown in Fig. 4–1. The other two procedures, described in the following subsections, provide *in situ* values using a fit of the experimental conductance[1] G_{exp} to theoretical models in both the gas and normal liquid phases of ^{4}He. The length of the nanopore is fixed by the thickness of the Si_3N_4 membrane provided by the manufacturer, with a tolerance of 7%, *i.e.* (30 ± 2.1) nm [6].

4.1.1 Mass flow in the gaseous Knudsen regime

A gas flow experiment was initially performed at 77 K in order to obtain a first *in situ* characterization of the pore radius R. The methodology is similar to that reported in Ref. [5] where the conductance G_{exp} of the nanopore is measured as a function of the dimensionless Knudsen number Kn, defined here as the ratio of the atoms' mean free path[2], λ_{mfp}, to the nanopore diameter, $D = 2R$,

$$Kn \equiv \frac{\lambda_{mfp}}{2R} = \frac{k_B T}{2\sqrt{2}\pi\sigma^2 PR}. \tag{4.1}$$

---

[1] The conductance is defined as the ratio of the measured mass flow, $Q_{m,exp}$, to the pressure difference ΔP, applied across the nanopore, $G_{exp} = Q_{m,exp}/\Delta P$.

[2] The mean free path used here is based on non-interacting particles.

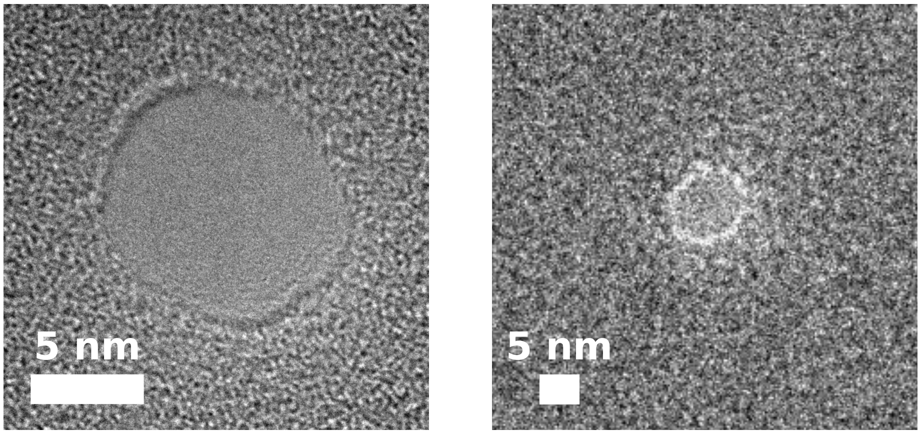

Figure 4–1: TEM images of the nanopore used in this study. **(Left)** Image taken with a JEM-2100F TEM 15 minutes after the pore was drilled. Its radius determined by an analysis of the image line profile is 5.1±0.2 nm. **(Right)** Image of the same pore a few hours prior to mounting inside experimental cell, taken with a FEI TecnaiG2F20 TEM. This TEM has a lower resolution at high magnification than the JEM-2100F one. Its radius has shrunk since its initial opening to 4.3 ± 0.2 nm.

.

.

The Knudsen number is a function of both the temperature T and pressure P. In Eq. (4.1), the factor $\sqrt{2}$ arises from assuming a Maxwell distribution for the velocities of the individual atoms, k_B is the Boltzmann constant and σ is the cross-section, or hard-shell, diameter. For ^{4}He, σ is equal to $2.6 \cdot 10^{-10}$m [7][3]. The Knudsen number is a dimensionless number, useful to determine whether statistical or continuum mechanics is a more suitable description for the mass flow. A cartoon of the different flow regimes as a function of Kn is provided in Fig. 4–2. A low value, $Kn \ll 1$, means the gas is in a regime of viscous flow and hence in the realm of continuum mechanics. A high value, $Kn \gg 1$, corresponds to the Knudsen regime

---

[3] In Ref. [3], $\sigma = 2.18 \cdot 10^{-10}$m was used. However the value found in Ref. [7] is from more recent measurements.

where the mean free path is much larger than the nanopore diameter and so the particles undergo ballistic motions, *i.e.* interactions between particles are rare.

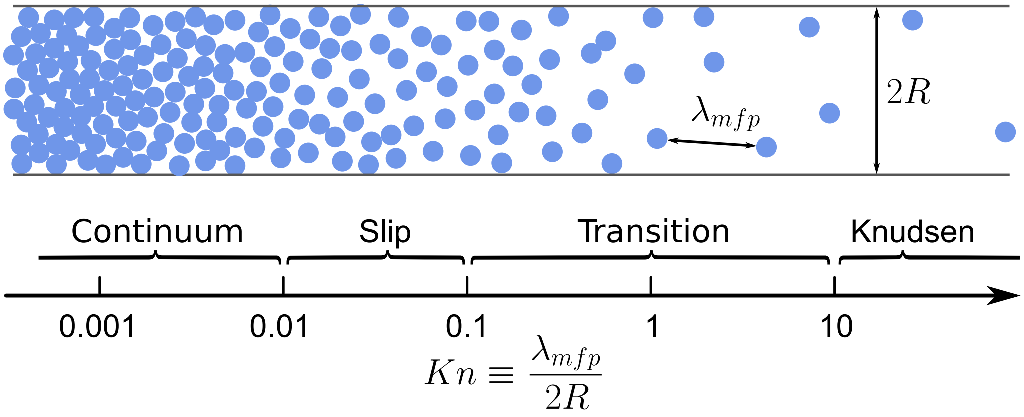

Figure 4–2: Schematic illustration of the density of particles as a function of the Knudsen number, Kn. The value of Kn reflects various fluid dynamic regimes, as indicated on the scale. *Source*: [3].

Due to the small radius of our nanopore, the Knudsen number is sufficiently high across the range of experimental pressures so that we are always in the Knudsen regime and as such, we can neglect contributions from viscous flow. In the Knudsen regime, the conductance is given by [8, 9]

$$G_{Kn} = R^2 \kappa_{Cl}(R, L, \theta) \sqrt{\frac{\pi}{2R_s T}}, \tag{4.2}$$

where R_s is the specific perfect gas constant for ^{4}He, L is the nanopore's length and θ is the opening angle of the nanopore, as illustrated in Fig. 4–3. Note that the conductance is independent of the applied pressure, as can be seen in Eq. (4.2). The determination of the opening angle θ is discussed in section 4.1 of Ref. [3].

The *Clausing factor*, $\kappa_{Cl}(R, L, \theta)$, is a geometrical factor that accounts for the probability for an atom to go from one side of the nanopore to the other by bouncing off the walls [8, 10]. Graphs of the Clausing factor as a function of θ and L/R are provided in Figs. D–2 and D–3, respectively.

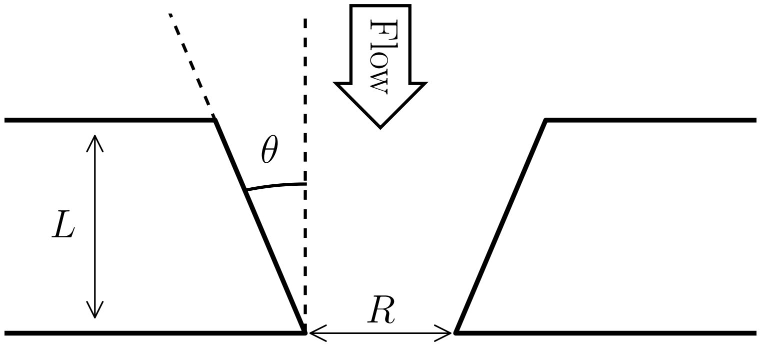

Figure 4–3: Cross-section view of a nanopore, showing the definition of θ used in the Clausing factor. When $\theta = 0°$ the nanopore is a perfect cylinder. *Source*: [10].

.

Fig. 4–4 shows the value of the conductance G_{exp} as a function of Knudsen number Kn. The data at higher Kn have larger uncertainties because they were taken at very low pressures/flow regimes where the mass spectrometer's signal-to-noise ratio is lower. The radius of the nanopore and its uncertainty, ΔR, were extracted from the minimization of $G_{Kn}(R) - G_{exp}$ and $G_{Kn}(R \pm \Delta R) - (G_{exp} \pm \delta G_{exp})$, for which $L = 30 \pm 2.1$ nm and $\theta = 15 \pm 5°$ and where G_{exp} is the average of the values measured at different pressures. Here, the deviation δG_{exp} corresponds to one standard deviation from G_{exp}. The extracted value for the radius was found to be $R^{Kn} = 3.06 \pm 0.13$ nm. It is significantly smaller than the value of 4.3 ± 0.20 nm, obtained by TEM imaging at room temperature. It is because the nanopore shrinks over time, and this is consistent with previous work of Dauphinais *et al.* [11], and Savard *et al.* [3, 5]. Moreover, the shrinkage has been observed *live* at several occasions during the fabrication process of theses Si_3N_4 nanopores.

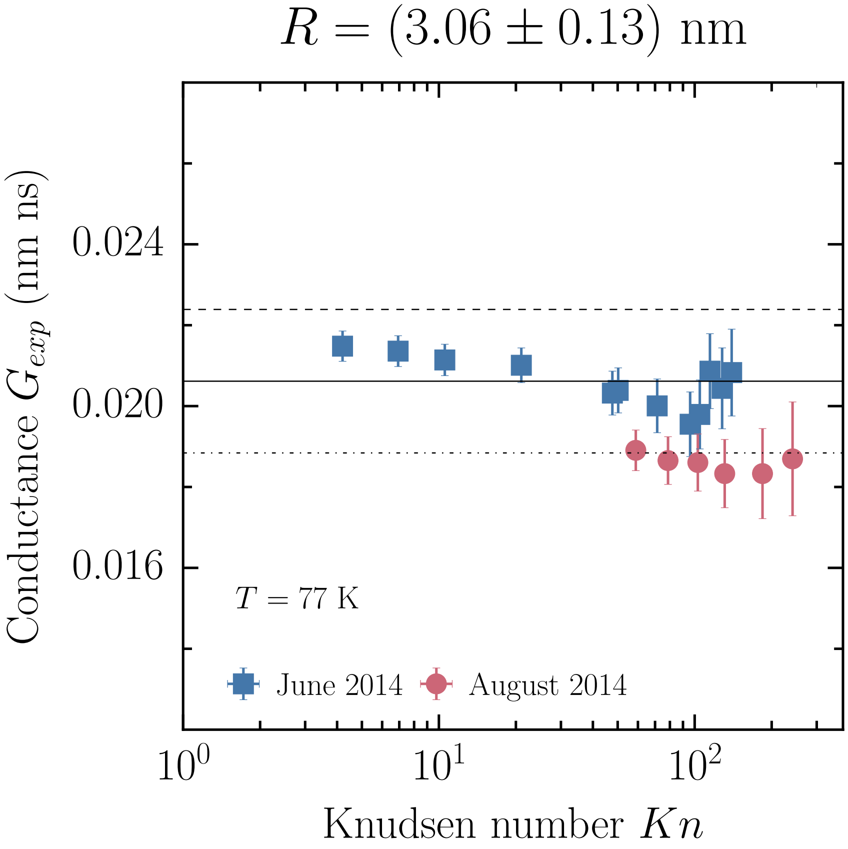

Figure 4–4: Determination of the radius by Knudsen effusion. Conductance values obtained from the ratio of the measured mass flow and the applied pressure gradient across the nanopore. The red circles and the blue squares are Knudsen effusion measurements at 77 K performed prior and after the superfluid flow measurements, respectively. The two datasets were acquired two months apart from each other. The solid line corresponds to the average conductance, G_{exp}, of the square data points above $Kn = 10$. The dashed and dashed-dotted lines correspond to $G_{exp} + \delta G_{exp}$ and $G_{exp} - \delta G_{exp}$, respectively.

.

4.1.2 Mass flow in the normal liquid phase

A second *in situ* estimate of the pore radius R was made with pressure-driven flow experiments in the normal phase of ^{4}He, at temperatures above T_λ. In this phase, the flow through the nanopore is viscously dissipative, and is expected to follow the model developed for a short pipe by Langhaar [12], based on the Navier-Stokes equations. The pressure at the outlet of the pore being close to vacuum $P_{outlet} \simeq 0$, we consider that $\Delta P = P_{inlet} - P_{outlet} \simeq P_{inlet} \equiv P$. The pressure P inside the experimental cell, or the pressure difference ΔP across the membrane are thus equivalent in the remainder of this thesis. Pressure sweeps were conducted at constant temperature while monitoring the mass flow rate $Q_{m,exp}$. An example of pressure sweep at a fixed temperature of 3 K is shown in Fig. 4–5. In the absence of a pressure difference, the mass flow rate should go to zero. However, a spurious signal is detected in the mass flow spectrometer even when the pressure difference across the nanopore vanishes, $\Delta P \to 0$. This likely arises from evaporation at the walls of the pore, or from an offset in the mass spectrometer. To determine this offset, the data were fitted with a modified equation for viscous flow in a short pipe,

$$Q_m(P,T) = \frac{8\pi\eta L}{\tilde{\alpha}}\left(\sqrt{1+\frac{\tilde{\alpha}\rho R^4}{32\eta^2 L^2}P}-1\right)+\tilde{Q}_m, \tag{4.3}$$

where the last term was added here to account for the spurious signal as $\Delta P \to 0$. The free parameters in Eq. (4.3) are the radius R, the length L, a mass flow offset $\tilde{Q}_m$, and $\tilde{\alpha}$ which is a geometry-dependent factor accounting for the acceleration of the fluid at the nanopore's inlet. The temperature dependence of Q_m is implicitly

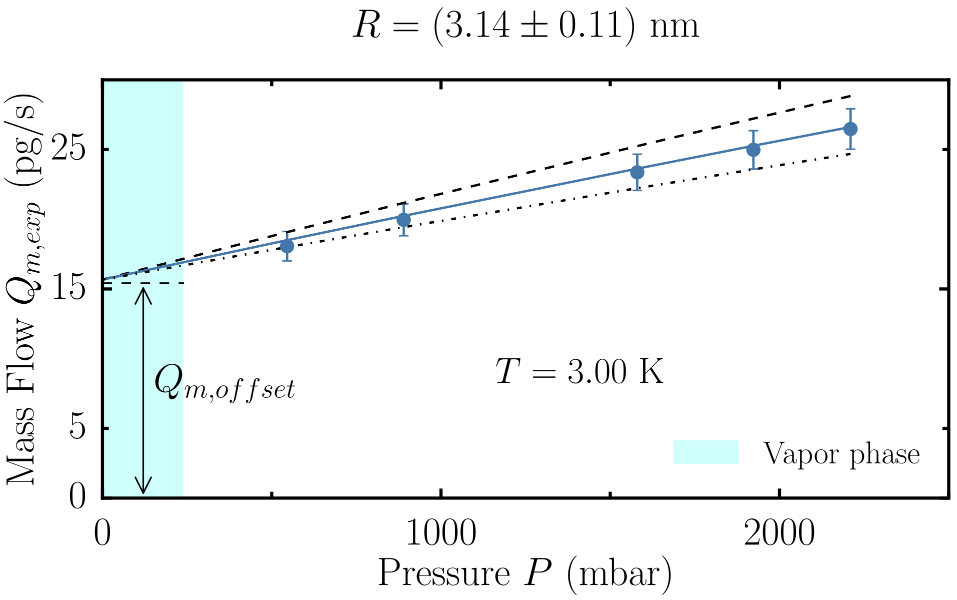

Figure 4–5: Mass flow measurements as a function of pressure in the normal phase at $T = 3$ K. The blue line is a fit of the data using Eq. (4.3). The value of the radius extracted from the fit is $R^{\mathrm{HeI}} = 3.14 \pm 0.11$ nm. The other fit parameters were found to be $L = 30$ nm, $\tilde{Q}_m = Q_{m,offset} = 15.77$ pg/s and $\tilde{\alpha} = 2$. The dashed and dash-dotted lines are obtained using Eq. (4.3) with the same fitting parameters than that of the blue line except for the radius. The radii associated to the dashed and dash-dotted lines correspond to $R^{\mathrm{HeI}} \pm \Delta R$, with $\Delta R = 0.11$ nm. The finite intercept at zero pressure $\tilde{Q}_m = Q_{m,offset}$ is a spurious signal (see text). The shaded area in the lower pressure range represent the vapor phase of ^{4}He. Its upper boundary on the abscissa is the saturated vapor pressure at 3 K.

contained in the tabulated values of the viscosity η and the density ρ [13][4]. These parameters are evaluated here at fixed temperature. Across the pressure range of

---

[4] The density $\rho(T, P)$ and viscosity $\eta(T, P)$ of ^{4}He on both sides of the superfluid transition are interpolated from experimental data [13–15] using *Python 2.7 Scipy* package [16]. The open-source code is publicly available on GitHub `https://github.com/Bachibouzouk/liquid-helium-physical-properties-interpolator`.

interest in Fig. 4–5, the density and viscosity vary almost linearly with P and they are bound by a 3% and 10% variation, respectively. The best-fit values of the free parameters were determined using a least squares method $\sum(Q_m - Q_{m,exp})^2$ evaluating the difference between the theoretical value Q_m and the experimental one, $Q_{m,exp}$. This fitting procedure was conducted over a hypercube in the parameter space of $(R, L, \tilde{Q}_m, \tilde{\alpha})$ in order to find a global minimum in the difference. The solid line displayed in Fig. 4–5 is a fit of Eq. (4.3) to the data with a radius of $R^{\mathrm{HeI}} = 3.14 \pm 0.11$ nm. This value is in excellent agreement with the one determined independently via the Knudsen effusion technique discussed above. Importantly, it demonstrates *de facto* that our experiment can quantitatively determine the mass flow near the superfluid transition in very small channels.

It is interesting to note that since ρ and η are nearly constant in the normal phase, the influence of the $\tilde{\alpha}$ parameter becomes negligible at sufficiently small values of R, *i.e.*,

$$\frac{8\pi\eta L}{\tilde{\alpha}}\left(\sqrt{1+\frac{\tilde{\alpha}\rho R^4}{32\eta^2 L^2}P}-1\right) \simeq \frac{8\pi\eta L}{\tilde{\alpha}}\left(1+\frac{\tilde{\alpha}\rho R^4}{64\eta^2 L^2}P-1\right) = \frac{\pi\rho R^4}{8\eta L}P.$$

This was indeed the case for this nanopore. Changes in Q_m arising from a variation of $\tilde{\alpha}$ between 1 and 10 were found to be negligible, and so the exact value of $\tilde{\alpha}$ had little or no influence on the determination of the radius R.

The mass flow model used in this section is based on the assumption that a nanopore shape can be approximated as a cylinder. Tomographic imaging by other groups showed the shape of similar size nanopores to be closer to a Laval nozzle [17]. To correct the model for a Laval nozzle geometry would require a tomographic image of the nanopore, an image that was not available to us. Nevertheless, since the cylindrical model fitted the data well and since the fitted value for the radius was found to be in good agreement with the value extracted from the Knudsen effusion, most likely this correction is small. Therefore, we approximated all pores to have a cylindrical geometry in the remainder of this thesis. Another assumption was that the ^{4}He is in its liquid phase along the whole channel, *i.e.* the liquid-gas interface is located on the low pressure side. A model for mass flow with liquid-gas interface located inside the channel was tested with recent ^{4}He mass flow measurements performed by the group of Prof. Taborek in long ($L \simeq 20$ μm) capillary channels [18]. They found that the liquid-gas interface was very close to the low pressure side. In this model, the pressure drop across the pore is equal to $\Delta P = P_{inlet} - P_{int} + \frac{2\gamma}{R_c}$. P_{int} is the pressure in the gas a few mean-free-path from the liquid-gas interface. Its value is expected by the authors of Ref. [18] to be to close to SVP$\simeq$ 240 mbar at $T = 3$ K. The factor $\frac{2\gamma}{R_c}$ is the Laplace pressure, proportional to the ratio of the surface tension, γ, and the radius of curvature of the interface, R_c. The radius of curvature cannot be smaller than the radius of the pore R, which provides and upper bound on the Laplace pressure at $\frac{2\gamma}{R} \simeq 1400$ mbar at $T = 3$ K. Both R_c and P_{int} are unknown, however, their effect is similar to a pressure offset $\tilde{P}$ on the Langhaar model, *i.e.*

$$Q_m(P,T) = \frac{8\pi\eta L}{\tilde{\alpha}}\left(\sqrt{1+\frac{\tilde{\alpha}\rho R^4}{32\eta^2 L^2}(P+\tilde{P})}-1\right). \tag{4.4}$$

A fit of Eq. (4.4) on the experimental data with a radius $R = 3.14$ nm and a length $L = 30$ nm yields a value of $\tilde{P} = 3026$ mbar, which is more than a factor 2 larger than the upper bound on $\tilde{P} \leq \frac{2\gamma}{R} \simeq 1400$ mbar. A fit with a fixed value of $\tilde{P}$ lower than 3026 mbar requires lower values of both L and R. Fitting Eq. 4.4 to the experimental data with parameters $R \in [2,5]$ nm, $L \in [10,30]$ nm, $\tilde{P} \in [0,1400]$ mbar and $\tilde{\alpha} \in [0.1,20]$ did not yield better fits as with Eq. (4.3), shown in Fig. 4–5. The offest due the Laplace pressure (4.4) can be partially accounted for by $\tilde{Q}_m$

in Eq. (4.3). However, if $\tilde{P}$ is large, then $\tilde{\alpha}$ is not negligible anymore. Thus, Eq. (4.4) has five fitting parameters $(R, L, P_{int}, R_c, \tilde{\alpha})$ whereas Eq. (4.3) has only three $(R, L, \tilde{Q}_m)$, as the effect of $\tilde{\alpha}$ can be neglected. Based on the last points, and in regard of the excellent agreement with the radius determined via Knusden effusion, it was decided to keep Eq. (4.3) as the fitting model of our experimental data in the normal phase of liquid ^{4}He. In the superfluid phase, due to the sharp decrease of the viscosity, the pore is expected to be completely filled with liquid.

4.1.3 Mass flow in the superfluid phase

Subsequent to the two independent *in situ* determinations of the nanopore's radius, the mass flow was measured as a function of temperature across the superfluid phase transition T_λ, and at several constant pressures. These data are displayed in Fig. 4–6 with the mass flow offset $Q_{m,offset}$ previously discussed in section 4.1.2 subtracted. An important feature of the flow data not previously observed in larger pores is the extremely weak pressure dependence below T_λ. The increase of pressure difference by a factor 15 only enhances the flow by 10–30 percent for temperatures below the superfluid transition. This independence of the mass flow upon a pressure gradient is expected in the case of a purely superfluid flow [19].

Previous work in Vycor®[5] observed the onset of the superfluid transition temperature at 1.95 K, lower than T_λ [20]. However, the superfluid transition in our pore is observed, to within our experimental accuracy, at a temperature very close to the bulk transition temperature, *i.e.* 2.17 K. This is not surprising since we measure the total conductance of the nanopore *and* of the source reservoir in series. Therefore, the onset of superfluidity in the bulk is first observed at T_λ and we expect the onset of the superfluid transition inside the pore to appear as a kink in the superfluid flow at a temperature slightly lower than T_λ. Unfortunately, it was not observed in our experiment due to the uncertainty in the mass flow near T_λ.

---

[5] Vycor® is a porous glass material with pores' sizes typically ranging between 5 and 10 nm diameter [20].

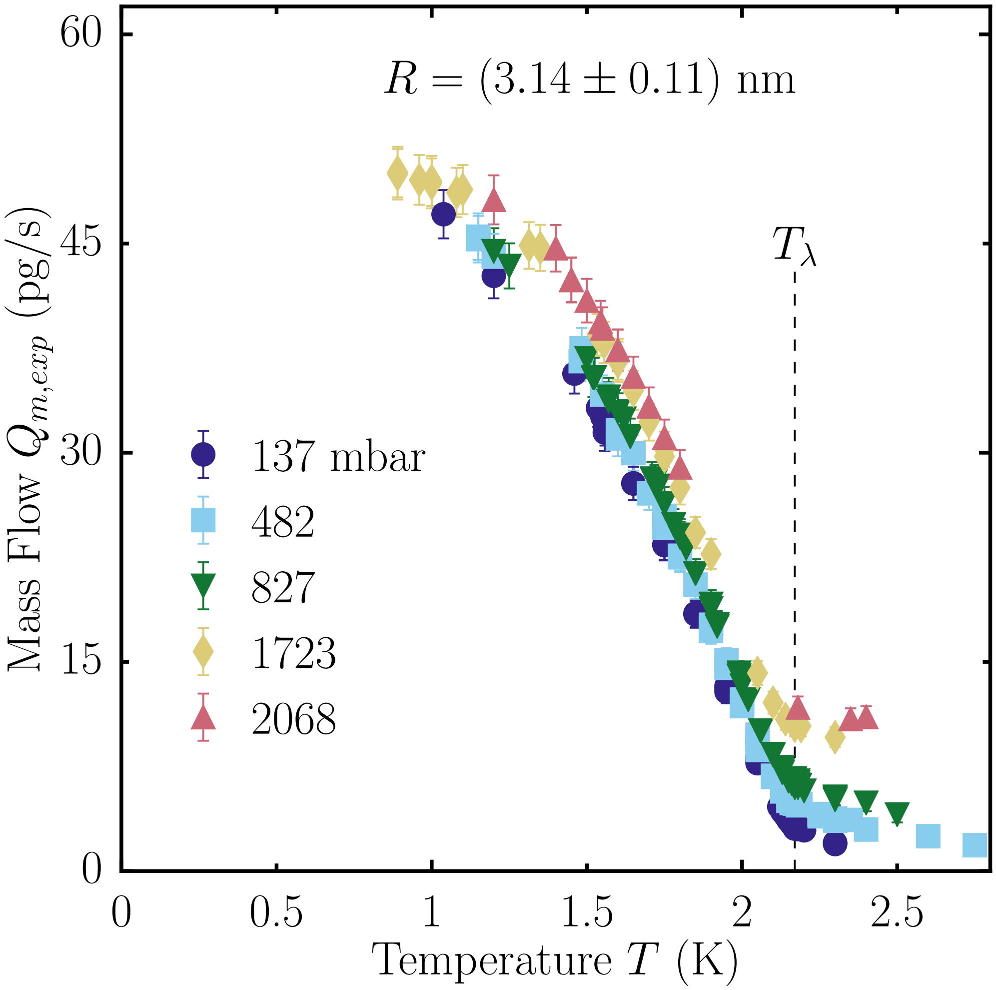

Figure 4–6: Temperature dependence of the mass flow measured at various pressures in the 3.14 nm radius pore. The offset $Q_{m,offset}$ introduced in 4.1.2 has been subtracted for each dataset. The vertical dashed line shows the bulk superfluid transition temperature T_λ at SVP.

In Fig. 4–7, the normal and superfluid mass flow from Figs. 4–5 and 4–6 are compared with measurements performed in a 7.81 nm radius and 30 nm long pore. Remarkably, the pressure dependence of the mass flow is strongly weakened in the smaller pore.

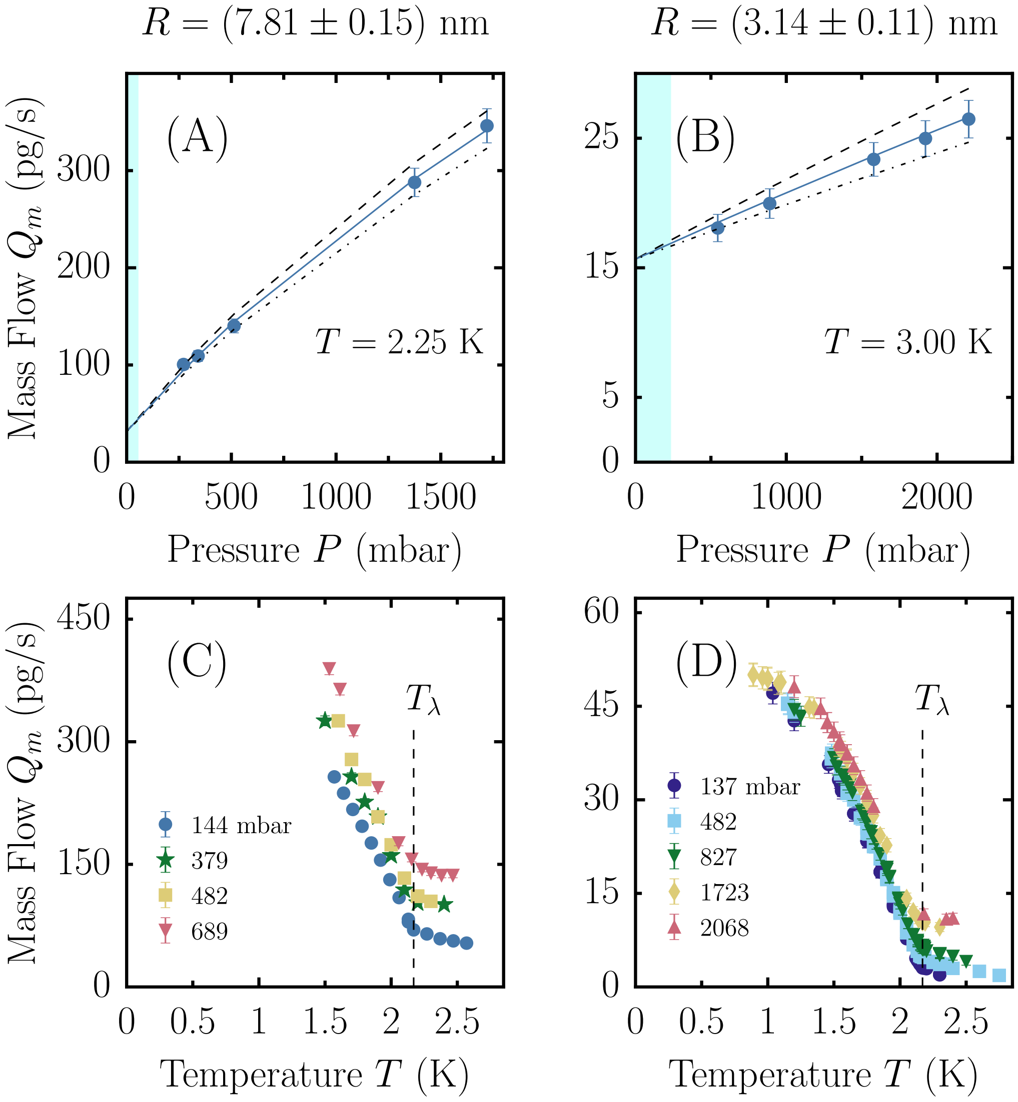

Figure 4–7: Normal fluid mass flow measurements at constant temperature as a function of pressure for a 7.81 nm **(A)** and a 3.14 nm **(B)** pore radius in the normal state. The panel (B) was presented in Fig. 4–5. The blue line is a fit of Eq. (4.3) to the data and the dashed and dash-dotted lines are one standard variation from the mean value for the radius, with all other parameters in Eq. (4.3) kept constant. The shaded area in the lower pressure range represent the vapor phase of ^{4}He. **(C)** and **(D)**, temperature dependence of the superfluid mass flow at several pressures as in Fig. 4–6. The vertical dashed line shows the bulk superfluid transition temperature T_λ at SVP. *Source*: [1].

Using the data taken during temperature sweeps at fixed pressures and shown in Fig. 4–6, we can reconstruct various pressure dependences of the mass flow at fixed temperatures and compare them with predictions from the normal flow model described in Eq. (4.3). The data and the model are displayed in Fig. 4–8 (A) and (B), respectively.

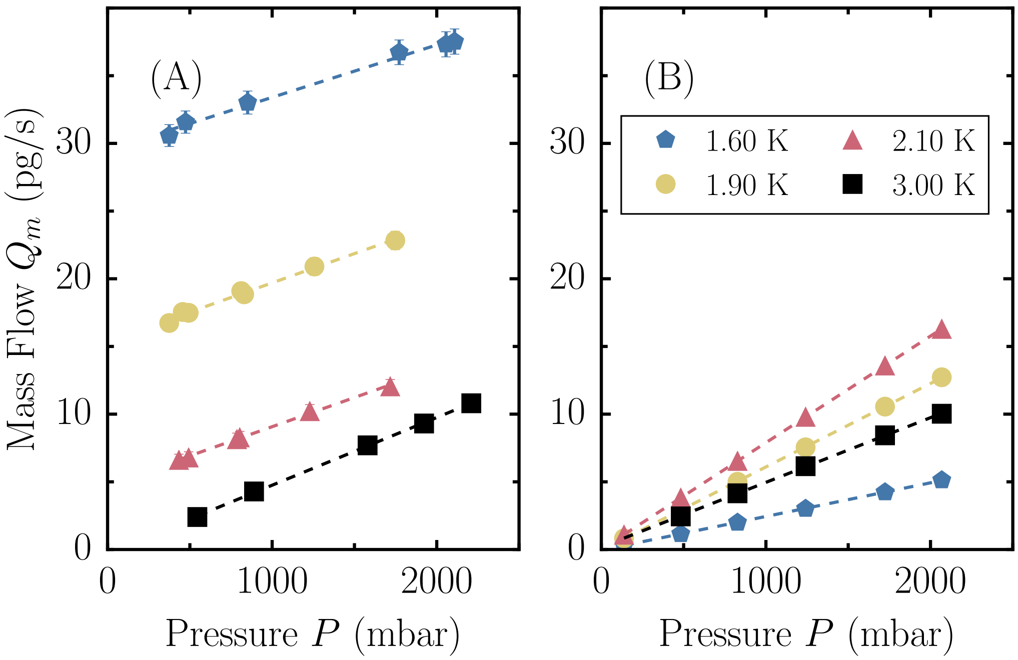

Figure 4–8: Pressure dependence of the mass flow at various fixed temperatures. **(A)** The experimental pressure dependences reconstructed from the temperature sweeps data, except for the black squares which are from the pressure sweep at 3 K (*cf.* Fig. 4–5). The offset $Q_{m,offset}$ introduced in 4.1.2 has been subtracted for each dataset. The dashed lines are linear fits to the displayed datasets. **(B)** The pressure dependences predicted by Eq. (4.3), model for the normal flow. The parameter values used here are described in the main text. The dashed lines are also linear fits. Note that the datasets in (A) correspond to the total mass flow, whereas the ones in (B) correspond only to the normal part of the flow. The values of the fits' slopes are compared in Fig. 4–9 for additional fixed temperatures, not displayed here for the sake of readability.

Because the radius determinations by Knudsen effusion before and after the superfluid measurements are in close agreement (*cf.* Fig. 4–4), we can assume that both radius and length of the nanopore are constants. Thus, the model's parameters used in Fig. 4–8 (B) are the ones extracted from the fit of the model for the 3 K pressure sweep data discussed in section 4.1.2, *i.e.* $R = 3.14$ nm, $L = 30$ nm and $\tilde{\alpha} = 2$. As the value of the parameter $\tilde{Q}_m$ has no influence on the slopes of the pressure dependences, it was set to zero in the curves shown in Fig. 4–8 (B). At temperatures below the superfluid transition, the mass flow is constituted of a normal and a superfluid component. Thus, the density ρ in Eq. (4.3) was replaced by the normal component's density, ρ_n (see Eq. (2.26)). Since previously measured pure superfluid flow was found to be pressure independent [19], we tentatively attribute the pressure dependence of the observed mass flow below the superfluid transition to the normal component. When looking at the pressure dependence of the data, we notice that its pressure dependence becomes gradually weaker as the temperature decreases. In contrast, the model's pressure dependence becomes stronger at first in the vicinity of T_λ, before getting weaker and similar to the observed dependence on the data at lower temperatures. For the lowest temperature of 1.6 K, the model predicts even a weaker pressure dependence than what is observed. These observations are illustrated via a linear fit of the mass flow versus pressure. The slopes of the fits on the data and the model's pressure dependences are shown in Fig. 4–9. In the vicinity of the superfluid transition temperature, the slope of the pressure dependence predicted by the normal flow model is up to twice as large than the observed one, whereas above the transition and below 1.8 K the slopes' values are comparable. Hence, the data displayed in Fig. 4–9 clearly show the failure of the model to predict the right pressure dependences very close to T_λ.

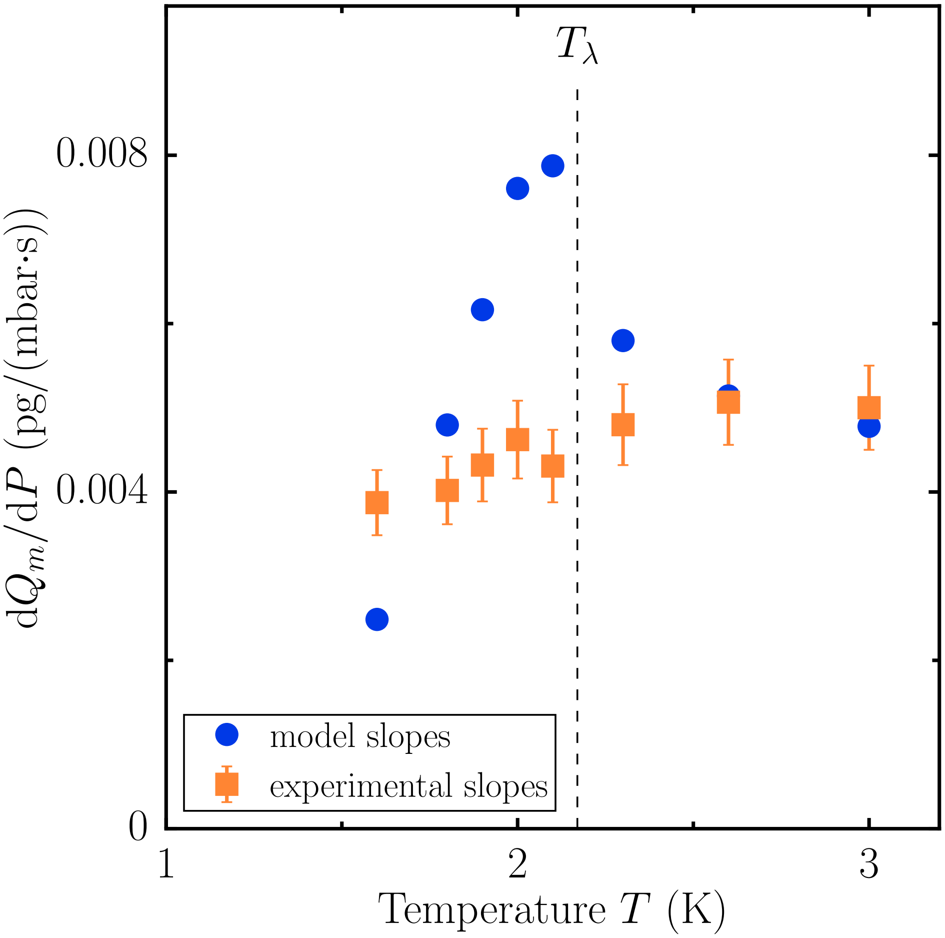

Figure 4–9: Slopes of the linear fits to the experimental and modeled pressure dependences illustrated by the dashed lines in Figs. 4–8 **(A)** and **(B)**, respectively. The vertical dashed line shows the bulk superfluid transition temperature T_λ at SVP.

4.1.4 Relevant length scales

Now that we have characterized the nanopore radius R and its length[6] L, it is imperative to perform a comparative analysis of all possible relevant length scales to determine the effective dimensionality of the nanopore. Unlike superconductors or superfluid ^{3}He which undergo BCS pairing, ^{4}He has a very small coherence length on the Angstrom scale, *i.e.* $\xi_4(T) \simeq \xi_0(1 - T/T_\lambda)^{-\nu}$ with $\xi_0 \simeq (3.45 \pm 0.05) \cdot 10^{-10}$ m [21] and $\nu \approx 2/3$ is the correlation length universal critical exponent [21, 22]. For example, $\xi_4 \sim 0.4$–2 nm in the temperature range $T \simeq 0.5$–2 K. In this temperature range, the pore radius R can also be compared to the thermal de Broglie wavelength, $\Lambda(T) = \sqrt{2\pi\hbar^2/m_4 k_\mathrm{B} T} \sim 1$ nm and with the thermal length $L_T = \hbar c_1/k_B T \sim 1$ nm, where $c_1 \simeq 235$ m/s is the first sound velocity of ^{4}He.

Another estimate regarding the effective dimensionality can be made by considering ^{4}He atoms confined inside a long cylinder of radius R with hard walls. In analogy with electrons confined in quantum wires, we compute the energy needed to populate excited single particle transverse modes. In order to fill the lowest excited transverse angular momentum state for a single ^{4}He atom, a temperature $T \sim \Delta_\perp/k_\mathrm{B} \simeq 3.5/R^2\ \mathrm{nm}^2 \cdot \mathrm{K} \sim 0.4$ K for $R = 3$ nm is needed. These estimates, which neglect interaction effects, would place our flow experiments in a mesoscopic regime, whereby confinement length scales and energy scales are on the order of the intrinsic ones.

---

[6] Our nanopores lengths are known from the thickness of the membrane through which they were drilled.

4.1.5 Critical velocity

Considering only the mass flow data below T_λ, we can extract the superfluid velocities using the two-fluid model proposed by Landau and Tisza (see Eq. (2.27)) and the relation between the mass current density $\vec{J}_{\text{tot}}$ and the mass flow $Q_{m,\text{tot}}$,

$$Q_{m,\text{tot}} \equiv \int_A \vec{J}_{\text{tot}} \cdot \mathrm{d}\vec{a} = \int_A (\rho_n \vec{v}_n + \rho_s \vec{v}_s) \cdot \mathrm{d}\vec{a} = Q_{m,n} + \rho_s v_s \pi R^2. \tag{4.5}$$

In the last step above, we assume the superfluid velocity field being (i) homogeneous in space and (ii) along the axis of the nanopore. Here, $Q_{m,n}$ is the normal flow of ^{4}He which is still present down to temperatures to approximately 1 K. It is modeled in Eq. (4.3), by replacing ρ by ρ_n. Subtracting $Q_{m,n}$ from the total mass flow yields the superfluid fraction of the flow, whereby the velocity is given by

$$v_s = (Q_{m,\text{tot}} - Q_{m,n})/(\rho_s \pi R^2). \tag{4.6}$$

In this analysis, we use the *in situ* determination of the radius R described in previous subsection 4.1.2, *i.e* 3.14 ± 0.11 nm. We also assumed the superfluid density ρ_s is that of the bulk for the ^{4}He inside the pore. It would be desirable to independently measure ρ_s, however this is not yet possible in our flow experiment. In the remainder of this thesis, ρ_s will always refer to the superfluid density taken from the bulk. Finally, as in the previous literature dating since the 1930's, we assume that the superfluid is always reaching the critical velocity, *i.e.* $v_s = v_c$. The superfluid velocities are thus limited due to dissipation mechanisms, as previously discussed in subsection 2.4.3. In the remainder of this thesis, v_s and v_c will be equivalent.

4.1.5.1 Pressure dependence of the critical velocities

When the constant $Q_{m,offset}$ is used as the parameter $\tilde{Q}_m$ in Eq. (4.3), the model underestimates the normal mass flow above the transition temperature for the low pressures datasets in Fig. 4–6. Conversely, it overestimates it for the high pressure ones. At low pressure (below 500 mbar), the underestimation results in large critical velocities near the transition temperature, in a region where the normal flow still has a strong influence within the two fluid model. For the high pressure datasets (above 1.5 bar), the subtraction of the normal flow can even result in unphysical negative critical velocities close to the transition temperature because the model predicts larger flow than the measured ones. To correct for a potential pressure dependence of $\tilde{Q}_m$, a pressure dependent quantity $\delta\tilde{Q}_m(P)$ is added to $Q_{m,offset}$. The $\delta\tilde{Q}_m$ are determined for each fixed pressure dataset by a fit of Eq. (4.3) with fixed radius $R = 3.14$ nm and $L = 30$ nm to the data taken above T_λ. In the following of this chapter, the critical velocities are computed using these two routes, by using either (i) $\tilde{Q}_m = Q_{m,offset}$ or (ii) $\tilde{Q}_m = Q_{m,offset} + \delta\tilde{Q}_m(P)$ in Eq. (4.3). The mass flow datasets at fixed pressure 137 and 1723 mbar and the models based on the two routes (i) and (ii) are shown in Figs. 4–10 (A) and (B), respectively[7] . The surprising maximum in the normal mass flow below T_λ arises from the temperature dependence of the liquid ^{4}He viscosity which decreases by a factor of two across the transition, thus leading to an increase of the flow. This increase is then countered and suppressed by ρ_n which greatly decreases with the temperature. The critical velocities extracted from the two aforementioned mass flow datasets are displayed in Figs. 4–10 (C) and (D). The values of $\delta\tilde{Q}_m(P)$ used in route (ii) are summarized in Tab. 4–1. The resulting critical velocities extracted for all fixed pressure datasets following routes (i) and (ii) are displayed as a function of temperature in Figs. 4–11 and 4–12, respectively.

---

[7] The fits for the other pressures are shown in Appendix E.

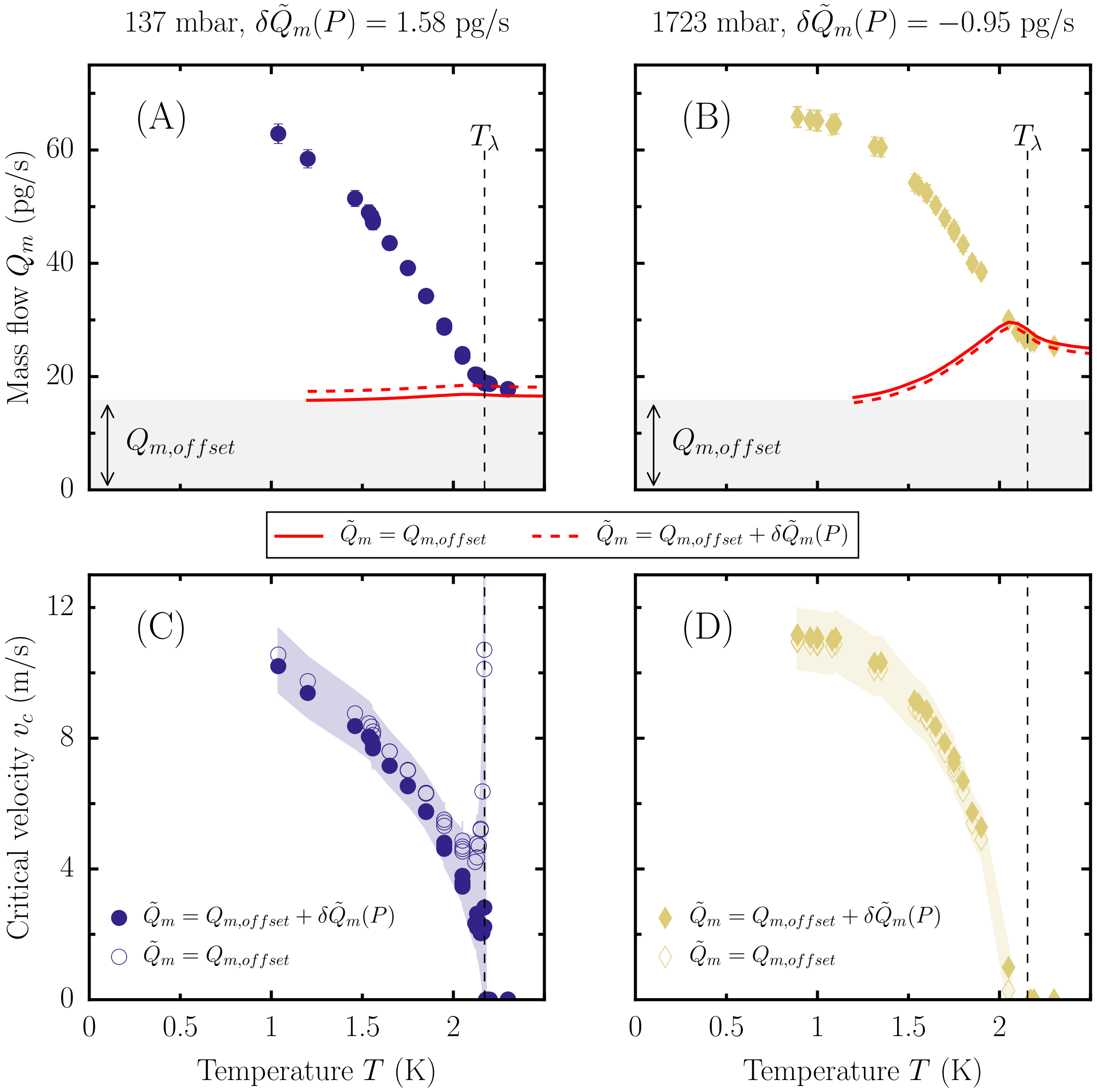

Figure 4–10: Critical velocities from the mass flow measured at various fixed pressures in the 3.14 nm radius pore. Vertical axes are shared for sub-figures in the same row, and horizontal ones are shared for sub-figures in the same column. **(A)-(B)** Mass flow as a function of temperature for the 137 and 1723 mbar fixed pressure, respectively. The solid and dashed red lines correspond to the model in Eq. (4.3) with $\tilde{Q}_m = Q_{m,offset}$ and $\tilde{Q}_m = Q_{m,offset} + \delta\tilde{Q}_m(P)$, respectively. The grey shaded area is a visual representation of $Q_{m,offset}$ which was not subtracted from the datasets here. **(C)-(D)** Critical velocities extracted using Eq. (4.6) and Eq. (4.3) with $\tilde{Q}_m = Q_{m,offset}$ (open symbols) or $\tilde{Q}_m = Q_{m,offset} + \delta\tilde{Q}_m(P)$ (filled symbols). The colored shaded areas represent a confidence interval accounting for the experimental and fitting uncertainties. The vertical dashed line shows the bulk superfluid transition temperature T_λ at SVP.

P (mbar)	137	482	827	1723	2068
$\delta\tilde{Q}_m$ (pg/s)	1.58	0.47	0.16	-0.95	-1.10

Table 4–1: Values of the $\delta\tilde{Q}_m(P)$ used to make the normal flow model parameter $\tilde{Q}_m$ pressure dependent. They are determined by the difference of $Q_{m,offset}$ and $\tilde{Q}_m(P)$. $Q_{m,offset}$ is determined by the fit of the normal flow model in Eq. (4.3) on pressure sweep data at fixed temperature above T_λ, shown in Fig. 4–5. $\tilde{Q}_m(P)$ are extracted for each fixed pressure from a fit of Eq. (4.3) on the temperature sweep data. The data used in the fit are restricted to temperatures above T_λ.

The critical velocities obtained through route (*i*) display large variations near T_λ in Fig. 4–11. In this case, the pressure dependence of the critical velocities is extremely weak below 1.9 K. We note that the higher pressure sets have lower critical velocities than the lower pressure ones in the range (1.7 K – T_λ). Below approximatively 1.7 K, this pressure dependence is inversed. We do not interpret this as a regime transition, but rather as arising from systematic errors made in the modeling of the normal flow component. Indeed, changing the value of $\tilde{Q}_m$ would shift the temperature at which this change of pressure dependence is observed. The critical velocities obtained through route (*ii*), and shown in Fig. 4–12, display no significant pressure dependence in the (1.8 K – T_λ) range compared to route (*i*). Below 1.8 K, the critical velocities exhibit a larger spread between different pressure sets than the ones extracted through route (*i*). The route (*i*) shows better agreement with previous experimental results highlighting the pressure independence of the superfluid velocity at low temperature, where the normal flow is vanishing [19]. However, in the case of route (*ii*), the superfluid velocities vanish at the transition, which is expected for the two-fluid model when $\rho_s \rightarrow 0$. The values of critical velocities obtained via the two routes thus provide a confidence interval for the critical velocities extracted from the mass flow measurements. This confidence interval reflects the systematic error in the determination of $\tilde{Q}_m$.

The critical velocities below 1.95 K are less dramatically affected by the route used to subtract the normal flow component. This is because the normal component density ρ_n decreases rapidly with the temperature and thus the percentage of the total mass flow in the normal phase decreases as well, leading towards a pure superfluid flow around 1 K. Moreover, by excluding data in the vicinity of T_λ in our analysis, we also minimize the systematic error arising as previously discussed in section 4.1.3. In next section, we will therefore only discuss critical velocities at temperatures below 1.95K.

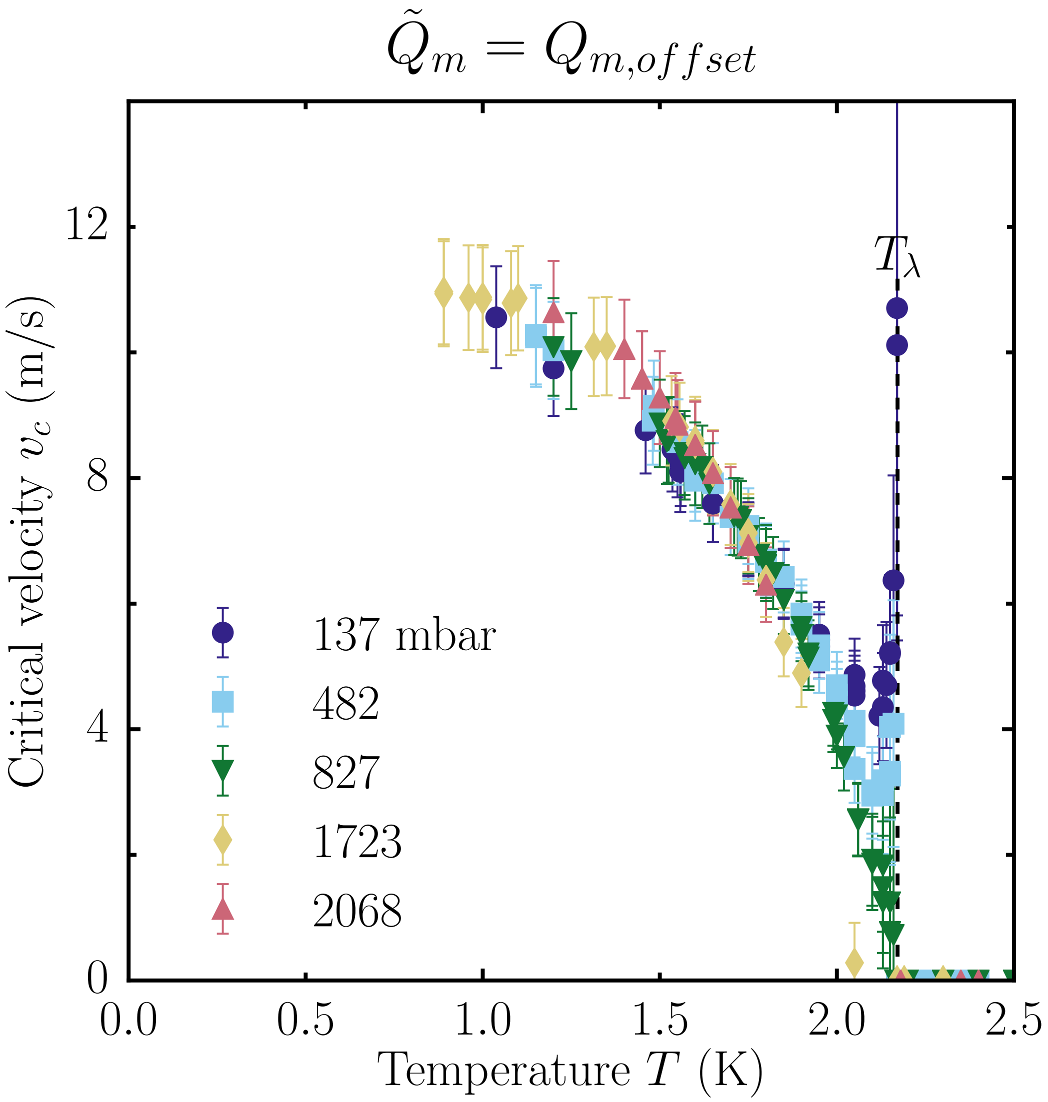

Figure 4–11: Critical velocities computed by subtracting the normal flow component modeled by Eq. (4.3) with a constant $\tilde{Q}_m$ parameter. The vertical dashed line shows the bulk superfluid transition temperature T_λ at SVP.

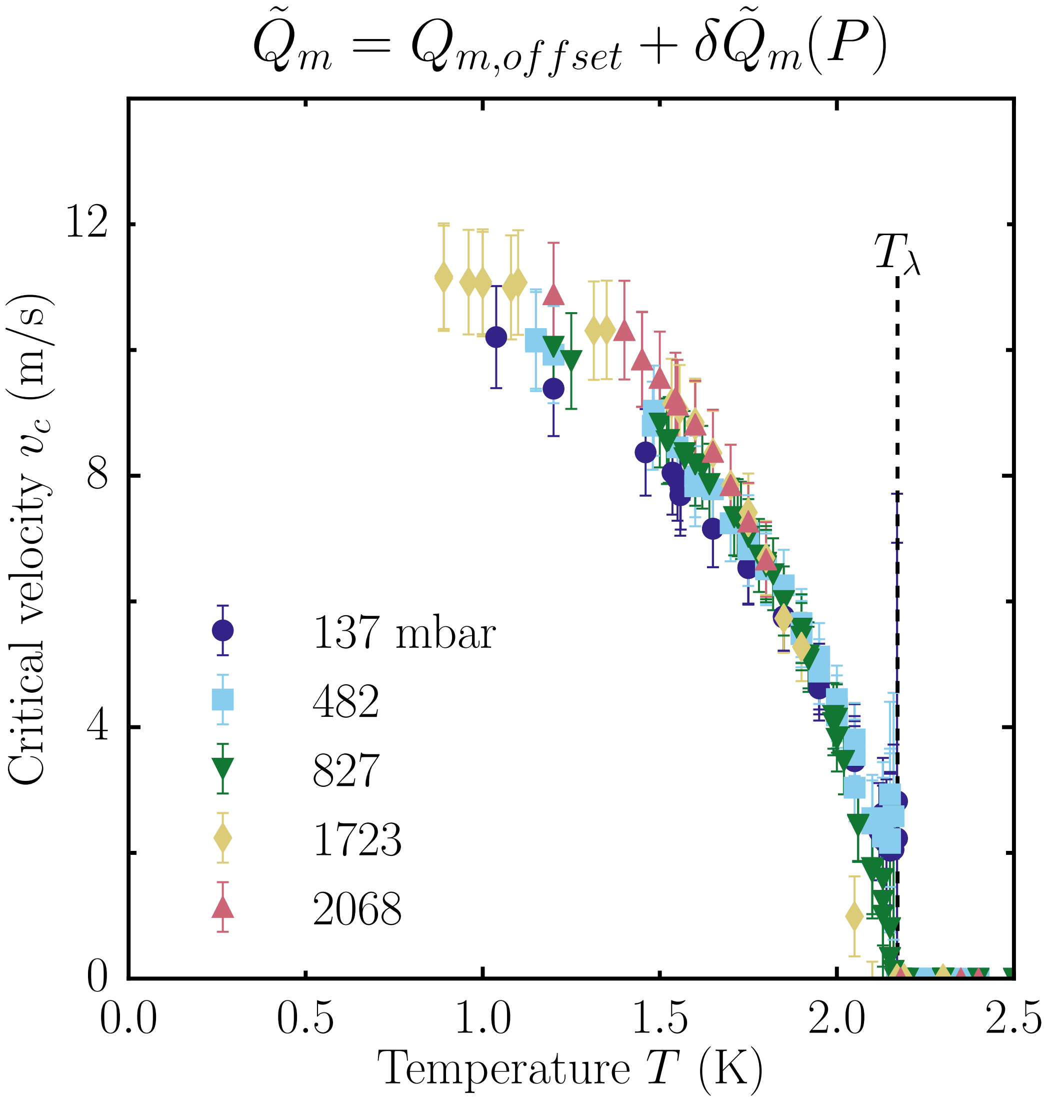

Figure 4–12: Critical velocities computed by subtracting the normal flow component modeled by Eq. (4.3) with a pressure dependent $\tilde{Q}_m$ parameter. The pressure dependent deviations from $\tilde{Q}_m = Q_{m,offset}$, $\delta\tilde{Q}_m$, are listed in Tab. 4–1. The vertical dashed line shows the bulk superfluid transition temperature T_λ at SVP.

4.1.5.2 Temperature dependence of the critical velocities

The extracted superfluid critical velocities are shown as a function of reduced temperature, $t \equiv 1 - T/T_\lambda$, in Fig. 4–13 for two lower pressure datasets.

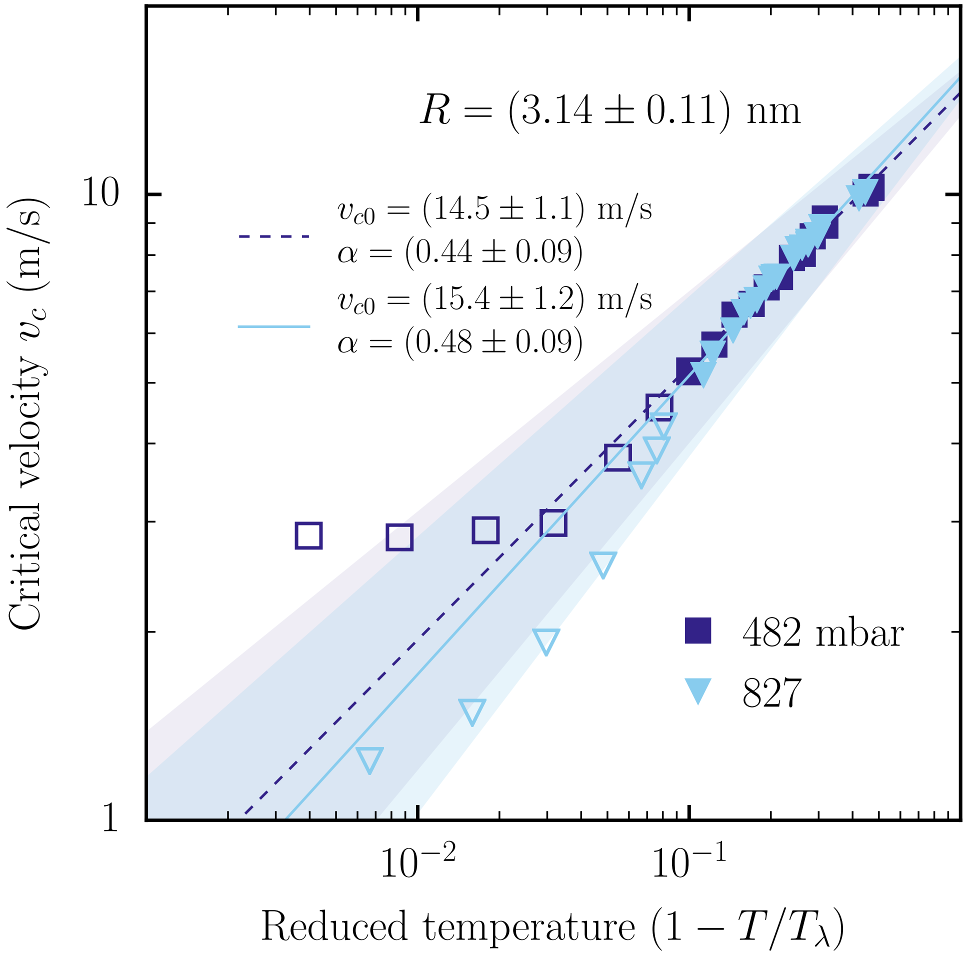

Figure 4–13: Log-log plot of the superfluid critical velocity versus the reduced temperature $t \equiv 1 - T/T_\lambda$ for the 3.14 nm pore data. The filled symbols indicate the data used for the power law fit of the data taken at pressure of 482 (dashed line) and 827 (solid line) mbar. The power law relation used in the fit follows Eq. (4.8). The data at low reduced temperature, *i.e.* close to T_λ, is very sensitive to uncertainty on $Q_{m,\mathrm{tot}}$ because ρ_s is nearly zero. The power law is graphed by the dashed lines with color corresponding to each pressure dataset. The colored shaded areas show the maximum and minimum uncertainties for all combinations of the power law fitting parameters.

Near the bulk superfluid transition, it is well-established that the superfluid density follows a universal power law form

$$\rho_s(t) = \rho_{s,0} t^{\nu}, \tag{4.7}$$

where ν is the correlation length's critical exponent found experimentally to be close to 2/3 [23]. Considering a slowly-varying quantum-mechanical wave function with a phase Φ, the kinetic energy of the superfluid is given by $\rho_s v_s^2/2 = \rho_s(\hbar^2/2m_4^2)|\vec{\nabla}\Phi|^2$. From scale invariance, we expect near T_λ the mean square of the superfluid velocity to scale with the correlation length $\xi_4(T)$ as $\overline{v_s^2} \sim 1/\xi_4(T)^2 \sim t^{2\nu}$. In fact, this result is only valid at temperatures very close T_λ, *i.e* for $t \lesssim 0.1$. From this hyperscaling analysis, there is *a priori* no reason to expect a power law behavior in the superfluid velocity over a wide range of temperatures away from T_λ.

However, the data shown in Fig. 4–13, *appear* to follow a power law of the form

$$v_c(t) = v_{c0} t^{\alpha}, \tag{4.8}$$

where v_{c0} is the superfluid critical velocity at $T = 0$ K. For our pore, the power law yields an exponent α equal to 0.44 ± 0.09 and 0.48 ± 0.09 for the 482 mbar and 827 mbar pressure datasets, respectively. Critical velocities extrapolated at zero temperature are $v_{c0} = 14.5 \pm 1.1$ m/s and $v_{c0} = 15.4 \pm 1.2$ m/s for both pressures, respectively.

In contrast, the superfluid velocities in a larger pore (7.81 nm radius), as shown in Fig. 4–14, display a significantly distinct exponent equal to 0.66 ± 0.05 and the zero-temperature extrapolated critical velocity is $v_{c0} = 30.1 \pm 2.4$ m/s. Other work in nanoporous material such as Vycor® reported in Ref. [20] found power law behavior close to the transition temperature with exponents close to the three-dimensional bulk value, *i.e.* $\nu \simeq 0.67$. While not a proof given the limited range in temperature explored, the appearance of a smaller non-universal exponent when the dimensionality is reduced is consistent with expectations from quantum hydrodynamics in 1D, whereby increased thermal and quantum fluctuations should prohibit long-range order. In that limit, it is expected for superfluidity to become governed by non-universal power laws as a function of the systems' details, such as pore length and size, rather than a universal critical exponent, as in the bulk case.

In the next section, experimental data for the superfluid flow will be compared with previous measurements conducted in larger single nanopores [2, 3]. This will allow us to highlight the quasi–one-dimensional behavior observed in the 3.14 nm pore. For the sake of readability, only the data extracted from route (i) will be used in the plots, however the confidence interval will be used for systematic uncertainties.

4.2 Comparison with previous studies

4.2.1 Critical velocity versus pore radius

The superfluid critical velocities extracted from measurements in larger single pores are displayed as a function of temperature in Fig. 4–14, together with the data presented in the previous section. As mentioned in section 4.1.3, the pressure dependence of the velocities in the smaller pore is weaker than for larger pores.

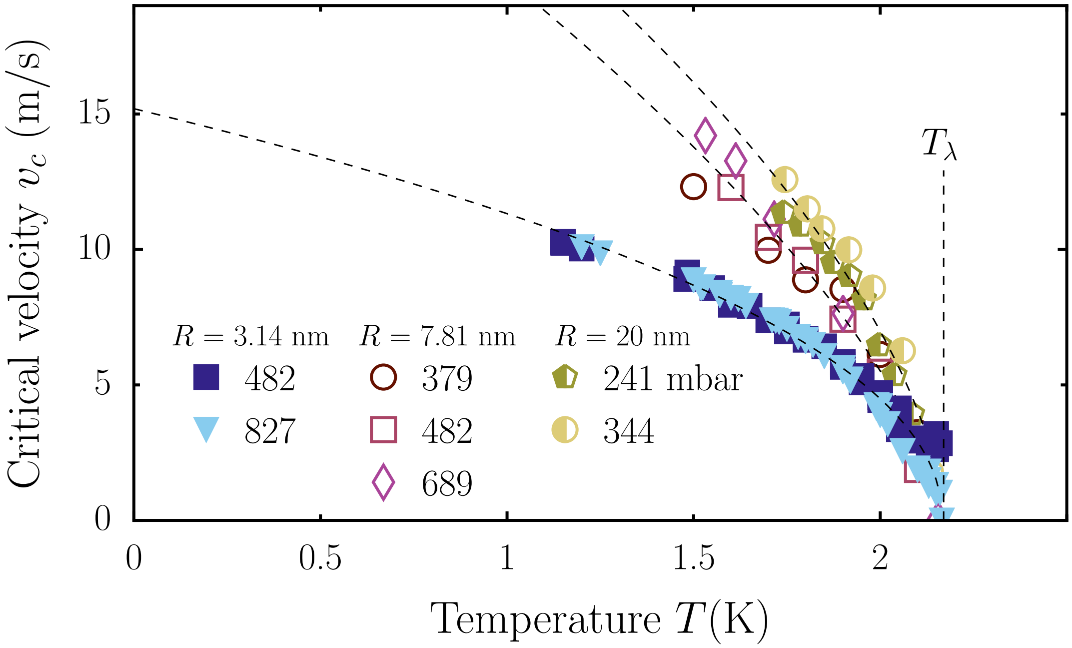

Figure 4–14: The superfluid critical velocities are shown at several pressures below 1 bar for three different nanopore radii. The filled symbols refer to the 3.14 nm pore, the open symbols to the 7.81 nm one and the half-filled symbols a 20 nm pore from a previous study [2]. The dashed lines are fits using the power law from Eq. (4.8). The thicknesses of the membranes for the 20 and 7.81 nm pores are 50 and 30 nm, respectively. *Source*: [1].

The larger pores have a smaller aspect ratio L/R and a relatively small length compared to the porous media used as superleaks to filter Helium II from Helium I [20]. This likely explains why the pressure dependence of the superfluid velocities is stronger in the larger pores, as the Helium I might be less efficiently filtered out over distances comparable to the membrane thickness and so it contributes more to the measured flow. An inspection by eye of the data plotted in Fig. 4–14 readily shows the superfluid velocities being smaller in the $R \simeq 3.14$ nm pore, at similar pressures and temperatures. Such suppression of the flow velocity as the radius is decreased is in stark contrast to the behavior described by Eq. (2.37), *i.e.* $v_{c,F} \simeq \frac{\kappa_0}{4\pi R} \ln(2R/a_0)$, predicted by Feynman, and observed in larger apertures and nanoporous materials [24]. To illustrate this last point, critical velocities from previous studies of superfluid flow through channels of sizes ranging from centimeters down to a few tens of nanometers are displayed in Fig. 4–15, together with the data from Fig. 4–14, and the predictions from the Feynman model.

From our data, it is clear that Feynman's model does not predict the correct trend of the critical velocity at the nanometric scale. This early model of dissipations in superfluid flow via production of vortices does not address either the rate at which those are produced. Anderson [27] proposed, in analogy with the Josephson effect in superconductors, that a steady state non-entropic flow may be achieved at a critical velocity v_c via a mechanism that unwinds the phase of the order parameter in 2π quanta (*cf.* Eq. (2.25) from section 2.4.1). Such "phase slips" (or vortices) occur at a rate Γ, and correspond to a process for which the amplitude of the order parameter Φ would instantaneously be suppressed to zero at some point along the nanopore. This process can be driven either by thermal or quantum fluctuations. In the temperature range of our experiment, we however expect thermally-activated phase slips to dominate. Using a Gibbs–Duhem relation at constant temperature to convert a pressure to a chemical potential difference, energy conservation dictates that there must exist dissipation mechanisms in the nanopore occurring at a rate Γ

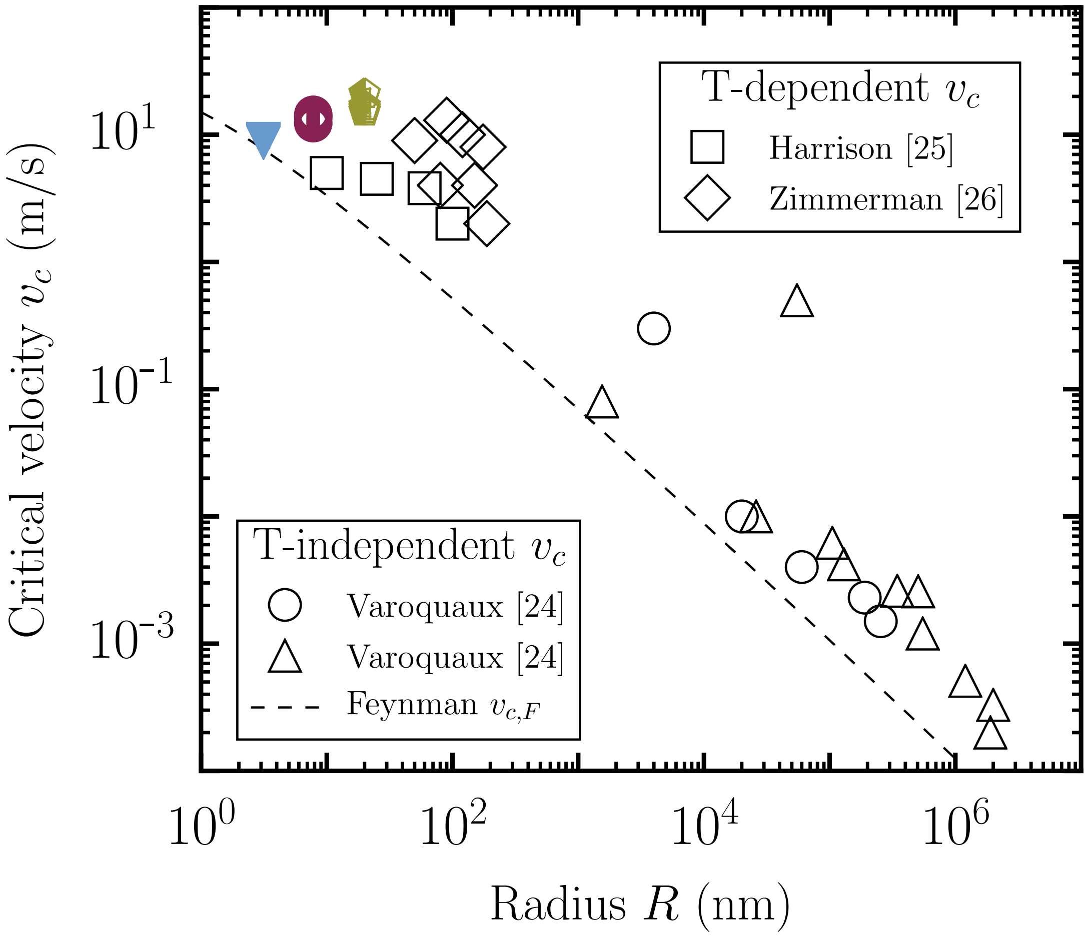

Figure 4–15: Critical velocities at temperature $T = 1.5$ K from Fig. 4–14 (color) are displayed alongside with critical velocities from various previous work (white squares, diamonds, circles and triangles) summarized by Varoquaux [24]. The squares and diamonds correspond to pressure driven AC flow experiments with circular nanopores in nanoporous 5 μm thick mica [25] and in ∼100 nm thick nickel foil [26], respectively. The circles represent a homogenous set of data and the triangles represent a heterogeneous set of data collected from various types of experiments (heat flow, oscillations) for which v_c was found independent of the temperature [24]. The outliers triangle data point at larger radius is a thin film experiment. The superfluid critical values are all quoted at 1.5 K, since earlier experiments were not performed at a lower temperature. The dashed line represents Feynman's critical velocity, described in Eq. (2.37).

given by

$$h\Gamma = \frac{m_4 \Delta P}{\rho_s} - \frac{1}{2} m_4 v_s^2. \tag{4.9}$$

Experimental estimates of Γ were first made by Trela and Fairbank [28], who found $\Gamma \sim 1$ Hz for superfluid flow through constrictions with $R \sim 10^{-4}$ m. Using Eq. (4.9) with our range of values for ΔP and v_s , we estimated that $\Gamma \sim$ 3–5 GHz, which is well below the flow rate of 7.5×10^{12} atoms/s measured in our smaller pore, yet approaching the quantum of mass flow given in natural units by $Q_0 = m_4^2/h \simeq 10^{10}$ atom/s at one bar differential pressure and fluid density taken at SVP.

In the next section, we will present very recent theoretical work regarding the dissipation rate in superfluid [4] that builds on previous seminal works of Langer and Fisher [29]. Strikingly, this new model accounts properly for the critical velocity as well as the temperature and nanopore size dependences found in our experiment.

4.2.2 Beyond the Feynman critical velocity

Feynman's prediction for superfluid critical velocity in confined geometries, Eq. (2.37), is based on the assumption that the nanopore radius R is much larger than the vortex core radius a_0, which he had arbitrarily estimated to be 0.4 nm, close to the ^{4}He atomic spacing [30]. Our smallest pore radius is only one order of magnitude larger than a_0. Thus, a change of regime as we approach this critical length scale seems plausible. Indeed, we indicated in previous section that the trend of our experimentally determined critical velocities, as the pore size decreases, contradicts Feynman's prediction. In this section, we will describe a new model which suggests that our smallest pore stands at the edge of a crossover region where dissipations are further enhanced with the decrease of the pore's size.

We begin by considering an early model of dissipation in the form of thermally-activated vortices [29]. The energy cost of a vortex creation along a superfluid flow, E_{tot}, is a balance between the condensation energy inside the core of the vortex, E_0, and the kinetic energy due to the circulation of superfluid around the vortex core,

$$E_{tot} = E_0 + \vec{p} \cdot \vec{v}_s. \tag{4.10}$$

Here, $\vec{p}$ is the momentum of the vortex and $\vec{v}_s$ is the superfluid velocity, both with respect to the rest frame. For ring vortices created within the flow through a long pore or *channel* (*i.e.* with an aspect ratio L/R of ten or more), it can be shown that E_{tot} is a function of the vortex radius r [4]. In the limit where $r/a_0 \gg 1$, Langer and Fisher [29] predicted the existence of a critical vortex radius r_c for which $E_{tot}(r_c)$ is a local maximum, as illustrated in Fig. 4–16. This critical radius arises from the creation of vortices. Vortices with a radius r larger than r_c will lower their energy by expanding further, whereas vortices with $r < r_c$, will tend to collapse.

Langer and Fisher assumed the height of the energy barrier to be $E_{max} \equiv E_{tot}(r_c)$, and that it can be used as an estimate for the free energy difference δF between a metastable state without vortices and a stable state with vortices. Restricting themselves to temperature-dependent critical flow velocities, they linked E_{max} directly to Γ, the rate of vortex creation inside the superfluid, *i.e* to phase slip events, with an Arrhenius law of the form

$$\Gamma \simeq \Gamma_0 e^{-\beta \delta F} = \Gamma_0 e^{-\beta E_{max}}, \tag{4.11}$$

where $\beta = 1/k_B T$ and Γ_0 is a rate, referred to as the *attempt rate* (or *attempt frequency*). Namely, Γ_0 corresponds to the phase space available for vortices excitations and depends on the vortex type as well as the temperature [4]. When the channel radius is such that $R < r_c$, the maximum size of a vortex ring is then constrained by the radius R of the channel. The energy barrier for their creation is thus lowered, leading to an *increase* in dissipation. It is interesting to note that their estimate of $r_c \simeq 3$ nm is *conspicuously the length scale of the smallest pore measured in this work*. The suppression of the experimental critical velocities as the pore radius decreases at $T = 1.5$ K, as shown in Fig. 4–15, can therefore be interpreted as a crossover to a regime where the flow is dominated by the physics inside the channel.

Building on the work of Langer and Fisher, recent theoretical work by Del Maestro and Rosenow quantitatively describes the critical velocity temperature and pore size dependence for two different pore geometries, *i.e.* a pinhole (orifice) and a cylindrical channel [4]. They determined the energy barrier E_{max} for thermally-activated creation of both line and ring vortices as a function of superfluid velocity v_s, pore radius R and a vortex geometric factor equal to $x \in [-R, R]$ for line vortices

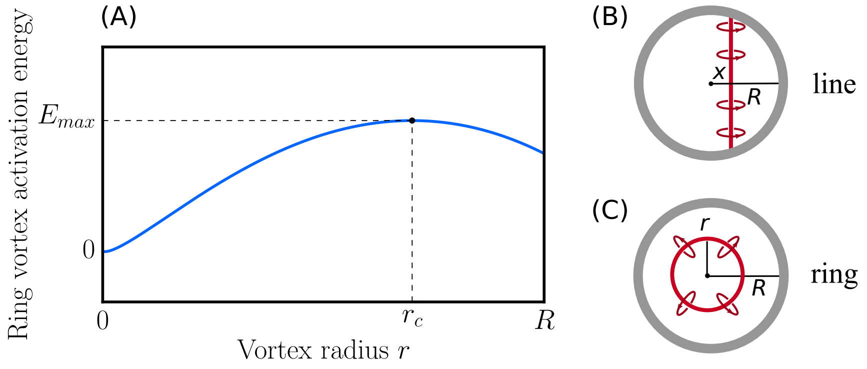

Figure 4–16: **(A)** Energy required for the thermal creation of a ring vortex inside flowing superfluid ^{4}He through a channel of radius R. The radius at which the energy is maximum, r_c, is special because vortex rings created with a radius $r < r_c$ will tend to collapse, whereas vortices with larger radii will tend to proliferate and slow down the flow through the channel. **(B)** A line vortex located at distance x from the center of the channel. The line vortex begins and ends on the boundaries of the channel. **(C)** A ring vortex of radius r centered around the axis of the channel. (B) and (C) are a reproduction of Fig. 2–14 in section 2.4.3.2.

and $r \in [0, R]$ for ring vortices. Both x and r are illustrated in Fig. 4–16 (B) and (C) respectively.

Using the energy barrier to determine the vortex creation rate at fixed temperature T, in the same spirit as in Eq. (4.10), they found that

$$\Gamma = \Gamma_0 \left(e^{-\beta E_{max}(v_s)} - e^{-\beta E_{max}(-v_s)} \right), \tag{4.12}$$

where $\beta = 1/k_B T$ and Γ_0 is again the attempt rate. By appyling time-dependent Ginzburg–Landau theory in the same spirit than the Langer–Ambegaokar–McCumber–Halperin (LAMH) model for thin superconducting wires [31, 32], they were able to calculate the attempt rate Γ_0, for both ring and line vortices,

$$\Gamma_0 = \frac{1}{\tau_{GL}} \frac{LR}{\xi_4^2(T)} \begin{cases} \frac{\pi R}{\xi_4(T)} & \text{ring vortices} \\ 2\pi & \text{line vortices} \end{cases}, \tag{4.13}$$

where $\tau_{GL}^{-1} = 16k_B(T - T_\lambda)/h$ is the Ginzburg–Landau relaxation rate and L is the length of the orifice, or channel.

To relate Γ to the pressure difference ΔP across the pore through a fixed temperature, they used the Gibbs–Duhem relation[8] $h\Gamma = \frac{m_4 \Delta P}{\rho_s}$. Finally, the critical velocity v_c associated with each pore and vortex types at fixed pressure and temperature was extracted by numerically solving Eq. (4.12). Repeating this procedure for several pore radii R yields the dashed and solid curves shown in Fig. 4–17. The length scales and velocities are expressed in natural units of the ^{4}He correlation length at $T = 0$, $\xi_0 = 0.345 \cdot 10^{-10}$ m and $v_0 = \kappa_0/4\pi\xi_0 = \hbar/2\xi_0 m_4 = 22.98$ m/s, respectively. We note that ξ_0 is effectively pressure independent within the pressure range of interest in this thesis [21]. One important feature of the Bernd–Del Maestro critical velocity's model is the absence of adjustable parameters. Our experimental critical velocities are well bound by these theoretical predictions for ring vortices in orifice flow. Our smallest pore is even bound by the channel flow, which is consistent with the increase of its aspect ratio L/R. Interestingly, the smallest pore radius is only a factor of two away from a region where the critical velocity is predicted to decrease drastically owing to an increase of dissipation. In this region, the vortices creation should be enhanced because the energy barrier for vortices creation diminishes as the pore radius decreases.

---

[8] In their model, the pore has ^{4}He reservoirs located both at inlet and outlet. Therefore the term $\frac{1}{2} m_4 v_s^2$ present in Eq. (4.9) is not needed. For the pressures and temperatures considered in this thesis, the term $\frac{1}{2} m_4 v_s^2$ is always at least one order of magnitude smaller than $\frac{m_4 \Delta P}{\rho_s}$.

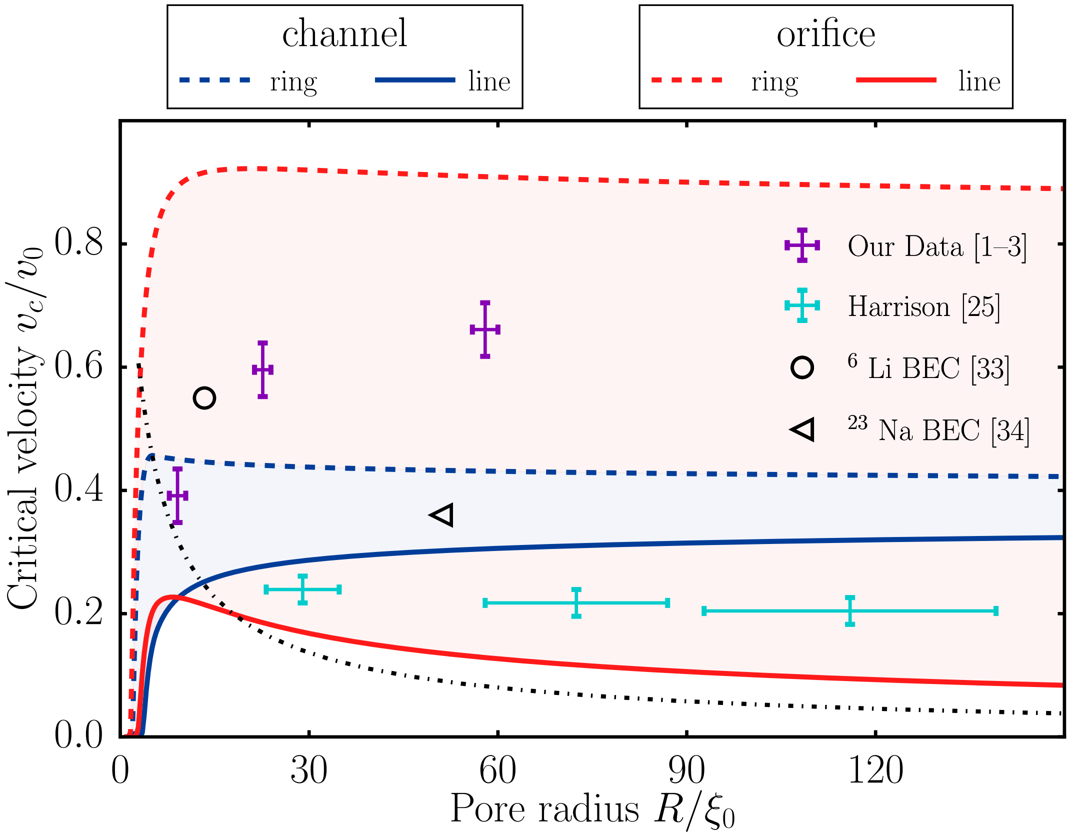

Figure 4–17: Critical velocities prediction for both ring and line vortices inside both a channel of length $L = 10^3\xi_0$ (blue) and an orifice of length $L = 10\xi_0$ (red). The temperature for the prediction was fixed at $0.7T_\lambda \simeq 1.52$ K and the pressure to 500 mbar. The solid and dashed lines represent upper bounds for the critical velocity due to thermally-activated line and ring vortices, respectively. The black dash-dotted line is the Feynman critical velocity model, described in Eq. (2.37). Our experimental critical velocities [1–3] are reproduced in natural units. They are well bound by the theoretical prediction for ring vortices in orifice flow and the smallest pore falls inside the channel flow boundary, which is consistent with the increase of its aspect ratio L/R. Other symbols show mass flow experiments on superfluid helium [25] and on BEC with ^{6}Li [33] and ^{23}Na [34]. *Source*: [4].

The temperature dependence of the critical velocities computed with the model developed by Del Maestro and Rosenow is shown in Fig. 4–18, together with the data from Fig. 4–15. The experimental critical velocities lie above the theoretical critical velocity for line vortices but are well bound by the ring vortices' critical velocity for a channel geometry. This indicates, according to their model, that the dissipation mechanisms limiting the superfluid velocity is the production of ring vortices. Above 1.95 K, the spread in the confidence interval corresponding to the shaded grey area in Fig. 4–18 becomes too wide to draw any conclusions from the comparison of the data and the model. It is unfortunately in this region, at the temperature $T^* = 2.095$ K, that the coherence length[9] equals the pore radius $R = \xi_4(T^*)$ and that the model predicts a suppression of the critical velocity. In their theoretical model, the increase of pressure leads to an increase of the critical velocities. This increase is slightly smaller than the spread in the confidence interval of our data. However, it is the same order of magnitude.

In addition we observe that below 1.6 K, the data branch off the predicted critical velocity. This could be interpreted as the superfluid velocity inside the pore not reaching the critical velocities. However, as the energy scale of the term $\frac{m_4 \Delta P}{\rho_s}$ is more than one order of magnitude larger than the kinetic energy $\frac{1}{2} m_4 v_s^2$, we discard this interpretation. This discrepancy between the model and the data could be explained by other dissipation mechanisms which are not accounted for by the model such as scattering by defects along the channel and quantum phase slips.

As the temperature approaches the absolute zero, the thermal activation of vortices will eventually be suppressed and this model based on thermal fluctuations will no longer be valid. Phase slips should still occur but via quantum fluctuations, *i.e.* by quantum tunneling through the energy barrier [35].

---

[9] The bulk values of the transition temperature T_λ and the exponent ν are used to compute the coherence length here.

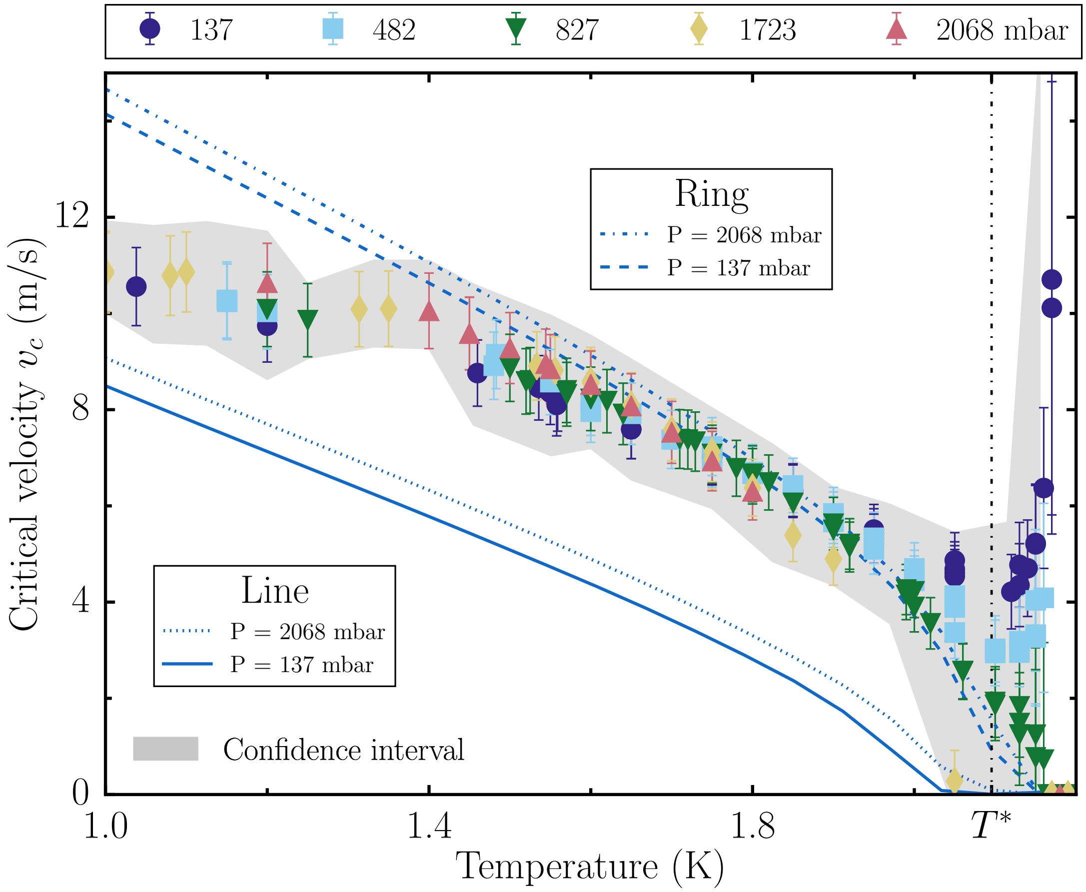

Figure 4–18: Prediction of the critical velocity temperature dependence for both line and ring vortices thermally-activated inside a channel of radius $R = 3.14$ nm and length $L = 30$ nm. The dashed-dotted black vertical line indicates the boundary where $R = \xi_4(T^*)$. At temperatures lower than T^*, $R > \xi_4(T)$. The experimental critical velocities are reproduced from Fig. 4–11 and were extracted with route (i). The shaded area represents the confidence interval within which lie the critical velocities extracted from both routes. The line vortices critical velocity is represented by the solid blue line and the dotted blue line for the lowest and highest pressures of the experimental datasets, respectively. The ring vortices critical velocity is given by the dashed and the dashed-dotted blue lines for 137 and 2068 mbar, respectively. The experimental critical velocities confidence interval is well bound by the prediction for ring vortices critical velocities and above the line vortices critical velocity limit. Thus, according to the model, it suggests that line vortices are not the limiting dissipation mechanisms in this case, as the experimental velocities are larger.

In this chapter, we demonstrated the measurement of superfluid helium flow through a *single* nanopore of ∼3 nm radius and 30 nm long. We determined the nanopore's dimensions *in situ* by fitting conductance models on ^{4}He gas and normal liquid experimental conductance, $G_{exp} = \frac{Q_{m,exp}}{\Delta P}$. We observed the superfluid behavior of the flow in the sudden rise of the mass flow at the bulk superfluid transition temperature T_λ in temperature sweeps. We discussed two different routes to extract the superfluid velocities from the total flow measurements using the two-fluid model, described in Eq. (2.27), and the normal flow model, described in Eq. (4.3). In addition, we also determined that the normal flow model did not match the pressure dependence of the observed total flow through the nanopore in the vicinity of the superfluid transition temperature. We then compared the extracted critical velocities with measurements made in previous works [2, 3]. From this comparison stem three important observations: (*i*) a much weaker pressure dependence for the mass flow in the smallest pore, (*ii*) a critical velocity well described by a power law as a function of the reduced temperature albeit with a non-universal exponent and (*iii*) decreasing critical velocities as a function of decreasing radius for pore radii below R = 20 nm, in stark contrast with what is both predicted by Feynman's critical velocity model and previously observed in micrometer-sized channels [24]. We concluded that these findings indicate that the smallest pore has reached a quasi–one-dimensional regime, in contrast to the two larger pores. This conclusion was reinforced by comparing the critical velocities inside the smallest pore with a recent theoretical model developed by Del Maestro and Rosenow [4]. This model, based on thermal nucleation of vortices in the superfluid, provides quantitative predictions for the critical velocities inside pores of different geometries. The temperature and pressure dependences of our extracted critical velocities were shown to be well bound by the model's prediction of critical velocity due to ring vortices in a channel geometry. Moreover, within this model, our smallest pore stands at the edge of a region where the superfluid velocity is predicted to be drastically suppressed due to enhanced vortices creation.

References

[1] Duc, P.-F. *et al. Sci. Adv.* **1**, e1400222–e1400222 (2015).

[2] Savard, M., Dauphinais, G. & Gervais, G. *Phys. Rev. Lett.* **107**, 254501 (2011).

[3] Savard, M. *Towards a One-Dimensional State of Neutral Matter.* Ph.D. thesis, McGill University (2014). `http://gervaislab.mcgill.ca/Savard_PhD_Thesis.pdf`.

[4] Del Maestro, A. & Rosenow, B. *Phys. Rev. B* **95**, 140507 (2017).

[5] Savard, M., Tremblay-Darveau, C. & Gervais, G. *Phys. Rev. Lett.* **103**, 104502 (2009).

[6] Norcada. TEM membranes spec. sheet (2017). `https://www.norcada.com/wp-content/uploads/2017/03/TEM-Grid-Specsheet-Rev-6.pdf`.

[7] Mehio, N., Dai, S. & Jiang, D. *J. Phys. Chem. A* **118**, 1150–1154 (2014).

[8] Clausing, P. *J. Vac. Sci. Technol. A* **8**, 636–646 (1971).

[9] Lafferty, J. M. *Foundations of Vacuum Science and Technology* (Wiley New York, 1998).

[10] Gómez-Goñi, J. & Lobo, P. J. *J. Vac. Sci. Technol. A* **21**, 1452–1457 (2003).

[11] Dauphinais, G. *Fabrication, Structural Relaxation, and Flow in Solid-State Nanopores.* Master's thesis, McGill University (2011). `http://gervaislab.mcgill.ca/Dauphinais_MSc_Thesis.pdf`.

[12] Langhaar, H. L. *J. Appl. Mech.* **9**, A55–A58 (1942).

[13] Donnelly, R. J. & Barenghi, C. F. *J. Phys. Chem. Ref. Data* **27**, 1217–1274 (1998).

[14] Goodwin, J. *The Pressure Dependence of Viscosity in Liquid Helium.* Ph.D. thesis, University of Washington (1968).

[15] NIST. Nist chemistry webbook. `http://webbook.nist.gov/chemistry/fluid` (2017).

[16] Duc, P.-F. Helium property interpolator (2015). `https://github.com/Bachibouzouk/liquid-helium-physical-properties-interpolator`.

[17] Kim, M. J., Wanunu, M., Bell, D. C. & Meller, A. *Adv. Mater.* **18**, 3149–3153 (2006).

[18] Velasco, A. E., Yang, C., Siwy, Z. S., Toimil-Molares, M. E. & Taborek, P. *Applied Physics Letters* **105**, 033101 (2014).

[19] Atkins, K. *Adv. Phys.* **1**, 169–208 (1952).

[20] Reppy, J. D. *J. Low. Temp. Phys.* **87**, 205–245 (1992).

[21] Singasaas, A. & Ahlers, G. *Phys. Rev. B* **30**, 5103–5115 (1984).

[22] Zassenhaus, G. M. & Reppy, J. D. *Phys. Rev. Lett.* **83**, 4800–4803 (1999).

[23] Gasparini, F. M., Kimball, M. O., Mooney, K. P. & Diaz-Avila, M. *Rev. Mod. Phys.* **80**, 1009–1059 (2008).

[24] Varoquaux, E. *C. R. Phys.* **7**, 1101–1120 (2006).

[25] Harrison, S. J. & Mendelssohn, K. *Superfluid ^{4}He velocities in narrow channels between 1.8 and 0.3 K*, vol. 1 (Springer, New York, 1974).

[26] Beecken, B. P. & Zimmermann, W. *Phys. Rev. B* **35**, 1630–1635 (1987).

[27] Anderson, P. W. *Rev. Mod. Phys.* **38**, 298–310 (1966).

[28] Trela, W. J. & Fairbank, W. M. *Phys. Rev. Lett.* **19**, 822–824 (1967).

[29] Langer, J. S. & Fisher, M. E. *Phys. Rev. Lett.* **19**, 560–563 (1967).

[30] Feynman, R. P. *Application of Quantum Mechanics to Liquid Helium - Chap. II* (Elsevier, 1955).

[31] Langer, J. S. & Ambegaokar, V. *Phys. Rev.* **164**, 498–510 (1967).

[32] McCumber, D. E. & Halperin, B. I. *Phys. Rev. B* **1**, 1054–1070 (1970).

[33] Weimer, W. *et al. Phys. Rev. Lett.* **114**, 095301 (2015).

[34] Raman, C. *et al. Phys. Rev. Lett.* **83**, 2502–2505 (1999).

[35] Khlebnikov, S. *Phys. Rev. Lett.* **93**, 090403 (2004).

CHAPTER 5

Conclusion and outlook

5.1 Summary

In this thesis, we reported mass flow measurements of superfluid ^{4}He through a *single* nanopore. The overarching goal of this study was the one-dimensional confinement of ^{4}He in order to achieve an experimental realization of a Tomonaga–Luttinger liquid. We advanced successfully towards this goal by measuring the superfluid ^{4}He flow through a $\sim$3 nm radius nanopore and showed that our measurements indicate a crossover to a quasi–one-dimensional regime. The radius of our pore is a factor 2.5 smaller than previously reported in Michel Savard's Thesis at McGill University [1]. We compared the mass flow and associated superfluid critical velocities with data from previous studies [1, 2]. The comparison yields three important findings: (*i*) the pressure dependence of the mass flow is much weaker in the pore with a $\sim$3 nm radius than in larger ones, (*ii*) for this small pore, the superfluid critical velocity fits a power law of the reduced temperature with a non-universal exponent and (*iii*) the critical velocity decreases with pore size for pores with radii below 20 nm, in stark contrast with the behavior predicted by Feynman's critical velocity model and as previously observed in larger pores [3].

We interpret these findings as the signature of a crossover to a quasi–one-dimensional state whereby increased fluctuations are modifying superfluidity. This interpretation is further supported by recent theoretical advances in modeling the superfluid flow inside pores as a function of their size and its temperature [4]. Our data showed good agreement with this model's predictions. Moreover, within this model, our smallest pore's radius stands very close to the critical pore size at which the superfluid velocity would sharply decrease due to enhanced thermal vortices creation.

On the technical side, we have suggested routes for improving the production of smaller nanopores. We successfully conducted proof-of-concept experiments of the nanopores' walls Atomic Layer Deposition coating and it appears as a viable route to yield nanopores with radii even smaller than ∼3 nm and with different aspect ratios. Besides, the ability to tune the nanopore's length will be key asset in order to probe algebraic decay of the superfluid order parameter in a TLL. In addition, the most recently fabricated experimental cell at McGill for a dilution refrigerator extends the range of temperatures for which the superflow can be measured. These two advances will hopefully lead collaborators to observe crossover to a pure one-dimensional regime. The lower temperatures achievable, ∼50 mK, will also allow to probe dissipation in both regimes, *i.e.* from thermally-activated phase slips, to the quantum regime where phase slips occur due to quantum fluctuation and tunneling events through the energy activation barrier [5].

5.2 Outlook

As we approach the final goal, some assumptions made to model our data will no longer be valid and hence will need to be questioned. For example, the fluid-wall interactions will become important when the radii get close to 1 nm. These interactions are currently neglected in the Langhaar hydrodynamic short-pipe model we used to model the normal part of the flow. Another assumption we made was that the bulk values of ^{4}He density and viscosity could be used inside the pore. We cannot expect this assumption to hold true as the radius of the pore is further reduced. Ultimately, the density units will have to shift from kg/m^3 to kg/m. Recent numerical simulations studies of ^{4}He inside nanopores provide predictions of the superfluid density temperature dependence inside pores with 0.3–1.5 nm radii [6, 7]. Yet, an independent experimental determination of the density and superfluid density inside the confined geometry of the pore for radii in the 1.5–3 nm range would be of great interest.

These numerical simulation studies bring hope in terms of achieving a one-dimensional state of matter by confining ^{4}He in a nanopore. Indeed, these simulations used a radius only a factor 2 away from the smallest pore presented in this thesis. The results of these simulations show that the ^{4}He atoms tend to arrange in concentric shells centered on the pore axis. Remarkably, they show TLL physics in the central region. Another interesting finding from these simulations is that the inner surface of the pore is covered by a few solid-like ^{4}He layers, thus providing additional confinement[1] to the remaining superfluid ^{4}He as well as a screening effect

---

[1] According to Ref. [6], the solid layer thickness could vary from 0.2 to 0.3 nm.

from surface defects and from the wall potential of the pore inner surface. Provided these effects are indeed present in the nanopore, they would tend to increase the critical pore radius at which a TLL could be realized.

As the channel size of our Si_3N_4 pores is reduced further, we expect to observe physics characteristic of a true one-dimensional system. When this is the case, and according to the TLL predictions, the algebraic decay of the superfluid order parameter should manifest itself as: (*i*) a reduction of the superfluid density as a function of channel length, (*ii*) the appearance of non-universal power laws in the mass flow dependence on pressure ($Q_{m,1D} \sim \Delta P^{\beta}$) and temperature ($Q_{m,1D} \sim T^{\gamma}$). Such observations would signal the experimental discovery of a truly one-dimensional bosonic interacting quantum liquid. Furthermore, diluting a small amount of ^{3}He inside the ^{4}He would allow us to study the indistinguishability of fermions and bosons, as predicted by theory.

The recent numerical simulations of ^{4}He confined in pores and the theoretical advances modeling dissipation mechanisms in superfluid flow, such as described in Refs. [4, 6, 7], highlight the importance to keep pushing the limits of this experimental research further, to provide a stable testing ground for TLL physics and dissipation mechanisms in the fascinating quantum liquids which are ^{4}He and ^{3}He. We hope that the experimental progress we have achieved in this work will motivate the next series of efforts to reach the one-dimensional world.

References

[1] Savard, M. *Towards a One-Dimensional State of Neutral Matter.* Ph.D. thesis, McGill University (2014). `http://gervaislab.mcgill.ca/Savard_PhD_Thesis.pdf`.

[2] Savard, M., Dauphinais, G. & Gervais, G. *Phys. Rev. Lett.* **107**, 254501 (2011).

[3] Varoquaux, E. *C. R. Phys.* **7**, 1101–1120 (2006).

[4] Del Maestro, A. & Rosenow, B. *Phys. Rev. B* **95**, 140507 (2017).

[5] Khlebnikov, S. *Phys. Rev. Lett.* **93**, 090403 (2004).

[6] Kulchytskyy, B., Gervais, G. & Del Maestro, A. *Phys. Rev. B* **88**, 064512 (2013).

[7] Del Maestro, A., Boninsegni, M. & Affleck, I. *Phys. Rev. Lett.* **106** (2011).

Appendices

APPENDIX A

Heat conduction through a solid material

The thermal power P_{th} due to a temperature gradient along the axis of a cylindrical object can be estimated by the following relation

$$P_{th} = \frac{A}{L}\int_{T_C}^{T_H} k(T)\mathrm{d}T, \tag{A.1}$$

where A is the area of the cylinder's cross section, L is the cylinder's length, $T_H > T_C$ are the temperatures across the two ends of the cylinder and $k(T)$ is the thermal conductivity. The thermal conductivity is temperature and material dependent.

APPENDIX B

Dilution cryostat cycle

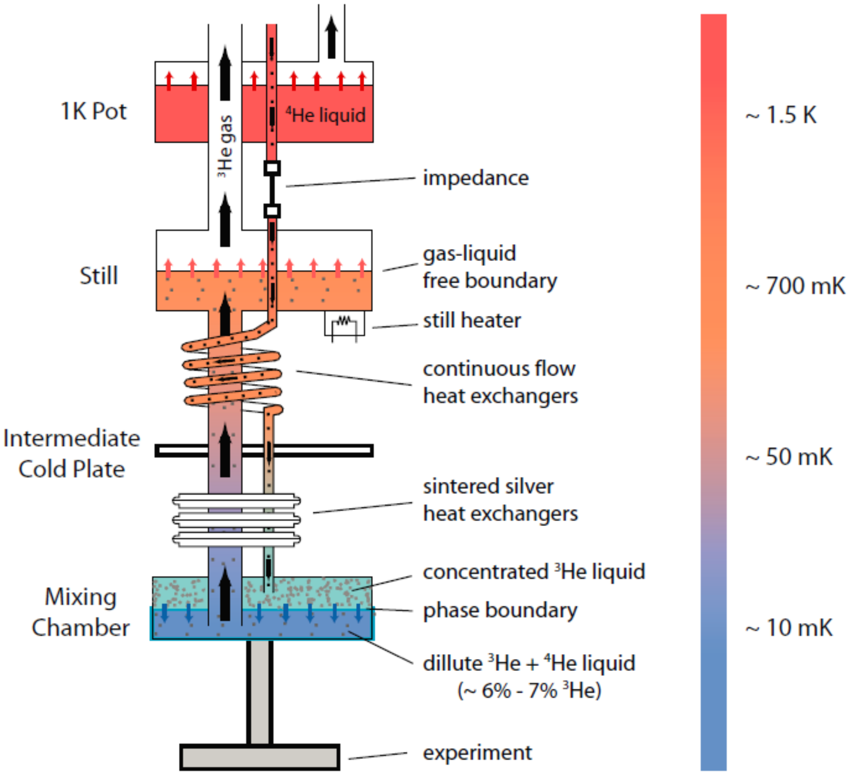

Figure B–1: Dilution cycle as depicted in section 3.1.2. *Source*: [1].

APPENDIX C

Capillary circuit inside dilution dry cryostat.

The capillaries between the 4 K plate and the still plate and to the cold plate have a diameter of 0.006", while the capillaries from outside to the 50 K and from to the 4 K plates as well as the return line from the cell have a diameter of 0.030". Efforts were made to minimize the thermal link due to helium within the capillaries by making the capillaries longer and coiling them. Dental floss was used to tighten the coils together and avoid mechanical vibration.

Plate name	T(K)	Source (μW)	Drain (μW)	Total heat (μW)
50 K plate	49	$7.0 \cdot 10^{3}$	$2.7 \cdot 10^{4}$	$3.4 \cdot 10^{4}$
4 K plate	3.2	$2.2 \cdot 10^{2}$	$6.8 \cdot 10^{2}$	$9.0 \cdot 10^{2}$
Still	0.8	$5.2 \cdot 10^{-1}$	1.6	2.1
Cold plate	0.07	$3.1 \cdot 10^{-2}$	$5.7 \cdot 10^{-2}$	$8.8 \cdot 10^{-2}$

Table C–1: Heat leaks due to the empty lines. Note: the cold plate does not usually reach 7 mK. Thus, the heat leak correspond to the worst case senario.

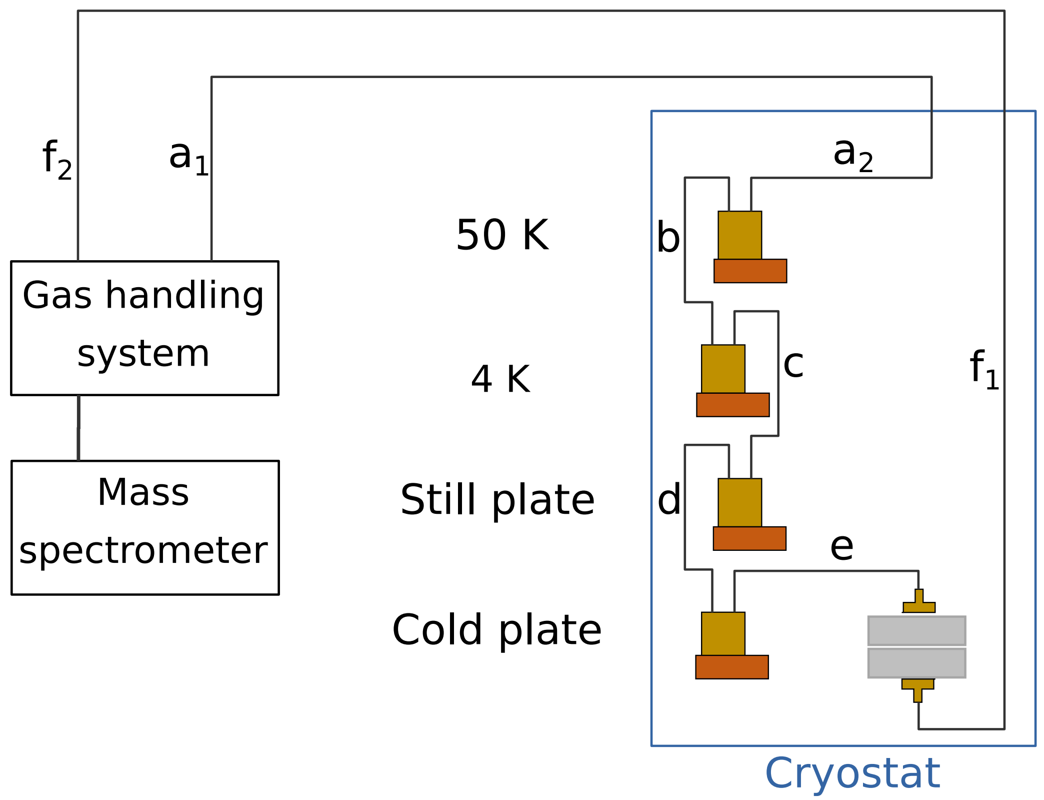

Figure C–1: See Tab. C–2 for dimensions of the capillaries.

Portion of circuit	Material	diameter	length (m)
a_1	SS	0.03 (in)	6.4
a_2	SS	0.03 (in)	1.37
b	SS	0.03 (in)	1
c	SS	0.006 (in)	0.2
d	CuNi	0.3 (mm)	1
e	CuNi	1 (mm)	0.4
f_1	SS	0.03 (in)	0.91
f_2	SS	0.03 (in)	7.4

Table C–2: SS stands for stainless steel 316 and CuNi for copper nickel.

APPENDIX D

Clausing factor

Figs. D–2 and D–3 show Clausing factor computed by Iczkowski [2] (circles) for a series of angles of the channel's opening θ and a series of channel's aspect ratios L/R, respectively. A perfect cylindrical tube has an angle of 0° and a pinhole has an angle of 90° as shown on Fig. D–1. The dotted lines are guides-to-the-eye.

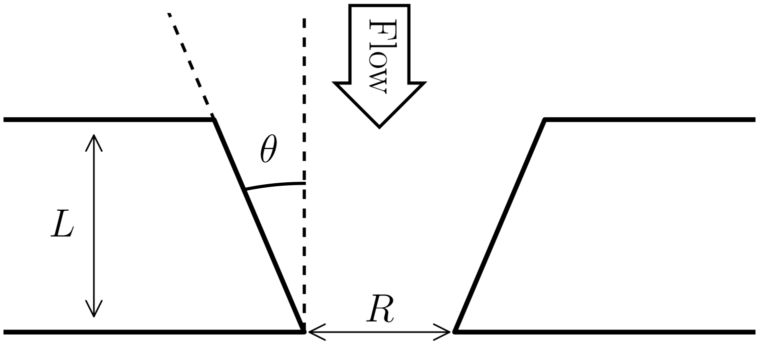

Figure D–1: Reproduction of Fig. 4–3

.

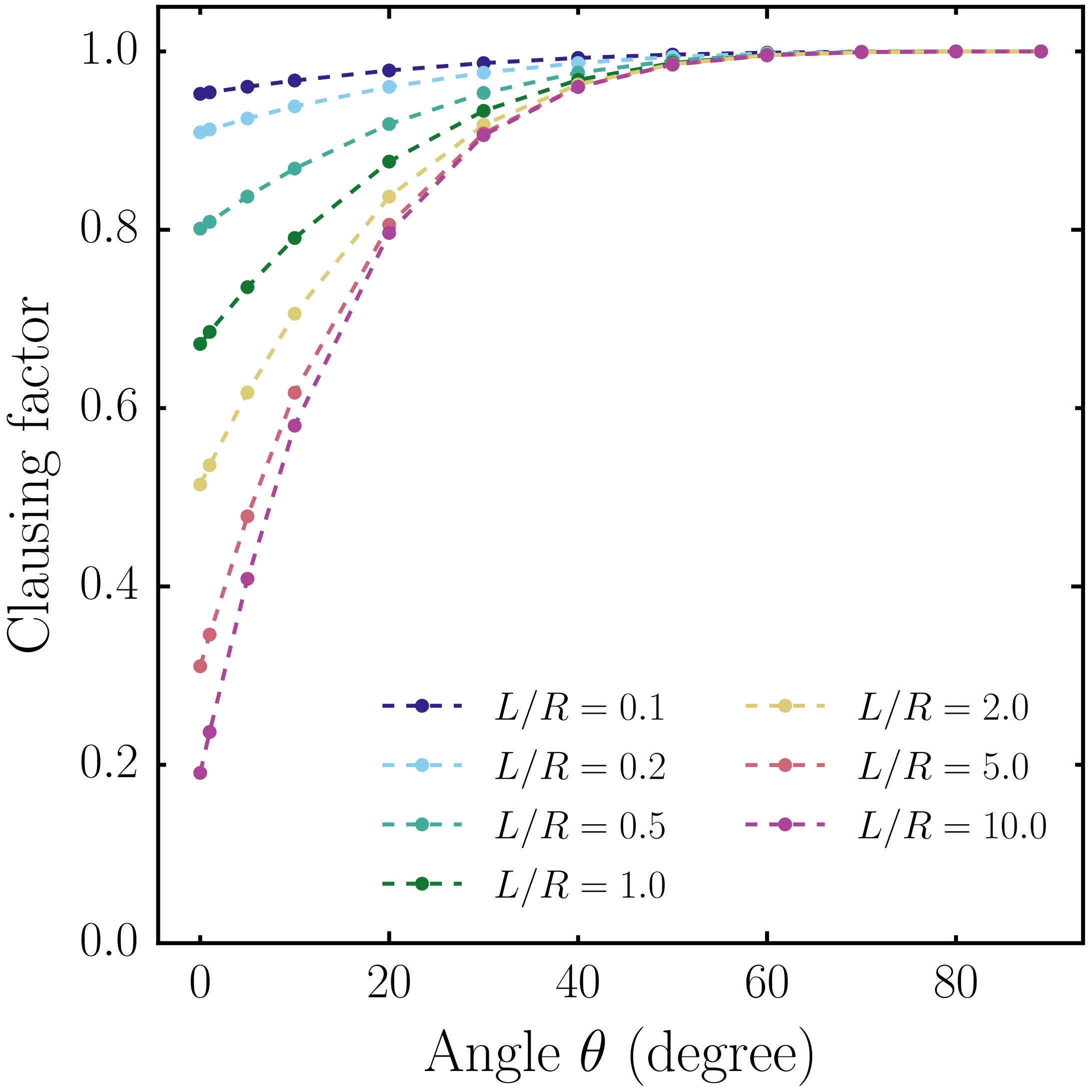
1.0
0.8
0.6
0.4
0.2
0.0
Clausing factor
0
20
40
60
80
Angle θ (degree)
$L/R = 0.1$
$L/R = 0.2$
$L/R = 0.5$
$L/R = 1.0$
$L/R = 2.0$
$L/R = 5.0$
$L/R = 10.0$

Figure D–2:

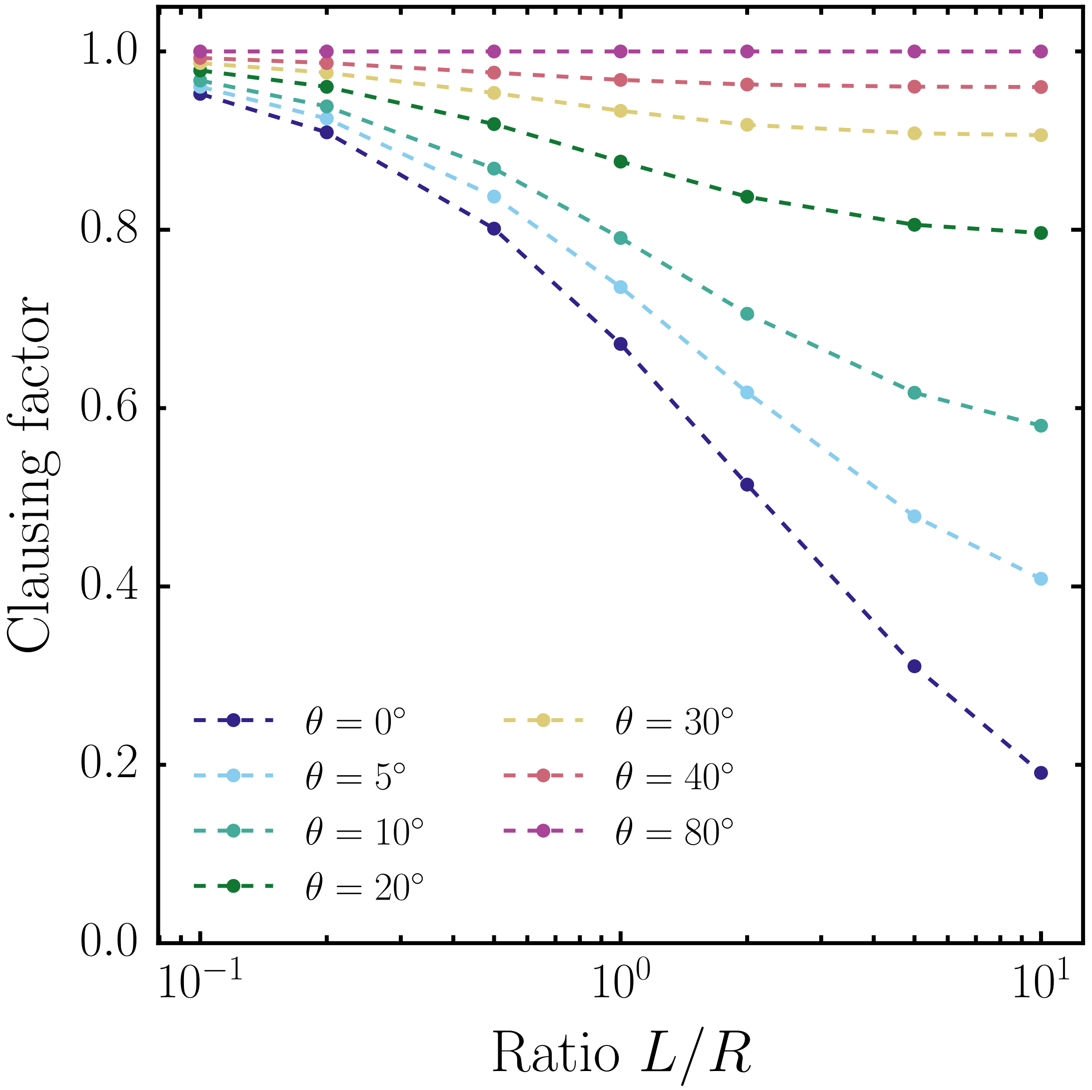
Clausing factor
Ratio L/R
1.0
0.8
0.6
0.4
0.2
0.0
10^{-1}
10^{0}
10^{1}
$\theta = 0°$
$\theta = 5°$
$\theta = 10°$
$\theta = 20°$
$\theta = 30°$
$\theta = 40°$
$\theta = 80°$

Figure D–3:

APPENDIX E

Computation of superfluid velocities for fixed pressure temperature sweeps

---

Figs. E–1 to E–5 show the critical velocities from the mass flow measured at various fixed pressures in the 3.14 nm radius pore. Horizontal axes are shared for sub-figures in the same column. **(A)** Mass flow as a function of temperature for the given pressure. The solid and dashed red lines correspond to the model in Eq. (4.3) with $\tilde{Q}_m = Q_{m,offset}$ and $\tilde{Q}_m = Q_{m,offset} + \delta\tilde{Q}_m(P)$, respectively. The grey shaded area is a visual representation of $Q_{m,offset}$ which was not subtracted from the datasets here. **(B)** Critical velocities extracted using Eq. (4.6) and Eq. (4.3) with $\tilde{Q}_m = Q_{m,offset}$ (open symbols) or $\tilde{Q}_m = Q_{m,offset} + \delta\tilde{Q}_m(P)$ (filled symbols). The colored shaded areas represent a confidence interval accounting for the experimental and fitting uncertainties. The vertical dashed line shows the bulk superfluid transition temperature T_λ at SVP.

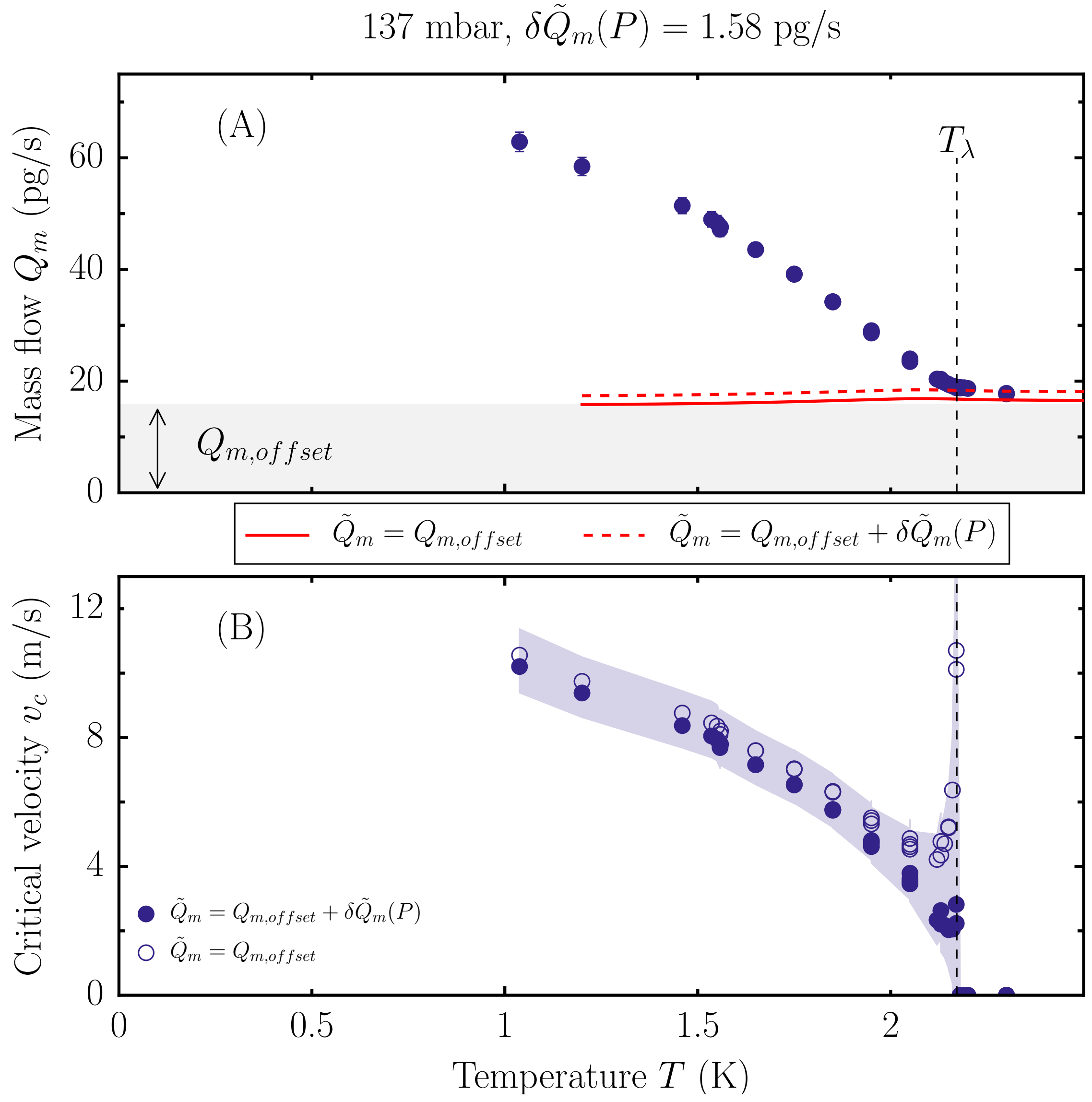

137 mbar, $\delta\tilde{Q}_m(P) = 1.58$ pg/s

Figure E–1:

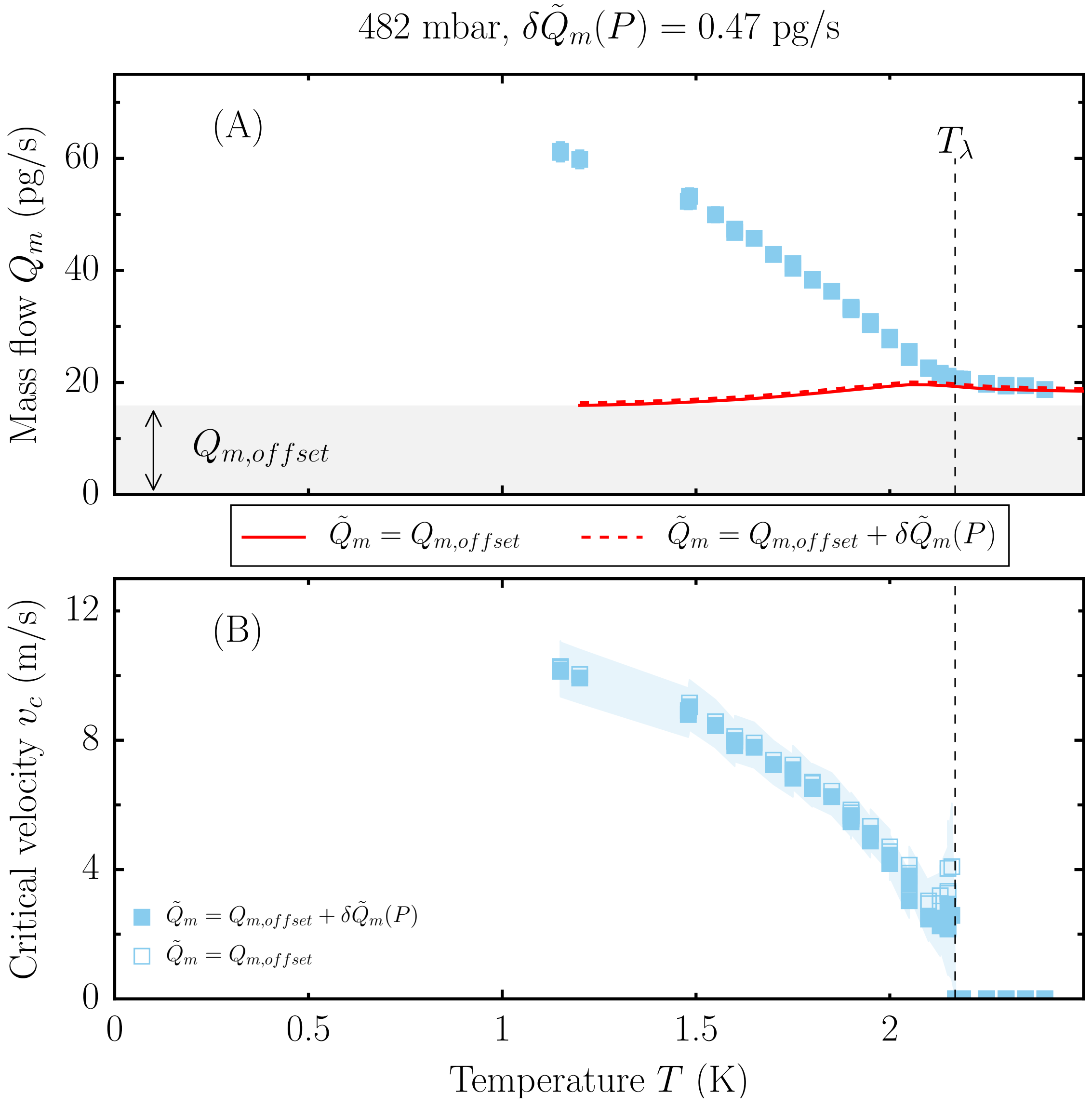
482 mbar, $\delta\tilde{Q}_m(P) = 0.47$ pg/s
(A)
T_λ
Mass flow Q_m (pg/s)
60
40
20
0
$Q_{m,offset}$
$\tilde{Q}_m = Q_{m,offset}$
$\tilde{Q}_m = Q_{m,offset} + \delta\tilde{Q}_m(P)$
(B)
Critical velocity v_c (m/s)
12
8
4
0
$\tilde{Q}_m = Q_{m,offset} + \delta\tilde{Q}_m(P)$
$\tilde{Q}_m = Q_{m,offset}$
0
0.5
1
1.5
2
Temperature T (K)

Figure E–2:

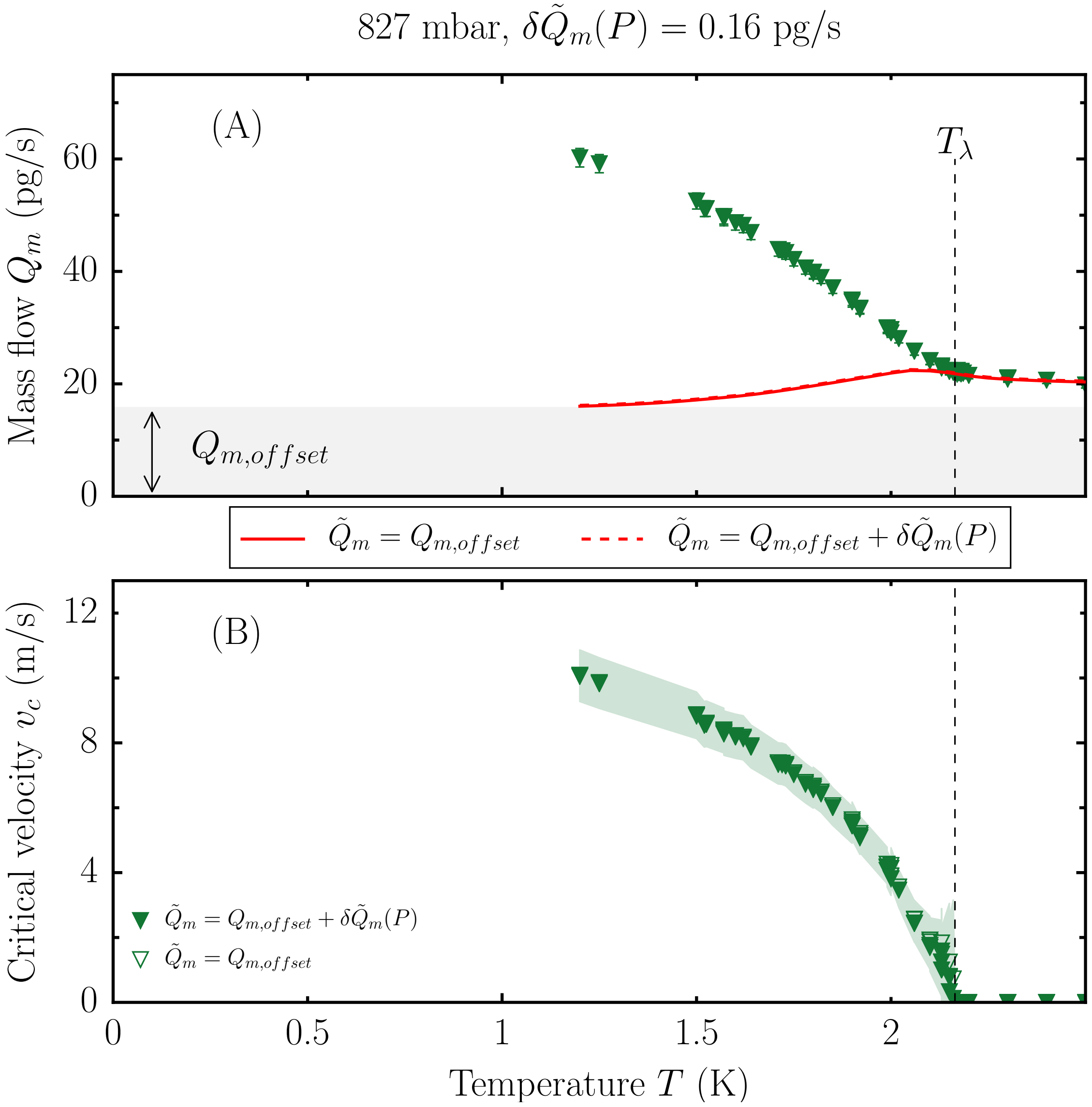
827 mbar, $\delta\tilde{Q}_m(P) = 0.16$ pg/s
(A)
T_λ
Mass flow Q_m (pg/s)
60
40
20
0
$Q_{m,offset}$
$\tilde{Q}_m = Q_{m,offset}$
$\tilde{Q}_m = Q_{m,offset} + \delta\tilde{Q}_m(P)$
(B)
Critical velocity v_c (m/s)
12
8
4
0
$\tilde{Q}_m = Q_{m,offset} + \delta\tilde{Q}_m(P)$
$\tilde{Q}_m = Q_{m,offset}$
0
0.5
1
1.5
2
Temperature T (K)

Figure E–3:

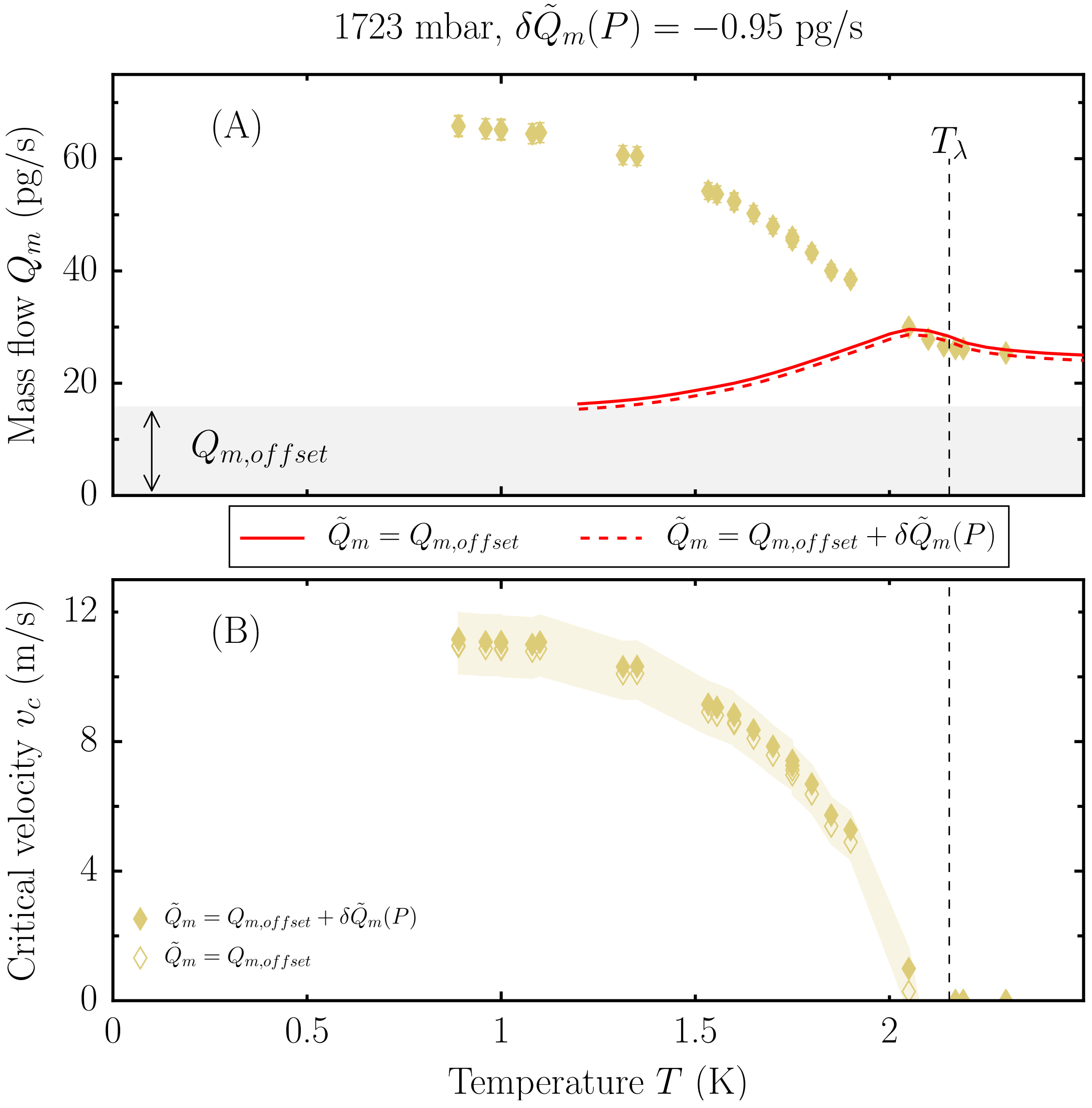
1723 mbar, $\delta\tilde{Q}_m(P) = -0.95$ pg/s
(A)
T_λ
Mass flow Q_m (pg/s)
0
20
40
60
$Q_{m,offset}$
$\tilde{Q}_m = Q_{m,offset}$
$\tilde{Q}_m = Q_{m,offset} + \delta\tilde{Q}_m(P)$
(B)
Critical velocity v_c (m/s)
0
4
8
12
$\tilde{Q}_m = Q_{m,offset} + \delta\tilde{Q}_m(P)$
$\tilde{Q}_m = Q_{m,offset}$
0
0.5
1
1.5
2
Temperature T (K)

Figure E–4:

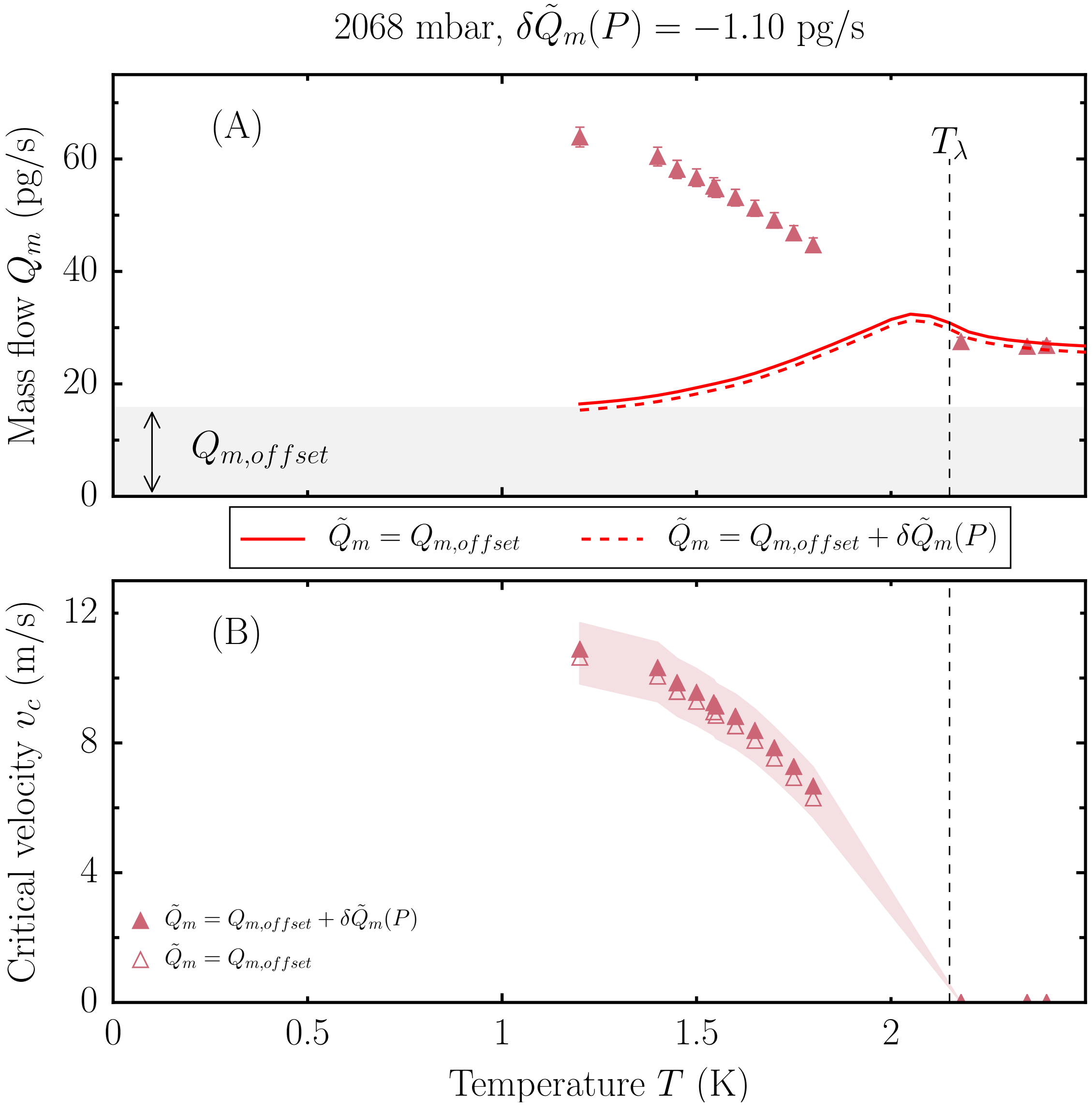
2068 mbar, $\delta\tilde{Q}_m(P) = -1.10$ pg/s
(A)
T_λ
Mass flow Q_m (pg/s)
0
20
40
60
$Q_{m,offset}$
$\tilde{Q}_m = Q_{m,offset}$
$\tilde{Q}_m = Q_{m,offset} + \delta\tilde{Q}_m(P)$
(B)
Critical velocity v_c (m/s)
0
4
8
12
$\tilde{Q}_m = Q_{m,offset} + \delta\tilde{Q}_m(P)$
$\tilde{Q}_m = Q_{m,offset}$
0
0.5
1
1.5
2
Temperature T (K)

Figure E–5:

References

[1] Dean, C. R. *A Study of the Fractional Quantum Hall Energy Gap at Half Filling*. Ph.D. thesis, McGill University (2008). `http://gervaislab.mcgill.ca/Dean_PhD_Thesis.pdf`.

[2] Iczkowski, R. P., Margrave, J. L. & Robinson, S. M. *J. Phys. Chem.* **67**, 229–233 (1963).